

AD-A252 689



(2)

TECHNICAL REPORT BRL-TR-3363

**BRL****MODELING RHA PLATE PERFORATION  
BY A SHAPED CHARGE JET**

MARTIN N. RAFTENBERG

**DTIC**  
**ELECTE**  
**JUL 13 1992**  
**S A D**

JUNE 1992

✓  
\*Original contains color  
plates: All DTIC reproductions  
will be in black and  
white\*

APPROVED FOR PUBLIC RELEASE; DISTRIBUTION IS UNLIMITED.

U.S. ARMY LABORATORY COMMAND

**BALLISTIC RESEARCH LABORATORY  
ABERDEEN PROVING GROUND, MARYLAND****92-18162**

92 7 1 047

## NOTICES

Destroy this report when it is no longer needed. DO NOT return it to the originator.

Additional copies of this report may be obtained from the National Technical Information Service, U.S. Department of Commerce, 5285 Port Royal Road, Springfield, VA 22161.

The findings of this report are not to be construed as an official Department of the Army position, unless so designated by other authorized documents.

The use of trade names or manufacturers' names in this report does not constitute indorsement of any commercial product.

# DISCLAIMER NOTICE



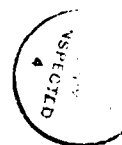
THIS DOCUMENT IS BEST QUALITY AVAILABLE. THE COPY FURNISHED TO DTIC CONTAINED A SIGNIFICANT NUMBER OF COLOR PAGES WHICH DO NOT REPRODUCE LEGIBLY ON BLACK AND WHITE MICROFICHE.

REPORT DOCUMENTATION PAGE			Form Approved OMB No 0704-0188	
<small>Public reporting burden for this collection of information is estimated to average 1 hour per response, including the time for reviewing instructions, searching existing data sources, gathering and maintaining the data needed, and completing and reviewing the collection of information. Send comments regarding this burden estimate or any other aspect of this collection of information, including suggestions for reducing this burden, to Washington Headquarters Services, Directorate for Information Operations and Reports, 1215 Jefferson Davis Highway, Suite 1204, Arlington, VA 22202-4302, and to the Office of Management and Budget, Paperwork Reduction Project (0704-0188), Washington, DC 20503.</small>				
1. AGENCY USE ONLY (Leave blank)		2. REPORT DATE <b>June 1992</b>		3. REPORT TYPE AND DATES COVERED <b>Final, May 89-Mar 92</b>
4. TITLE AND SUBTITLE <b>Modeling RHA Plate Perforation by a Shaped Charge Jet</b>			5. FUNDING NUMBERS <b>PR: 1L162618AH80</b>	
6. AUTHOR(S) <b>Martin N. Raftenberg</b>				
7. PERFORMING ORGANIZATION NAME(S) AND ADDRESS(ES)			8. PERFORMING ORGANIZATION REPORT NUMBER	
<b>U.S. Army Ballistic Research Laboratory</b> <b>ATTN: SLCBR-DD-T</b> <b>Aberdeen Proving Ground, MD 21005-5066</b>			<b>10. SPONSORING MONITORING AGENCY REPORT NUMBER</b> <b>BRL-TR-3363</b>	
11. SUPPLEMENTARY NOTES				
12a. DISTRIBUTION / AVAILABILITY STATEMENT <b>Approved for public release; distribution is unlimited.</b>			12b. DISTRIBUTION CODE	
13. ABSTRACT (Maximum 200 words)  <p>Models for metal failure by tensile voids and shear bands are presented and inserted into hydrocode EPIC-2. Each model consists of an onset criterion and a post-onset prescription on stresses. The resulting code is used to simulate an experiment involving perforation of a 13.0-mm-thick RHA plate by the leading particle of an OFHC copper jet produced by firing a shaped charge warhead at long standoff. Quantities evaluated from the experiment and compared with computational results include the final hole radius averaged over the plate's thickness, the final hole shape, the time required for hole formation, the net mass lost by the plate, and the location of voids and shear bands in the final plate cross section.</p> <p>Three parameters are varied in the calculations. One of these is associated with each of the two failure models, and the third with the slideline erosion algorithm. With neither failure model or with only the tensile failure model active, the computed hole is too small and its formation is completed prematurely. However, when both failure models are active, reasonable agreement with the experiment is obtained for a range of parameter values.</p> <p>Three problems are repeated with a finer mesh. The degree of mesh sensitivity is quantified.</p>				
14. SUBJECT TERMS <b>Shaped Charge Jets; Perforation; Shear Bands; Failure Modeling; Slideline Erosion</b>			15. NUMBER OF PAGES <b>147</b>	
			16. PRICE CODE	
17. SECURITY CLASSIFICATION OF REPORT <b>UNCLASSIFIED</b>	18. SECURITY CLASSIFICATION OF THIS PAGE <b>UNCLASSIFIED</b>	19. SECURITY CLASSIFICATION OF ABSTRACT <b>UNCLASSIFIED</b>	20. LIMITATION OF ABSTRACT <b>UL</b>	

INTENTIONALLY LEFT BLANK.

# TABLE OF CONTENTS

	<u>Page</u>
LIST OF FIGURES .....	v
LIST OF TABLES .....	xi
ACKNOWLEDGMENTS .....	xiii
1. INTRODUCTION .....	1
2. RANGE FIRING .....	1
3. THREE BENCHMARK QUANTITIES EVALUATED FROM EXPERIMENT	2
4. LEADING JET PARTICLE DESCRIPTION .....	4
5. EPIC-2 SIMULATIONS WITHOUT FAILURE MODELING .....	5
5.1 Features of EPIC-2 .....	5
5.2 Problem Series I .....	7
6. EXPERIMENTAL OBSERVATIONS OF VOIDS AND SHEAR BANDS ...	11
7. EPIC-2 SIMULATIONS WITH THE TENSILE FAILURE MODEL .....	11
7.1 The Tensile Failure Model .....	11
7.2 Problem Series II .....	14
8. EPIC-2 SIMULATIONS WITH THE TENSILE AND SHEAR BAND FAILURE MODELS .....	16
8.1 The Shear Band Failure Model .....	16
8.2 Problem Series III Through VIII .....	17
9. EXAMINATION OF RESULTS' SENSITIVITY TO MESH FINENESS ....	23
10. CONCLUDING REMARKS .....	30
11. REFERENCES .....	125
LIST OF SYMBOLS .....	127
DISTRIBUTION LIST .....	131



Availability Codes	
Dist	Avail and/or Special
A-1	

INTENTIONALLY LEFT BLANK.

## LIST OF FIGURES

<u>Figure</u>	<u>Page</u>
1. Experimental Setup for Rd. 10771 .....	38
2. Flash Radiographs of the Jet at 161.5 and 181.4 $\mu$ s After Explosive Initiation .	39
3. Flash Radiographs of the Jet and RHA Plate at 181.0 and 226.3 $\mu$ s After Explosive Initiation .....	40
4. Enlargement of Flash Radiograph of the Jet and RHA Plate at 226.3 $\mu$ s After Explosive Initiation .....	41
5. Photograph of the Perforated Plate's Entrance Surface .....	42
6. Photograph of the Perforated Plate's Exit Surface .....	43
7. Perforation Hole in RHA Plate Fitted by a Circle .....	44
8. Construction of Radial Slices to be Removed From Perforated Plate .....	45
9. Removal of Five Radial Slices From Perforated Plate .....	46
10. Five Radial Slices From the Perforated Plate .....	47
11. Digitized Boundary of a Slice From the Perforated Plate and Calculation of the Throat Radius and $\bar{r}_{hole}^{exp}$ From Rd. 10771 .....	48
12. Flash Radiographs at Various Times From Rds. 4190 and 4189 .....	49
13. Five-Parameter Geometric Model for the Leading Jet Particle .....	50
14. The Jet Particle Model Fitted to the Radiograph at 8.6 $\mu$ s Before Impact ....	51
15. The Initial Mesh Used in Sections 5, 7, and 8 .....	52
16. Mesh Plot at 3.01 $\mu$ s After Impact for Problem I-C .....	53
17. Mesh Plot at 4.02 $\mu$ s After Impact for Problem I-C .....	54
18. Mesh Plot at 500.04 $\mu$ s After Impact for Problem I-C .....	55
19. Mesh Plot at 10.02 $\mu$ s After Impact for Problem I-C, With Disembodied Nodes of Ejecta and Debris Included .....	56

<u>Figure</u>	<u>Page</u>
20. Mesh Boundary at 500.04 $\mu$ s and Calculation of $\bar{r}_{hole}$ From Problem I-C . . . .	57
21. Computed $\bar{r}_{hole}$ vs. $\epsilon_{erode}^p$ for Problem Series I . . . . .	58
22. Mesh Plot at 500.00 $\mu$ s After Impact for Problem I-E . . . . .	59
23. Mass Lost From Target Plate vs. Time for Problem Series I . . . . .	60
24. Micrograph of a Fracture Surface Formed by Void Coalescence in the RHA Target Plate of Rd. 10771 . . . . .	61
25. Micrograph of a Shear Band in the RHA Target Plate of Rd. 10771 . . . . .	62
26. Micrograph of a Crack That Extends Along a Shear Band in the RHA Plate of Rd. 10771 . . . . .	63
27. Sketch Showing Locations of Prominent Voids and Shear Bands in a Radial Slice From the RHA Plate of Rd. 10771 . . . . .	64
28. Mesh Plot at 1.02 $\mu$ s After Impact for Problem II-C . . . . .	65
29. Mesh Plot at 3.02 $\mu$ s After Impact for Problem II-C . . . . .	66
30. Mesh Plot at 500.00 $\mu$ s After Impact for Problem II-C . . . . .	67
31. Mesh Plot at 500.05 $\mu$ s After Impact for Problem II-A . . . . .	68
32. Mesh Plot at 500.03 $\mu$ s After Impact for Problem II-B . . . . .	69
33. Mesh Plot at 500.02 $\mu$ s After Impact for Problem II-D . . . . .	70
34. Mesh Plot at 500.00 $\mu$ s After Impact for Problem II-E . . . . .	71
35. Computed $\bar{r}_{hole}$ vs. $\epsilon_{erode}^p$ for Problem Series II . . . . .	72
36. Mass Lost From Target Plate vs. Time for Problem Series II . . . . .	73
37. The Deviatoric-Stress Reduction Function Used With the Shear Band Failure Model . . . . .	74
38. Computed $\bar{r}_{hole}$ vs. $\epsilon_{erode}^p$ With $\Delta\epsilon_{fail}^p$ a Parameter for Problem Series III Through VIII . . . . .	75

<u>Figure</u>	<u>Page</u>
39. Computed $\bar{r}_{hole}$ vs. $\Delta\epsilon_{fail}^P$ With $\epsilon_{erode}^P$ a Parameter for Problem Series III Through VIII .....	76
40. Mesh Plot at 1.03 $\mu s$ After Impact for Problem III-B .....	77
41. Mesh Plot at 2.01 $\mu s$ After Impact for Problem III-B .....	78
42. Mesh Plot at 3.01 $\mu s$ After Impact for Problem III-B .....	79
43. Mesh Plot at 4.03 $\mu s$ After Impact for Problem III-B .....	80
44. Mesh Plot at 5.00 $\mu s$ After Impact for Problem III-B .....	81
45. Mesh Plot at 10.01 $\mu s$ After Impact for Problem III-B .....	82
46. Mesh Plot at 20.04 $\mu s$ After Impact for Problem III-B .....	83
47. Mesh Plot at 50.04 $\mu s$ After Impact for Problem III-B .....	84
48. Mesh Plot at 100.06 $\mu s$ After Impact for Problem III-B .....	85
49. Mesh Plot at 150.05 $\mu s$ After Impact for Problem III-B .....	86
50. Mesh Plot at 200.06 $\mu s$ After Impact for Problem III-B .....	87
51. Mesh Plot at 250.04 $\mu s$ After Impact for Problem III-B .....	88
52. Mesh Plot at 300.06 $\mu s$ After Impact for Problem III-B .....	89
53. Mesh Plot at 450.05 $\mu s$ After Impact for Problem III-B .....	90
54. Mesh Plot at 500.02 $\mu s$ After Impact for Problem III-B .....	91
55. Mesh Plot at 500.00 $\mu s$ After Impact for Problem IV-C .....	92
56. Mesh Plot at 500.06 $\mu s$ After Impact for Problem V-D .....	93
57. Mesh Plot at 500.04 $\mu s$ After Impact for Problem VI-E .....	94
58. Mass Lost From Target Plate vs. Time for Problem Series III .....	95
59. Mass Lost From Target Plate vs. Time for Problem Series IV .....	96

<u>Figure</u>	<u>Page</u>
60. Mass Lost From Target Plate vs. Time for Problem Series V .....	97
61. Mass Lost From Target Plate vs. Time for Problem Series VI .....	98
62. Mass Lost From Target Plate vs. Time for Problem Series VII .....	99
63. Mass Lost From Target Plate vs. Time for Problem Series VIII .....	100
64. Computed $\Delta M$ vs. $\epsilon_{erode}^p$ With $\Delta \epsilon_{fail}^p$ a Parameter for Problem Series III Through VIII .....	101
65. Computed $\Delta M$ vs. $\Delta \epsilon_{fail}^p$ With $\epsilon_{erode}^p$ a Parameter for Problem Series III Through VIII .....	102
66. The Initial Mesh Used in Section 9 .....	103
67. Mesh Plot at 3.00 $\mu s$ After Impact for Problem I-C(R) .....	104
68. Mesh Plot at 4.00 $\mu s$ After Impact for Problem I-C(R) .....	105
69. Mesh Plot at 500.02 $\mu s$ After Impact for Problem I-C(R) .....	106
70. Mass Lost From Target Plate vs. Time for Problems I-C and I-C(R) .....	107
71. Mesh Plot at 1.00 $\mu s$ After Impact for Problem II-C(R) .....	108
72. Mesh Plot at 3.01 $\mu s$ After Impact for Problem II-C(R) .....	109
73. Mesh Plot at 500.00 $\mu s$ After Impact for Problem II-C(R) .....	110
74. Mass Lost From Target Plate vs. Time for Problems II-C and II-C(R) .....	111
75. Mesh Plot at 1.01 $\mu s$ After Impact for Problem III-B(R) .....	112
76. Mesh Plot at 2.01 $\mu s$ After Impact for Problem III-B(R) .....	113
77. Mesh Plot at 3.01 $\mu s$ After Impact for Problem III-B(R) .....	114
78. Mesh Plot at 4.00 $\mu s$ After Impact for Problem III-B(R) .....	115
79. Mesh Plot at 5.02 $\mu s$ After Impact for Problem III-B(R) .....	116
80. Mesh Plot at 10.02 $\mu s$ After Impact for Problem III-B(R) .....	117

<u>Figure</u>	<u>Page</u>
81. Mesh Plot at 20.02 $\mu\text{s}$ After Impact for Problem III-B(R) . . . . .	118
82. Mesh Plot at 50.03 $\mu\text{s}$ After Impact for Problem III-B(R) . . . . .	119
83. Mesh Plot at 100.01 $\mu\text{s}$ After Impact for Problem III-B(R) . . . . .	120
84. Mesh Plot at 200.02 $\mu\text{s}$ After Impact for Problem III-B(R) . . . . .	121
85. Mesh Plot at 500.01 $\mu\text{s}$ After Impact for Problem III-B(R) . . . . .	122
86. Mesh Boundary at 500.01 $\mu\text{s}$ and Calculation of $\bar{r}_{hole}$ for Problem III-B(R) . .	123
87. Mass Lost From Target Plate vs. Time for Problems III-B and III-B(R) . . . . .	124

INTENTIONALLY LEFT BLANK.

## LIST OF TABLES

<u>Table</u>		<u>Page</u>
1.	Parameter Values for the Leading Jet Particle's Geometric Model . . . . .	34
2.	Material Parameter Values for the Metals . . . . .	34
3.	Results From Problem Series I . . . . .	35
4.	Results From Problem Series II . . . . .	35
5.	Results From Problem Series III Through VIII . . . . .	36
6.	Results With the Refined Mesh . . . . .	37
7.	CPU Times on a Cray X-MP/48 for Six Problems . . . . .	37

INTENTIONALLY LEFT BLANK.

## ACKNOWLEDGMENTS

Thomas W. Wright and Michael J. Scheidler of the U.S. Army Ballistic Research Laboratory (BRL), Aberdeen Proving Ground, MD, and Howard Tz. Chen of the Naval Surface Warfare Center, Silver Spring, MD, provided assistance in developing the shear band model. Claire D. Krause, formerly of BRL, obtained the micrographs in Figures 24, 25, and 26 and produced the sketch in Figure 27. Robert A. Stryk and Gordon R. Johnson of Alliant Techsystems, Inc. in Brooklyn Park, MN, gave helpful comments on EPIC-2 coding. Jonas A. Zukas of BRL provided an insightful review of this report.

The author thanks Elaine Kessinger and Doris Cianelli of Nomura Enterprise Inc. for their assistance in preparing the figures.

INTENTIONALLY LEFT BLANK.

## 1. INTRODUCTION

The problem of rolled homogeneous armor (RHA) plate perforation by a shaped charge jet is one of ongoing interest to the U.S. Army Ballistic Research Laboratory. With the advent of supercomputers, the problem can now be analyzed with more detail and greater realism than has previously been possible. The present study presents an analysis of a single case, that of a particular shaped charge warhead fired at normal incidence and long standoff into a 13.0-mm-thick plate. The range firing is described in Section 2. Section 3 follows with the evaluation from experiment of three quantities pertaining to the perforated target plate that provide convenient benchmarks for hydrocode calculations. As preparation of input to the hydrocode, the geometry of the jet's leading particle is analyzed from radiographs in Section 4. Features of EPIC-2 (Johnson and Stryk 1986), the hydrocode used in this study, are reviewed in Section 5. Of particular interest is its eroding slideline feature. Also, a series of problems using only features contained in the 1986 version of EPIC-2 are presented as an initial modeling effort in this section. Section 6 presents evidence for the failure mechanisms of tensile voids and shear bands, as observed by applying microscopy to specimens removed from the perforated plate. Section 7 describes a model for failure due to tensile voids that has been installed into EPIC-2. A series of problems employing this added feature is discussed. Section 8 describes a model for failure by shear bands which has also been installed. Six series of problems are run using this model in conjunction with that for tensile voids. Results from these series are compared with experiment. In Section 9 one problem from each of Sections 5, 7 and 8 is rerun with a finer mesh in order to observe the sensitivity of results to the gridding. Section 10 summarizes the findings and suggests follow-up work.

## 2. RANGE FIRING

The shaped charge warhead used has a conical copper liner with a 42° apex angle, an 81.28-mm outer-diameter base, and a 1.91-mm wall thickness. The explosive fill used is Composition-B. It is fired at a standoff of 15.23 charge diameters (C.D.) into a 13.0-mm-thick RHA plate. RHA is a medium-carbon, quenched and tempered, martensitic steel. Its allowable ranges of chemical composition and heat treatment are specified in U.S. Department of Defense (1984). The plate's cross-section is approximately square, with a 197-mm edge length. A

Brinell hardness number (BHN) of 364 for the entrance and exit surfaces is obtained. Figure 1 shows the experimental setup, including the position and orientation of four flash X-ray tubes. The round number is 10771 of Range 7A. Figure 2 displays two flash radiographs on one film sheet, taken at 161.5 and 181.4  $\mu$ s after explosive initiation. Figure 3 shows the images on the second sheet. These apply at 181.0 and 226.3  $\mu$ s after initiation. Figure 4 contains an enlargement of the image at 226.3  $\mu$ s after initiation. This time corresponds to about 36  $\mu$ s after initial impact with the plate. Figures 2 through 4 show the jet's leading particle to have completely perforated the plate. The trailing particles are aligned with the leading particle and pass through the hole that it has made.

### 3. THREE BENCHMARK QUANTITIES EVALUATED FROM EXPERIMENT

The perforated plate's entrance surface is shown in Figure 5. Its exit surface is presented in Figure 6. The plate's hole is reasonably circular, except for a single notched region. Away from this notch, the hole is assumed to have been created entirely by the jet's leading particle. This assumption is supported by the degree of alignment in the jet's particles that was noted in the radiographs above. The hole is fitted by a circle (Figure 7), and radii spaced at  $25.7^\circ$  are constructed (Figure 8). Slices of plate material corresponding to five adjacent radii are removed (Figures 9 and 10). The boundary of the uppermost slice in Figure 10 is digitized to describe the hole's profile (Figure 11).

$\bar{r}_{hole}^{exp.}$  is defined as the value determined from experiment of the final hole boundary's radius averaged over the plate's thickness. The average radius of the red surface in Figure 11 is determined by numerical integration of the digitized coordinates. The result is a value of 18.2 mm for  $\bar{r}_{hole}^{exp.}$ , so

$$\bar{r}_{hole}^{exp.} = 18.2 \text{ mm} \quad (1)$$

This quantity will serve as a convenient benchmark by which to evaluate hydrocode solutions. Two other quantities that will also serve this function are  $\Delta M^{exp.}$  and  $t_{95}^{exp.}$ .  $\Delta M^{exp.}$  is defined to be the experimentally-determined total mass lost by the target plate.  $t_{95}^{exp.}$  is the experimentally-determined time after initial impact at which the plate has lost 95% of this mass. No data by which to evaluate  $\Delta M^{exp.}$  and  $t_{95}^{exp.}$

were obtained from Round (Rd.) 10771.

Fortunately, two more recent experiments, Rds. 4189 and 4190 of Range 16, do provide such data. In both of these experiments, the same shaped charge warhead employed in Rd. 10771 was fired into an RHA plate at a standoff of 975 mm (12.0 C.D.) The impact conditions at this standoff are quite similar to those at 15.2 C.D. In both cases the entire jet has broken up into particles that have probably ceased to stretch. Spacings between successive particles are greater at 15.2 C.D. than at 12.0 C.D., but Figures 3 and 4 establish that the fastest particles and probably most particles pass through the hole made by the first particle without contacting the plate. The target plates in Rds. 4189 and 4190 had respective thicknesses of 12.6 and 12.8 mm, both close to the 13.0 mm value of Rd. 10771. Thus data from Rds. 4189 and 4190 are assumed transferrable to Rd. 10771.

In Rd. 4190 the plate was weighed before and after the firing to produce a measurement of 136 g for  $\Delta M^{exp.}$ , so

$$\Delta M^{exp.} = 136 \text{ g} \quad (2)$$

A total of six flash radiographs was obtained from Rds. 4190 and 4189. As shown in Figure 12, these radiographs visualize the debris patterns at 1.7, 18.2, 33.2, 73.9, 143.2 and 213.0  $\mu\text{s}$  after initial impact. The three earliest views were obtained from Rd. 4190, and the three latest from Rd. 4189. The first RHA fragments to form are small and are seen to keep pace with the fastest moving jet particles. Much larger fragments appear at later times. In Section 8 distinct micromechanical mechanisms will be suggested for these two classes of fragments. It seems from Figure 12 that substantial material has separated from the plate subsequent to 73.9  $\mu\text{s}$  after impact. A rough estimate for  $t_{95}^{exp.}$  is therefore

$$t_{95}^{exp.} > 73.9 \mu\text{s} \quad (3)$$

The difficulty with assigning a time of fragment separation from the target plate on the basis of radiographs such as Figure 12 should be borne in mind, however. Such radiographs directly show only the later time at which the separated fragment has moved a noticeable distance from the plate.

#### 4. LEADING JET PARTICLE DESCRIPTION

Figure 2 shows the leading jet particle at 161.5 and at 181.4  $\mu\text{s}$  after initiation. These times correspond to 28.5 and 8.6  $\mu\text{s}$  before impact, respectively. Based on these two images, the leading particle's impact velocity is determined to be 7.73 mm/ $\mu\text{s}$ .

A cylindrical coordinate system is introduced, with its origin at the center of the target plate's entrance surface. Axial coordinate  $z$  measures distance from this surface, with positive values in the region between the plate and the warhead's original position. The digitized image of the jet's leading particle at 8.6  $\mu\text{s}$  before impact is mapped onto this cylindrical coordinate system by translation and rotation. The mapping is defined by three constraints: (i) and (ii) The particle's volume and centroid location, when computed based on the portion on one side of the  $r = 0$  centerline, agree with those computed using the portion on the other side of the centerline. (iii) Following translation and rotation, the point on the digitized boundary that intersects the centerline at the lowest  $z$  coordinate is assigned the position  $z = 0$ , i.e., is placed in contact with the center of the plate's entrance surface. In addition to producing a geometry on which to base input to an axisymmetric hydrocode analysis, the mapping determines the particle's length, volume and centroid position to be 20.6 mm, 353.2 mm<sup>3</sup>, and 7.97 mm above the base, respectively.

A five-parameter model for the leading particle's geometry is shown in Figure 13. The model's length  $L_P$ , volume  $V_P$ , and centroid position  $\bar{z}_P$  are expressed in terms of its five parameters by

$$L_P = L_C + L_S + L_B \quad (4)$$

$$V_P = \pi R_S^2 \left( \frac{1}{3} L_C + L_S + L_B \chi \right) \quad (5)$$

$$\bar{z}_P = \frac{\frac{1}{3}L_C \left[ L_B + L_S + \frac{1}{4}L_C \right] + L_S \left[ L_B + \frac{1}{2}L_S \right] + \frac{1}{2}L_B^2\chi}{\frac{1}{3}L_C + L_S + L_B\chi} \quad (6)$$

where

$$\chi = 1 + \frac{\pi}{2} \left[ \frac{R_B}{R_S} - 1 \right] + \frac{2}{3} \left[ \frac{R_B}{R_S} - 1 \right]^2 \quad (7)$$

$L_P$ ,  $V_P$  and  $\bar{z}_P$  are assigned the values 20.6 mm, 353.2 mm<sup>3</sup>, and 7.97 mm, respectively, as evaluated above on the basis of a radiograph. Equations (4), (5) and (6) can then be viewed as three equations in the five unknowns  $L_C$ ,  $L_S$ ,  $L_B$ ,  $R_S$  and  $R_B$ . A solution is obtained for  $L_C$ ,  $L_S$  and  $L_B$  in terms of  $R_S$  and  $R_B$ . Corresponding to a guess for the values of  $R_S$  and  $R_B$ , the quantities  $L_C$ ,  $L_S$  and  $L_B$  are evaluated and the model of Figure 13 is drawn. This procedure is applied iteratively until a close visual fit to the jet particle's shape according to the radiograph is obtained. The image in Figure 14, which corresponds to the values for  $L_C$ ,  $L_S$ ,  $L_B$ ,  $R_S$  and  $R_B$  that are listed in Table 1, is deemed to be an acceptable fit to the radiograph.

## 5. EPIC-2 SIMULATIONS WITHOUT FAILURE MODELING

**5.1 Features of EPIC-2.** The 1986 version of Lagrangian hydrocode EPIC-2 (Johnson and Stryk 1986) is used to model the Rd. 10771 experiment. The two metals, copper and steel, are both handled in the same fashion. Their dilatational deformation is governed by the Mie-Grüneisen equation of state

$$p = \left[ K_1\mu + K_2\mu^2 + K_3\mu^3 \right] \left[ 1 - \frac{1}{2}\Gamma\mu \right] + \Gamma(1 + \mu)e \quad (8)$$

where

$$\mu = \frac{\rho}{\rho_0} - 1 \quad (9)$$

$p$  is pressure, or negative hydrostatic stress,  $\rho$  is current density,  $\rho_0$  is undeformed density,  $e$  is the internal energy per undeformed volume, and  $\Gamma$  is the Grüneisen coefficient. Values for  $K_1$ ,  $K_2$ ,  $K_3$  and  $\Gamma$  are presented for OFHC copper and for 304 stainless steel in Kohn's handbook (Kohn 1965). These parameter values are displayed in Table 2, in which Kohn's values for austenitic 304 stainless steel have been applied to martensitic RHA.

The distortional deformation of copper and steel is treated by means of a plasticity model, which applies the von Mises yield condition as follows: At each cycle, deviatoric Cauchy stress components  $s_{rr}$ ,  $s_{zz}$ ,  $s_{\theta\theta}$  and  $s_{rz}$  are computed by applying elastic shear modulus  $G$  to the total strain increment. Equivalent stress  $\sigma$  is then computed using

$$\sigma = \left[ \frac{3}{2}(s_{rr}^2 + s_{zz}^2 + s_{\theta\theta}^2) + 3s_{rz}^2 \right]^{\frac{1}{2}} \quad (10)$$

and is compared to the current flow stress  $\sigma_y$ , a measure of the state of the material. If  $\sigma < \sigma_y$ , only elastic deformation occurs during that cycle and the computed stress components are unaltered. If  $\sigma \geq \sigma_y$ , plastic, non-recoverable deformation occurs as well as elastic. If  $\sigma > \sigma_y$ , stresses are adjusted along a radial path in stress space so that  $\sigma$  becomes equal to  $\sigma_y$ .

Flow stress  $\sigma_y$  is computed using the Johnson-Cook strength model (Johnson and Cook 1983). According to this model,  $\sigma_y$  is a function of equivalent plastic strain  $\epsilon^p$ , equivalent plastic strain rate  $\dot{\epsilon}^p$ , and homologous temperature  $T^*$ . The functional form is

$$\sigma_y = \left[ A + B(\epsilon^p)^N \right] \left[ 1 + C \ln \left( \frac{\dot{\epsilon}^p}{1.0s^{-1}} \right) \right] \left[ 1 - (T^*)^M \right] \quad (11)$$

where

$$\dot{\epsilon}^p = \left[ \frac{2}{3} D_{ij}^p D_{ij}^p \right]^{\frac{1}{2}} \quad (12)$$

and

$$\epsilon^p = \int_0^t \dot{\epsilon}^p dt \quad (13)$$

$t$  is time and  $D_{ij}^p$  is the plastic component of the rate of deformation tensor.  $T^*$  is related to room temperature  $T_r$  and melting temperature  $T_m$  by

$$T^* = \frac{T - T_r}{T_m - T_r} \quad (14)$$

where  $T$  is the current temperature, computed using a thermodynamic relation. Equation (11) expresses strain hardening, strain rate hardening, and thermal softening as separate factors. Hardening is assumed to be isotropic. Constants  $G$ ,  $A$ ,  $B$ ,  $N$ ,  $C$ ,  $M$ ,  $T_r$ , and  $T_m$  are assigned their values presented for OFHC copper and for 4340 steel by Johnson and Cook (1983). These values are listed in Table 2.

The slideline erosion algorithm of EPIC-2 enables the application of this Lagrangian hydrocode to problems in penetration mechanics. A description of this essential feature is reserved for the next subsection, 5.2.

In addition the 1986 version of EPIC-2 contains a failure model, or algorithm to cause stress reduction within a finite element subsequent to the local satisfaction of some onset criterion. This Johnson-Cook failure model is phenomenological and was derived to fit data from Hopkinson bar tests and quasi-static tensile tests (Johnson and Cook 1985). Such tests involve relatively low strain rates, so the model is judged to be inappropriate for the present application. In particular descriptions in Johnson and Cook (1985) of damaged specimens contain no mention of shear banding, which in Section 6 will be shown to constitute one of two micromechanical mechanisms for material failure found to be operative in RHA specimens from Rd. 10771. The other micromechanical mechanism is ductile voids, which apparently was also active in the experiments of Johnson and Cook. Nevertheless, the range of ambient conditions on strain rate and temperature were indeed much smaller in their experiments than in Rd. 10771, so a much simpler model for void failure will be utilized instead in this report.

**5.2 Problem Series I.** The axisymmetric mesh used in all calculations of this section as well as Sections 7 and 8 is shown in Figure 15. It consists of three-node triangular elements. The copper projectile's mesh closely approximates the

geometry of the five-parameter model with parameter values listed in Table 1. It contains 124 node points and 202 elements. The target's mesh approximates the square steel plate by a circular disk with a thickness of 13.0 mm and a radius of 104.0 mm. Individual elements in the target are isosceles right triangles, the longest edge of which has a length of 1.3 mm. This corresponds to ten layers of crossed triangles through the target plate's thickness. The target's mesh includes 3200 of these elements and 1691 node points.

The mesh contains two slidelines, both coincident with the projectile/target interface. One slideline has the projectile's surface nodes serving as master nodes and the target's surface nodes as slaves. In the other slideline this assignment is reversed.

The erosion feature is operative for both slidelines. This allows an element having one or more corner node on the master surface of the slideline to be discarded from the problem in the sense that all stresses in the element are thereafter set to zero. Since both copper projectile nodes and steel target nodes alternately serve as master nodes for one of the two slidelines, the procedure provides a means for modeling both projectile erosion and target hole formation. EPIC-2 uses three criteria to trigger erosion of a given surface element. One criterion is a user-supplied cutoff value for equivalent plastic strain,  $\epsilon_{erode}^p$ . Another is an angle cutoff, whereby none of the element's vertex angles is allowed to become less than a certain acute value. These two criteria limit the degree of distortion in the element. The third criterion discards a group of one or more elements that is connected to the master surface by a single vertex node. This criterion is motivated by the need to prevent such elements from crossing the slideline surface.

Following erosion of a slideline element, its three associated node points, to which its entire mass has been lumped, remain in the problem. One or two may become effectively disembodied from the remaining projectile or target. When this occurs, those disembodied nodes are converted from master into slave nodes. They subsequently interact with the remaining master surface and participate in momentum transfer across the slideline. Furthermore, previously interior nodes that now find themselves located on the master surface become identified as the slideline's master nodes. EPIC-2's eroding slideline algorithm is described further in Stecher and Johnson (1984).

In later sections of this report, two failure models will be developed to cause stress reduction in elements not necessarily located along the current slideline. Before considering this additional feature, consider a series of five problems that are run using only those features already discussed. It will be referred to as Problem Series I. Erosion strain  $\epsilon_{erode}^p$  is assigned the values 0.25, 0.50, 0.75, 1.25 and 2.00, as listed in Table 3. Each problem begins at the instant of initial impact and is run until 500  $\mu$ s after impact. Mesh plots for Problem I-C, for which  $\epsilon_{erode}^p$  equals 0.75, are shown at 3.01, 4.02, and 500.04  $\mu$ s after impact in Figures 16, 17, and 18, respectively. Perforation has occurred between 3.01 and 4.02  $\mu$ s after impact. This implies a penetration velocity between 3.23 and 4.32 mm/ $\mu$ s averaged over the course of perforation.

Figure 19 shows the mesh from Problem I-C at 10  $\mu$ s after impact, with the nodes disembodied by slideline erosion indicated. Each of these nodes is assigned by means of its color to one of the four categories: "target debris", "projectile debris", "target ejecta", and "projectile ejecta". "Target debris" denotes disembodied nodes of RHA material having a negative axial velocity  $\dot{z}$ . According to the coordinate system of Figure 19, nodes with negative axial velocity travel in the same direction as the jet particle and away from the original (before detonation) warhead position. "Target ejecta" denotes disembodied nodes of RHA material having a positive axial velocity, or traveling towards the original warhead position. Similarly, "projectile debris" and "projectile ejecta" denote disembodied nodes of copper material with a negative and a positive axial velocity, respectively.

Now consider results for the average hole radius at 500  $\mu$ s after initial impact,  $\bar{r}_{hole}$ . Figure 20 redraws the boundary of the target mesh of Figure 18. The portion of this boundary associated with the perforation hole boundary is shown in red.  $\bar{r}_{hole}$  is computed from Figure 20 by numerical integration of nodal coordinates along this red section. The result for Problem I-C is 11.0 mm, substantially smaller than the experimental result of 18.2 mm obtained from Figure 11. Results for  $\bar{r}_{hole}$  from Problem I-C and the other four problems in the series are listed in Table 3 and plotted vs.  $\epsilon_{erode}^p$  in Figure 21. The computed values for  $\bar{r}_{hole}$  are seen to increase with increasing  $\epsilon_{erode}^p$ . However, even for an  $\epsilon_{erode}^p$  of 2.00 (Problem I-E), the computed  $\bar{r}_{hole}$  of 13.9 mm is still substantially smaller than the experimental result. The mesh of the target plate at 500  $\mu$ s for Problem I-E is presented in Figure 22. The large value of  $\epsilon_{erode}^p$  for this problem has allowed highly distorted elements to

be retained in the final mesh. This consideration leads to the decision not to apply values of  $\epsilon_{erode}^p$  in excess of 2.00, even though the trend in Figure 21 suggests that such values might yield more realistic results for  $\bar{r}_{hole}$ .

Figure 23 plots the total mass that has eroded from the target plate vs. time after impact for the five problems of Problem Series I. These total masses are computed for a given time step by summing the masses of all steel elements that have eroded at or before that time step. Results for  $\Delta M$ , the total mass lost at 500  $\mu s$ , and  $t_{.95}$ , the time at which the plate has lost 0.95  $\Delta M$  of mass, can be obtained from Figure 23. These results are collected in Table 3.  $\Delta M$  results are rather insensitive to  $\epsilon_{erode}^p$  for  $\epsilon_{erode}^p$  equal to 0.25, 0.50, and 0.75. However, by an  $\epsilon_{erode}^p$  of 1.25,  $\Delta M$  is seen to decrease with increasing  $\epsilon_{erode}^p$ . This last trend is in contrast to the increase in hole radius  $\bar{r}_{hole}$  with increasing  $\epsilon_{erode}^p$  that was noted above. This discrepancy between relationships of  $\bar{r}_{hole}$  and  $\Delta M$  to  $\epsilon_{erode}^p$  is resolved by a comparison of the mesh plots in Figures 18 and 22. Hole growth is seen to have been accompanied by the removal of fewer RHA elements in Problem I-E than in Problem I-C. Instead, in Problem I-E many highly distorted elements have been retained, leading to much radial compression of material near the hole "throat", or most narrow cross-section, and to the formation of prominent lips at the entrance and exit surfaces along the hole boundary.  $\Delta M$  values for the five problems are all much smaller than the experimental value of 136 g in Equation (2). This is consistent with the fact that computed  $\bar{r}_{hole}$  values are all smaller than the measurement from Rd. 10771. Results for  $t_{.95}$  in Table 3 are all substantially smaller than the experimental lower bound of Equation (3).

The results from Problem Series I can be summarized as follows: For the mesh of Figure 15 and for the parameter  $\epsilon_{erode}^p$  varied simultaneously for both slidelines in the range of 0.25 to 2.00, (i)  $\bar{r}_{hole}$  is smaller than the measurement from Rd. 10771, (ii)  $\Delta M$  is smaller than the measurement from Rd. 4190, and (iii)  $t_{.95}$  is smaller than the range indicated by Rds. 4190 and 4189. In short the computed holes are too small, and their growths are completed prematurely.

## 6. EXPERIMENTAL OBSERVATIONS OF VOIDS AND SHEAR BANDS

At this point the perforated target plate of Rd. 10771 is studied further to assess the micromechanical processes that it has undergone. RHA specimens are extracted from the perforated plate in the vicinity of the hole. They are then polished, etched in 2% Nital, and examined using photomicroscopy and scanning electron microscopy. Figure 24 displays a fracture surface that has been formed by void coalescence. Figure 25 shows a shear band with a characteristic 6- $\mu$ m width, while Figure 26 displays a crack that runs along part of a shear band's length. From these figures, it is concluded that fracture, and therefore fragmentation of RHA, are associated with the two phenomena of voids and shear bands that result from interaction with the jet.

The extracted slice of RHA target plate from Rd. 10771 that was photographed to produce Figure 11 is now polished and examined with an optical microscope at magnifications up to 1000X. The goal is to observe the locations of prominent voids and shear bands in the final target plate cross-section. Here "prominent" is used to mean "observable with an optical microscope at 1000X magnification." The results are sketched in Figure 27. Voids and shear bands are seen to be concentrated in the hole boundary's region that is located near the plate's midsurface and that protrudes into the hole to form the throat. At least nine large, discrete voids and eleven shear bands can be observed in this region. Each shear band contacts either a void, the hole boundary, or in some cases both. Two or three prominent shear bands are also observed near the intersection of the hole boundary with the plate's entrance surface.

## 7. EPIC-2 SIMULATIONS WITH THE TENSILE FAILURE MODEL

**7.1 The Tensile Failure Model.** The voids in the RHA plate noted in Figure 24 are assumed to have nucleated and grown under the action of a tensile stress field. A tensile failure model to simulate effects of these voids at the finite element level is now developed and added to EPIC-2. In contrast to the slideline erosion algorithm, this tensile failure model will be applied to target and jet-particle elements throughout the domain, both on and off the slideline. The model consists of two parts: (i) a failure onset criterion and (ii) a prescription for post-onset stress reduction.

The onset criterion of the tensile failure model is developed first. The approximately spherical shape of individual voids in the photomicrograph of Figure 24 suggests that their growth was driven by the spherically symmetric portion of the stress tensor, namely the hydrostatic stress. Pressure is negative hydrostatic stress, defined in terms of  $\sigma_{rr}$ ,  $\sigma_{zz}$  and  $\sigma_{\theta\theta}$ , the radial, axial and circumferential normal components of the Cauchy stress by

$$p = -\frac{1}{3} \left[ \sigma_{rr} + \sigma_{zz} + \sigma_{\theta\theta} \right] \quad (15)$$

The RHA specimen of Figure 24 was removed from the remaining target plate in the vicinity of the perforation hole. The figure therefore displays material at about 19 mm from the shot line. The observation just made regarding spheroidally-shaped voids is assumed to apply throughout the RHA target plate. This last assumption is challengeable in that during the perforation process, RHA material that was originally located closer to the shot line presumably experienced much larger values for such field variables as strain, strain rate and temperature than did the material of Figure 24. However, the assumption receives some support from publications by researchers at SRI International (e.g., Barbee et al. 1972, Seaman et al. 1976). These publications have established that this general situation of fractures formed by coalescing spheroidal voids occurs quite commonly in shock loaded metals. They call such fracture "ductile", as opposed to their category of "brittle" fracture, which is characterized by planar cracks. In particular Barbee et al. (1972) has shown the situation to be at least sometimes applicable to OFHC copper. On this basis a pressure criterion for tensile failure onset will be applied to the copper jet particle as well as to the RHA.

In an element of either RHA target material or OFHC copper jet material, the onset of tensile failure is assumed to occur when the pressure, which at a given time step is constant in an element, becomes less than or equal to a negative-valued material parameter  $p_{fail}$ , i.e.,

$$p \leq p_{fail} < 0 \quad (16)$$

For each metal,  $p_{fail}$  is taken to be a constant, independent of both the local current values and the histories of all field variables.

The prescription for post-onset behavior will be considered next. Once the failure onset criterion of Equation (16) is met in an element, that element is no longer allowed to support hydrostatic tensile stress or deviatoric stresses. The element is only allowed to support hydrostatic compression. This involves modifications to the EPIC-2 hydrocode which at each time step affect all elements that have either then or at some previous time step satisfied Equation (16). For all such elements, deviatoric stresses are not computed, and positive hydrostatic stress values that result from evaluation of the Mie-Grüneisen equation of state are altered and set to zero.

Note that this post-onset prescription involves the instantaneous reduction to zero of certain stress components once the tensile failure onset criterion has been met. The prescription therefore ignores the possibility for gradual degradation of a material's load-bearing capability prior to its complete local failure. This neglect may be justifiable in problems involving shock loading, since the time scale of material degradation may be much smaller than those which pertain to other aspects of the problem.

The complete tensile failure model, including the onset criterion and the post-onset prescription, introduces a single additional input parameter for each material, namely  $p_{fail}$ . The issue to be addressed next is the assignment of a value to  $p_{fail}$  for each of the two materials. Relevant data were obtained by Rinehart (1951) from spallation experiments performed on several metals, including copper and 4130 steel. Spallation is defined as material failure caused by the tensile stress field that results from reflection of a compressive pulse from a free surface. In each experiment a cylindrical explosive charge was placed on one surface of a metal plate. A pellet composed of the same material as the plate was placed on the opposite surface to serve as a momentum trap. For each metal studied, Rinehart determined a value for the "critical normal fracture stress". This is the value attained in the region of spall fracture by the axial normal stress component. The values that Rinehart reported are 2.96 GPa for copper and 3.03 GPa for 4130 steel. If one assumes that a condition of uniaxial strain applied to his experiments, the pressure corresponding to each critical axial normal stress can be computed by subtracting  $2\sigma_y/3$  from the reported value, where  $\sigma_y$  is the local flow stress (Zukas 1982). The flow stress at initial yield is determined in Johnson and Cook (1983) to be 0.09 GPa for OFHC copper and 0.79 GPa for 4340 steel. If one also assumes

that the flow stress levels attained in Rinehart's experiments were never caused by strain or strain-rate hardening to greatly exceed these values, a reasonable value for  $p_{fail}$  is found to be -3.00 GPa (-30.0 kbar) for both OFHC copper and RHA steel. This value will be applied to both materials in all calculations that follow.

The tensile failure model that has been developed can be summarized as follows: In each element of either RHA target or OFHC-copper jet-particle material, tensile failure first occurs when Equation (16) is satisfied. At that time step and at all time steps thereafter, the element is not allowed to support hydrostatic tensile stress or any component of deviatoric stress. Only hydrostatic compression is allowed. The model introduces the single additional material constant  $p_{fail}$ , which is assigned the value of -3.00 GPa for both RHA and OFHC copper.

**7.2 Problem Series II.** A second series of five problems, Problem Series II, is run with this tensile failure model operative. Throughout the series,  $p_{fail}$  is assigned the value of -3.00 GPa for both RHA and copper. As in Problem Series I, erosion strain  $\epsilon_{erode}^p$  is again varied simultaneously for both slidelines over the range of 0.25 to 2.00. Mesh plots for Problem II-C, with  $\epsilon_{erode}^p$  set to 0.75, are shown at 1.02, 3.02 and 500.00  $\mu s$  after impact in Figures 28, 29 and 30, respectively. In these figures elements that are colored blue are those that have failed in tension according to the model. The phenomenon of spallation, or tensile failure brought on by reflection of a compressive shock wave at a free surface, is exhibited in Figure 29. Spallation is predicted to occur prior to perforation and in a small region directly in the path of the leading jet particle. Figure 30 shows a single non-eroded element in the final target plate, located near the plate's midsurface, in which tensile void failure has occurred. This elevation, or  $z$  coordinate, of void location is in some agreement with experiment in that all voids in Figure 27 reside within the midsurface protuberance.

Now consider final mesh plots from the other problems in this series. Figures 31 through 34 contain mesh plots at 500  $\mu s$  from Problems II-A, II-B, II-D and II-E, respectively. No failed elements are present in these final mesh plots from Problems II-A and II-B. In Problem II-D all failed elements are located near the hole boundary and slightly to the exit side of the midsurface. A larger portion of the cross-section has failed in tension in Problem II-D than in Problem II-C.

Moreover, the pattern of failed elements from Problem II-D is in better agreement with the experimental distribution of Figure 27 than is the pattern in Figure 30 from Problem II-C. Also note in Figure 33 that in Problem II-D the higher value of  $\epsilon_{erode}^p$  has allowed highly distorted RHA elements to escape erosion. The result is prominent lips on the entrance and exit surfaces at the hole boundary. Such lips are not present on the experimental cross-section in Figures 11 and 27. These two figures were obtained from the top slice shown in Figure 10. If instead one of the three middle slices in Figure 10 were focused on, distinct lips would have been included in the experimental profile.

In Problem II-E voids are present in a still larger portion of the cross-section than in Problem II-D. The lips around the hole boundary at the entrance and exit surfaces have become larger as well in Problem II-E and are now clearly larger than in any of the five experimental slices in Figure 10.

Results for  $\bar{r}_{hole}$ ,  $\Delta M$  and  $t_{.95}$  obtained from the five problems of Problem Series II are listed in Table 4.  $\bar{r}_{hole}$  is plotted as a function of  $\epsilon_{erode}^p$  for this series in Figure 35. The mass lost from the plate vs. time is plotted for the series in Figure 36.

A comparison of Table 4 and Figures 35 and 36 with Table 3 and Figures 21 and 23 shows that in general little change in computed  $\bar{r}_{hole}$ ,  $\Delta M$  and  $t_{.95}$  values has accompanied the addition of the tensile void failure model with the value of -3.00 GPa assigned to  $p_{fail}$  for both copper and RHA. For all five problems in Problem Series II,  $\bar{r}_{hole}$  and  $\Delta M$  are smaller than the experimental values in Equations (1) and (2), respectively. Thus the computed holes are still too small. For Problems II-A, II-B, II-C and II-D,  $t_{.95}$  is also much smaller than the experimental result in Equation (3), indicating that hole formation has completed prematurely. Problem II-E is exceptional in that it does yield a  $t_{.95}$  value consistent with the experimental result. Sensitivity of the results to the values used for  $p_{fail}$  for the two materials has not been studied.

## 8. EPIC-2 SIMULATIONS WITH THE TENSILE AND SHEAR BAND FAILURE MODELS

**8.1 The Shear Band Failure Model.** The algorithm inserted into EPIC-2 to model material failure from shear bands contains the same two generic parts as does the tensile failure model. These are a failure onset criterion and a prescription for post-onset stress reduction. The criterion adopted is called "Zener-Hollomon", after its apparent originators (Zener and Hollomon 1944). In a given time step the product  $[A + B(\epsilon^p)^N][1 - (T^*)^M]$  is evaluated for each RHA element that has not yet failed or eroded and that has undergone further plastic flow during that time step. (The shear band model is not applied to the copper.) This product includes contributions to the flow stress by plastic straining and by temperature. If the element also underwent plastic flow during the immediately preceding time step and if the above product has decreased from its level during that preceding time step, then the element is deemed to have begun to fail by shear banding. In effect, the criterion compares the strength increase due to plastic straining (work hardening) to its decrease due to temperature rise (thermal softening). Failure occurs when the latter exceeds the former.

Once this onset criterion has been satisfied in an element, at that and all subsequent time steps, deviatoric stresses are reduced from their computed values. However, hydrostatic tension is not altered, in contrast to the post-onset modeling for the case of tensile failure. Another difference is that the deviatoric stresses are not instantaneously set to zero, as with the previous model. Instead, their gradual reduction is imposed, qualitatively consistent with results from shear band modeling reported in Wright and Walter (1987). If  $s_{rr}^*$ ,  $s_{zz}^*$ ,  $s_{\theta\theta}^*$ , and  $s_{rz}^*$  are the four components of deviatoric stress computed by EPIC-2 in such an element for a given time step, then each of these is altered to the values given by

$$s_{ij} = s_{ij}^* f(\epsilon^p) \quad (17)$$

where for  $\Delta\epsilon_{fail}^p = 0$ ,

$$f(\epsilon^p) = \begin{cases} 1 & ; \quad \epsilon^p \in [0, \epsilon_{onset}^p] \\ 0 & ; \quad \epsilon^p \in (\epsilon_{onset}^p, \infty) \end{cases} \quad (18a)$$

while for  $\Delta\epsilon_{fail}^p > 0$ ,

$$f(\epsilon^p) = \begin{cases} 1 & ; \epsilon^p \in [0, \epsilon_{onset}^p] \\ 1 - \frac{\epsilon^p - \epsilon_{onset}^p}{\Delta\epsilon_{fail}^p} & ; \epsilon^p \in (\epsilon_{onset}^p, \epsilon_{onset}^p + \Delta\epsilon_{fail}^p) \\ 0 & ; \epsilon^p \in [\epsilon_{onset}^p + \Delta\epsilon_{fail}^p, \infty) \end{cases} \quad (18b)$$

The function  $f(\epsilon^p)$  is drawn in Figure 37. Here  $\epsilon_{onset}^p$  is the value of equivalent plastic strain  $\epsilon^p$  that existed in the element at the time step in which the Zener-Hollomon criterion was first met.  $\epsilon_{onset}^p$  is therefore computed by the code. On the other hand,  $\Delta\epsilon_{fail}^p$  is a user-prescribed material property.  $(\epsilon_{onset}^p + \Delta\epsilon_{fail}^p)$  is the level of  $\epsilon^p$  beyond which the element no longer supports deviatoric stresses.

The post-onset conditions imposed on an element that has failed according to the tension model are more stringent than those imposed on elements that have failed by the shear band model. In the former case hydrostatic tensile stress as well as deviatoric stresses are affected, and stress reduction to zero is instantaneous. For this reason, elements that have failed by shear banding continue to be checked for tensile failure.

**8.2 Problem Series III Through VIII.** Six problem series are run with the tensile and shear band failure models both operative. In each series parameter  $p_{fail}$  is fixed at -3.00 GPa for both RHA and copper, and  $\Delta\epsilon_{fail}^p$  is fixed at either 0.00, 0.10, 0.25, 0.50, 0.75 or 1.00.  $\epsilon_{erode}^p$  is again varied over the range of 0.25, 0.50, 0.75, 1.25, and 2.00 within each series, with the same value for  $\epsilon_{erode}^p$  assigned to both slidelines.

Problem Series III, IV, V, VI, VII and VIII correspond to a  $\Delta\epsilon_{fail}^p$  of 0.00, 0.10, 0.25, 0.50, 0.75 and 1.00, respectively. Problem Series III, for which  $\Delta\epsilon_{fail}^p = 0.00$ , is the case of instantaneous reduction of deviatoric stresses to zero upon shear band failure in an element. This is the case governed by Equation (18a). At the other extreme, Problem Series VIII, for which  $\Delta\epsilon_{fail}^p = 1.00$ , allows gradual stress reduction following satisfaction of the Zener-Hollomon condition, as governed by Equation (18b). In this series zero stresses are not imposed within an element until  $\epsilon^p$  exceeds  $\epsilon_{onset}^p$  by 1.00. Results for  $\bar{r}_{hole}$ ,  $\Delta M$  and  $t_{.95}$  from the six

problem series are presented in Table 5.

Figure 38 plots  $\bar{r}_{hole}$  vs.  $\epsilon_{erode}^p$  for the six series. Here  $\Delta\epsilon_{fail}^p$  is a constant parameter for each curve. On the other hand Figure 39 plots  $\bar{r}_{hole}$  vs.  $\Delta\epsilon_{fail}^p$  with  $\epsilon_{erode}^p$  a constant parameter for each curve. For each series, corresponding to a fixed  $\Delta\epsilon_{fail}^p$ ,  $\bar{r}_{hole}$  is seen to increase with increasing  $\epsilon_{erode}^p$  for  $\epsilon_{erode}^p$  in the range of 0.25 to 2.00. Also,  $\bar{r}_{hole}$  decreases with increasing  $\Delta\epsilon_{fail}^p$  for  $\epsilon_{erode}^p$  in the range of 0.25 to 2.00, with a single exception: at an  $\epsilon_{erode}^p$  of 2.00,  $\bar{r}_{hole}$  *increases* when  $\Delta\epsilon_{fail}^p$  is increased from 0.75 to 1.00. With this one exception ignored, the finding means that the more gradually deviatoric stresses are reduced following the onset of shear band failure, the larger the final hole size.

Activation of the shear band failure model allows for a large increase in computed hole size over those obtained in Problem Series I and II. For the series with  $\Delta\epsilon_{fail}^p$  equal to 0.50, 0.75, and 1.0,  $\bar{r}_{hole}$  is still consistently at least slightly smaller than the experimental value of 18.2 mm. However, the curves in Figure 38 corresponding to Problem Series III, IV and V and respective  $\Delta\epsilon_{fail}^p$  values of 0.00, 0.10, and 0.25 intersect the experimental result at an  $\epsilon_{erode}^p$  of about 0.5, 0.7, and 1.0, respectively. Four problems that produce reasonably close agreement with experimental  $\bar{r}_{hole}$ , arranged in order of increasing  $\Delta\epsilon_{fail}^p$ , are Problem III-B ( $\epsilon_{erode}^p = 0.50$ ,  $\Delta\epsilon_{fail}^p = 0.00$ ), Problem IV-C ( $\epsilon_{erode}^p = 0.75$ ,  $\Delta\epsilon_{fail}^p = 0.10$ ), Problem V-D ( $\epsilon_{erode}^p = 1.25$ ,  $\Delta\epsilon_{fail}^p = 0.25$ ), and Problem VI-E ( $\epsilon_{erode}^p = 2.00$ ,  $\Delta\epsilon_{fail}^p = 0.50$ ). These four problems all produce  $\bar{r}_{hole}$  values within 4% of the experimental result.

Mesh plots are now used to observe the evolution in time of the solution to Problem III-B. Plots at 1.03, 2.01, 3.01, 4.03, 5.00, 10.01, 20.04, 50.04, 100.06, 150.05, 200.06, 250.04, 300.06, 450.05 and 500.02  $\mu s$  after impact are presented in Figures 40 through 54, respectively. The blue elements in Figure 40 indicate those copper elements that have failed in tension. The green elements of RHA in Figures 40 through 54 have failed by shear banding, and the aquamarine elements of RHA in Figures 42, 43 and 44 have failed successively by shear banding followed by tension. Figures 40, 41 and 42 show the penetration process prior to perforation. In these figures the target's hole is surrounded by RHA material that has failed by shear banding. By 3.01  $\mu s$ , this failed region has extended to the exit surface. A single aquamarine element of RHA is located on the exit surface in Figure 42, indicating that the phenomenon of spallation has occurred slightly before

perforation. Perhaps formation of the relatively small, early-time debris fragments noted in Section 3 on the basis of Figure 12 can therefore be attributed to the failure mechanism of tensile voids. According to Figures 42 and 43, perforation occurs between 3.01 and 4.03  $\mu$ s.

Once an element of RHA material adjacent to the current hole boundary has failed by shear banding, the stress reduction scheme of Equations (17) and (18) renders it prone to large deformation and hence susceptible to slideline erosion. Figures 40 through 54 show that in Problem III-B, every RHA element that fails by shear banding and that does not have at least two of its edges bounded by elements that have not failed is discarded via slideline erosion by 500  $\mu$ s. A comparison of Figures 48, 49 and 50 reveals that a substantial amount of RHA material is still eroding and contributing to the final hole size between 100 and 200  $\mu$ s after impact. It is suggested that the relatively large, late-time fragments noted in Section 3 to be present in the radiographs of Figure 12 are primarily attributable to the failure mechanism of shear banding rather than tensile voids. Figures 51 and 52 show that the last failure by shear banding occurs between 250 and 300  $\mu$ s in a single element located near the entrance surface. This element and one of its neighbors erode from the target plate at between 450 and 500  $\mu$ s after impact, as is clear from Figures 53 and 54. This is the final occurrence of slideline erosion observed in Figures 40 through 54.

The mesh at 500  $\mu$ s shown in Figure 54 is taken to be the final state for Problem III-B. This figure therefore contains a prediction of the final hole geometry and the final spatial distribution of shear bands within a cross-section. Comparison with Figure 11 shows that this predicted hole geometry agrees quite closely with the experimental result, both in terms of the average hole radius  $\bar{r}_{hole}$  and the general shape of the hole profile. In particular Figure 54 contains a prominent protuberance that juts into the hole to form a distinguishable throat at about the midsurface elevation.

Mesh plots at 500  $\mu$ s from Problems IV-C, V-D and VI-E, which also agree closely with experiment in terms of  $\bar{r}_{hole}$ , are shown in Figures 55, 56 and 57, respectively. As with Problem III-B, green elements indicate shear banding failure, and the single aquamarine element in Figure 57 indicates shear banding failure followed by tensile void failure. Figures 54 through 57 reveal a trend in the number

of RHA elements that have failed by shear banding and that remain attached to the plate at 500  $\mu$ s. As  $\Delta \epsilon_{fail}^p$  is increased in the range of 0.00 to 0.50, the number of these elements also increases. In other words the number of RHA elements able to escape slideline erosion at 500  $\mu$ s increases as the rate at which deviatoric stresses are reduced following the onset of shear banding decreases. Note that  $\epsilon_{erode}^p$  is not held fixed in these four problems.  $\epsilon_{erode}^p$  equals 0.50, 0.75, 1.25 and 2.00 in Problems III-B, IV-C, V-D and VI-E, respectively. What is held approximately fixed is  $\bar{r}_{hole}$ .

Next the mesh plots at 500  $\mu$ s from Problems III-B, IV-C, V-D and VI-E are examined in terms of their predicted locations of tensile voids and shear bands. These observations are compared with the experimental results from Rd. 10771 in Figure 27. Figures 54, 55 and 56 contain no elements that have failed by tensile voids, a result that is clearly inconsistent with the experimental presence of voids in Figure 27. Figure 57 contains only a single element that has failed in this manner, so that Problem VI-E has also yielded an insufficiently large region of plate cross-section that has failed by voids. However, the location of this single element, near the intersection of the hole boundary with the plate's midsurface, does constitute a certain degree of agreement with experiment, since in Figure 27 all voids reside within the midsurface protuberance.

The calculations are more successful in terms of predictions of shear band locations in the final cross-section. Figure 54 from Problem III-B does display some shear banding within the midsurface-region protuberance that forms the throat. This is the region in which most shear bands are observed in Figure 27. However, Figure 54 does not display shear banding along the boundary of this protuberance, where it is conspicuous in Figure 27. Figure 54 also displays shear banding near the intersection of the hole boundary and the entrance surface, consistent with Figure 27. Two elements of shear banding are also contained in Figure 54 near the intersection of the hole boundary and the exit surface. This last result is inconsistent with Figure 27. However, the caveat stated in Section 6 should be recalled. The shear bands denoted in Figure 27 are those that were observable with an optical microscope at 1000X magnification. Perhaps additional shear bands could have been observed in these and other regions of the cross-section by more discriminating means. Thus in effect Figure 27 constitutes a lower bound on the number of shear bands present in the experiment.

Figure 55 from Problem IV-C contains a cylindrical ring about 5 mm thick in which shear bands are distributed rather uniformly. Thus there is little dependence on the density of shear bands with elevation  $z$  predicted for this problem. This is inconsistent with the preponderance of shear bands located near the midsurface elevation in Figure 27. The number of shear-banded elements within the cylindrical ring is about four times the total number contained in Figure 54. The general impression is that a larger portion of the cross-section in Figure 55 has failed by shear banding than in the experimental cross-section of Figure 27, but the caveat of Section 6 must again be borne in mind. Figure 55 contains a single shear-banded element at the exit surface and about 18 mm from the hole boundary. Figure 56 from Problem V-D shows a hole profile that is "flatter", or has less  $z$  dependence, than in Figures 54 and 55. Shear banding is predicted in Figure 56 along most of the hole boundary. Within a 5-mm-thick cylindrical ring adjacent to the hole boundary, a larger percentage of elements have shear banded in Figure 56 than in Figure 55. In Figure 57 from Problem VI-E, the corresponding 5-mm-thick ring has almost entirely failed by shear banding. In both Figures 56 and 57, the portion of the cross-section that has failed by shear banding clearly exceeds the experimental result of Figure 27.

Figures 58 through 63 plot cumulative mass lost by the target plate as a function of time after impact for Problem Series III, IV, V, VI, VII and VIII, respectively. In Figure 58 the curve for which  $\epsilon_{erode}^p = 0.50$  corresponds to Problem III-B. This curve can be divided into four regions. For the first 25  $\mu s$  after impact, mass loss occurs at the rapid average rate of  $1.9 \text{ g } \mu s^{-1}$ . The average mass loss rate between 25 and 100  $\mu s$  is  $0.52 \text{ g } \mu s^{-1}$ . From 100 to 200  $\mu s$ , the average rate further reduces to the still appreciable  $0.17 \text{ g } \mu s^{-1}$ . This is consistent with the continuing mass loss detected in the mesh plots of Figures 48, 49 and 50. By 200  $\mu s$  the curve has reached a plateau; no additional erosion occurs until 489.8  $\mu s$ , consistent with the observations based on the mesh plots in Figures 50 through 54.

The value attained at 500  $\mu s$  by each curve in Figures 58 through 63 is identified with  $\Delta M$ , the cumulative mass that the plate has lost during the 500  $\mu s$  following initial impact. These results for  $\Delta M$  are plotted vs.  $\epsilon_{erode}^p$  with  $\Delta \epsilon_{fail}^p$  a parameter in Figure 64 and vs.  $\Delta \epsilon_{fail}^p$  with  $\epsilon_{erode}^p$  a parameter in Figure 65.

Figures 64 and 65 show that in each of the Problem Series III through VIII,  $\Delta M$  increases with increasing  $\epsilon_{erode}^p$  for  $\epsilon_{erode}^p$  in the range of 0.25 to 2.00. These figures also show that for  $\epsilon_{erode}^p$  fixed at 0.25, 0.50, 0.75, 1.25 or 2.00,  $\Delta M$  decreases as  $\Delta \epsilon_{fail}^p$  is increased in the range of 0.00 to 1.00.  $\Delta M$  has been dramatically increased over the values obtained in Problem Series I and II by the activation of the shear band model. Thus whereas  $\Delta M$  results from Problem Series I and II never exceeded 28.6 g, in Figure 64 the curves pertaining to Problem Series III, IV and V intersect the experimental result of 136 g at an  $\epsilon_{erode}^p$  of about 0.8, 1.1 and 1.6, respectively. The curves for Problem Series VI, VII and VIII remain below this experimental result throughout the  $\epsilon_{erode}^p$  range of 0.00 to 2.00.

Recall that similar observations were made for  $\bar{r}_{hole}$  on the basis of Figures 38 and 39, which resemble Figures 64 and 65. In Figure 38 the curves of  $\bar{r}_{hole}$  vs.  $\epsilon_{erode}^p$  from Problem Series III, IV and V also intersected the experimental result of 18.2 mm, but at the lower  $\epsilon_{erode}^p$  values of about 0.5, 0.7 and 1.0, respectively. As a consequence of this difference, Problems III-B, IV-C, V-D and VI-E, which all produced  $\bar{r}_{hole}$  values within 4% of the experimental result, are now seen in Table 5 to produce  $\Delta M$  values that are smaller than the experimental result by 22%, 18%, 18% and 30%, respectively. These discrepancies between computed  $\Delta M$  values from Problems III-B, IV-C, V-D and VI-E and the experimental result of 136 g are attributed to the removal of insufficient RHA material in these four problems, despite the fact that the final hole radius displays close agreement with experiment in each case. Apparently too much RHA material has been compressed or bent and retained in the calculations instead of being discarded by slideline erosion.

The problem which produces a  $\Delta M$  result in closest agreement with experiment is Problem III-C.  $\Delta M$  for this problem is 130.3 g (Table 5), which is only 4% less than the experimental result of 136 g. The  $\bar{r}_{hole}$  value obtained from Problem III-C is 20.2 mm, which is 11% larger than the experimental result of 18.2 mm. Thus the correct amount of RHA material has been retained in Problem III-C, but the final hole radius is somewhat larger than in the experiment.

The four problems that produce  $\Delta M$  results in closest agreement with experiment after Problem III-C are Problems IV-C, IV-D, V-D and V-E. The  $\Delta M$  values computed for these problems agree with the experimental measurement from Rd. 4190 to within 18%, 12%, 18% and 16%, respectively. However, as with

Problem III-C, these four problems also produce  $\bar{r}_{hole}$  values larger than the experimental result of Equation (1), by 3%, 20%, 4% and 23%, respectively. Recall that Problems IV-C and V-D were previously noted to have produced  $\bar{r}_{hole}$  values in good agreement with experiment. The meshes at 500  $\mu$ s for these two problems were presented in Figures 55 and 56.

Return now to the mass loss vs. time plots of Figures 58 through 63, applicable to Problem Series III through VIII, respectively. When these are compared with the mass loss vs. time plots from Problem Series I and II, contained in Figures 23 and 36, respectively, it becomes apparent that activation of the shear band model has greatly extended the time at which target erosion comes to completion. In fact on the basis of Figures 58 through 63, some of the problems in Problem Series III through VIII still appear to be undergoing gradual additional erosion of RHA at 500  $\mu$ s after impact. Results for  $t_{.95}$ , the time at which the plate has lost 95% of mass  $\Delta M$ , are listed in Table 5. All  $t_{.95}$  listings for Problem Series III through VIII satisfy the experimental bound of Equation (3).  $t_{.95}$  results in Table 5 do not exhibit a simple dependence on either  $\epsilon_{erode}^p$  or  $\Delta\epsilon_{fail}^p$ .

## 9. EXAMINATION OF RESULTS' SENSITIVITY TO MESH FINENESS

All calculations thus far have employed the initial meshes for the jet particle and the RHA target plate that are shown in Figure 15. A question that arises is to what extent the results presented above for the eight problem series have been spuriously determined by the geometry of this mesh, rather than by the modeling of the various physical phenomena in the problem. In order to pursue this question, Problems I-C, II-C, and III-B will be rerun, this time using the same mesh for the jet particle as in Figure 15, but with a finer RHA target mesh. The new mesh, shown in Figure 66, consists of isosceles right triangles that are similar to those of Figure 15, but with their longest edge length equal to 0.65 mm, or one-half the longest edge length of each target element in Figure 15. Thus the total number of RHA elements has been quadrupled over that in Figure 15, from 3200 to 12800. There are now twenty layers of crossed triangles through the plate's thickness. These new problems, employing the mesh of Figure 66, are called Problems I-C(R), II-C(R), and III-B(R).

Problem I-C(R) has neither failure model activated and cutoff erosion strain  $\epsilon_{erode}^p$  set to 0.75 for both slidelines. Mesh plots from this problem at 3.00, 4.00 and 500.02  $\mu$ s after impact are displayed in Figures 67, 68 and 69, respectively. These can be compared with Figures 16, 17 and 18, which apply to Problem I-C at similar times. Hole geometries from the two problems are in reasonable agreement at the two earlier times. Perforation occurs at between 3 and 4  $\mu$ s in both cases. At 500  $\mu$ s, the final average hole radius,  $\bar{r}_{hole}$ , is slightly smaller in Problem I-C(R) than in Problem I-C, and hence a little further from the experimental result of 18.2 mm.  $\bar{r}_{hole}$  is determined to be 9.7 mm from Figure 69 and 11.0 mm from Figure 18, for a difference of 13%. In addition the mesh at 500  $\mu$ s contains more prominent lips at the intersections of the hole boundary with the entrance and exit surfaces in Problem I-C(R) than in Problem I-C.

The total mass lost by the target plate is plotted as a function of time for both Problems I-C and I-C(R) in Figure 70. After the initial 3  $\mu$ s, this quantity is seen to be consistently smaller in Problem I-C(R) than in Problem I-C. The total mass loss at 500  $\mu$ s,  $\Delta M$ , is 21.3 g in the former and 27.7 g in the latter problem. The difference here is 30%. The time at which 95% of  $\Delta M$  has been lost,  $t_{.95}$ , is determined to be 49.9  $\mu$ s in Problem I-C(R). This is 210.% larger than the value of 16.1  $\mu$ s determined for Problem I-C, but still smaller than the experimental bound of Equation (3). Results for  $\bar{r}_{hole}$ ,  $\Delta M$  and  $t_{.95}$  from Problem I-C(R) are collected in Table 6.

Problem II-C(R) has the tensile void failure model activated for OFHC copper and RHA steel, with material parameter  $p_{fail}$  set to -3.00 GPa for both metals. The cutoff strain for slideline erosion,  $\epsilon_{erode}^p$ , is set to 0.75 for both slidelines, as in Problem I-C(R). Mesh plots from Problem II-C(R) at 1.00, 3.01 and 500.00  $\mu$ s after impact are presented in Figures 71, 72 and 73, respectively. These are comparable with Figures 28, 29 and 30, showing mesh plots from Problem II-C at corresponding times. In general good qualitative agreement with the earlier problem is obtained. At 1.00  $\mu$ s, failed copper elements are seen near the leading edge of the jet particle. In contrast to Problem II-C, a single failed element of target material occurs as well, at the entrance surface of the hole boundary. At 3.01  $\mu$ s, the phenomenon of spallation, as visualized by the presence of failed target elements near the exit surface, is observed again. The spall fracture surface seems to be recessed by very roughly one element layer, or 0.6 mm, from the exit surface

in Problem II-C(R), an effect that could not be resolved with the coarser mesh of Problem II-C. At 500  $\mu$ s, both Figures 30 and 73 reveal a small region of RHA that has failed in tension. This region is located near the intersection of the hole boundary with the plate's midsurface in both figures. As mentioned in Section 7, this location of tensile failure is consistent in a general sense with Figure 27, which shows voids scattered about the midsurface protuberance. The hole radius at 500  $\mu$ s in Problem II-C(R) agrees closely with that from Problem II-C from the exit surface to the vicinity of the midsurface. Between the midsurface and the entrance surface, the hole radius at 500  $\mu$ s is slightly smaller in Problem II-C(R) than in Problem II-C.  $\bar{r}_{hole}$ , the radius averaged over the thickness, is 10.2 mm in Problem II-C(R), as opposed to 10.9 mm in Problem II-C. The difference between  $\bar{r}_{hole}$  values from Problems II-C(R) and II-C is 7%. Both are much smaller than the experimental value of 18.2 mm.

A comparison of Figures 69 and 73 shows that with this finer mesh, activation of the tensile void failure model has caused the final hole radius to grow slightly throughout most of the target plate thickness. The average radius,  $\bar{r}_{hole}$ , is 9.7 mm in Problem I-C(R) and 10.2 mm in Problem II-C(R). Recall from Section 7 that with the coarser mesh, a very small decrease in  $\bar{r}_{hole}$  was found to accompany activation of this model;  $\bar{r}_{hole}$  was 11.0 mm in Problem I-C and 10.9 mm in Problem II-C.

Figure 74 presents plots of cumulative mass lost by the target plate vs. time for Problems II-C and II-C(R). According to this figure, the mass loss is smaller in Problem II-C(R) than in Problem II-C at all times after 5  $\mu$ s. This is reminiscent qualitatively of the relationship between mass loss results from Problems I-C and I-C(R). Quantitatively, however, the difference between mass loss results obtained with the finer mesh and with the coarser mesh is less in Figure 74 than in Figure 70 throughout this time range. The cumulative mass lost at 500  $\mu$ s,  $\Delta M$ , is seen in Figure 74 to be 27.2 g for Problem II-C and 23.1 g for Problem II-C(R), for a difference of 18%. Both are much smaller than the experimental result of 136 g.  $t_{.95}$ , the time at which the target plate has lost cumulative mass equal to 95% of  $\Delta M$ , equals 22.7 and 28.1  $\mu$ s for Problems II-C and II-C(R), respectively. These times differ from each other by 24% and are both much earlier than the experimental bound of Equation (3). Note that  $\Delta M$  from Problem II-C(R) is slightly larger than the value obtained from Problem I-C(R). This is consistent with the relationship

observed for  $\bar{r}_{hole}$  from the two problems.  $t_{.95}$  from Problem II-C(R) is less than the result from Problem I-C(R), and both are substantially smaller than the experimental bound. Results for  $\bar{r}_{hole}$ ,  $\Delta M$  and  $t_{.95}$  obtained from Problem II-C(R) are added to Table 6.

Problem III-B(R) has the shear band failure model activated for the RHA in addition to the tensile void failure model for both OFHC copper and RHA with  $p_{fail}$  set to -3.00 GPa. Shear band parameter  $\Delta \epsilon_{fail}^p$  is set to 0.00, and cutoff erosion strain  $\epsilon_{erode}^p$  is set to 0.50 for both slidelines. Recall that Problem III-B, the counterpart of Problem III-B(R) with the coarser mesh, gave particularly satisfying agreement with experiment in terms of the final hole geometry. A question that comes up now is to what extent that agreement is preserved with the finer mesh in Problem III-B(R). Mesh plots from Problem III-B(R) are presented at 1.01, 2.01, 3.01, 4.00, 5.02, 10.02, 20.01, 50.03, 100.01, 200.02 and 500.01  $\mu s$  after impact in Figures 75 through 85. These can be compared with Figures 40 through 48, 50 and 54, which pertain to similar times for Problem III-B. Mesh plots at times prior to perforation are in good qualitative agreement. Spallation in the target plate is again observed at 3  $\mu s$  for both meshes. The radial extent of the spall fracture surface is about 4 mm in Problem III-B(R) and only about 1 mm in Problem III-B. Also, the spall fracture surface is recessed about 0.8 mm from the exit surface in Problem III-B(R), while no such recession can be resolved with the coarser mesh of Problem III-B.

Following perforation, mesh plots from Problem III-B(R) continue to display good qualitative agreement with those from Problem III-B through 10  $\mu s$ , both in terms of the hole boundary's geometry and the general location of zones of elements that have failed. At 4 and 5  $\mu s$ , a small zone of elements that have failed in tension subsequent to failure by shear banding exists at roughly the same location in both problems. Furthermore, by 10  $\mu s$  this zone has eroded away in both problems.

By 20  $\mu s$  after perforation, differences in hole profiles from Problems III-B and III-B(R) become apparent and seem to be driven by differences in the spatial distributions of zones of RHA that have failed by shear banding. For example, as was noted in Section 8, a midsurface-level protuberance remains present in the mesh at 500  $\mu s$  in Problem III-B (Figure 54). This feature is in good agreement with the experimental hole profile of Figure 11 and shows promise of being preserved in

Problem III-B(R) on the basis of the mesh plot at 20  $\mu$ s (Figure 81). In this figure a group of RHA elements which have not failed is seen to jut out into a region of failed elements which line the hole boundary. However, erosion of this group of unfailed elements occurs between 50 and 100  $\mu$ s (Figures 82 and 83). This erosion is assisted by the presence of contiguous failed elements located at about midsurface elevation and radially outward from the group of unfailed elements in question. The result is that no prominent midsurface protuberance is present in the final mesh from Problem III-B(R) (Figure 85). Instead, the hole's main throat, or most narrow cross-section, occurs near the entrance surface, with a lesser throat occurring near the exit surface. The hole is relatively wide at midsurface elevation.  $\bar{r}_{hole}$ , the hole's radius averaged over the plate thickness at 500  $\mu$ s, is determined for Problem III-B(R) on the basis of nodal coordinates along the red portion of the target boundary in Figure 86. The result is 17.3 mm for  $\bar{r}_{hole}$ . This agrees reasonably well with the experimental result of 18.2 mm, despite the large difference between hole profile shapes in Figure 85 or 86 and Figure 11. It also agrees reasonably well with the result of 18.1 mm from Problem III-B. The difference amounts to a 5% reduction in  $\bar{r}_{hole}$  corresponding to a doubling in mesh fineness.

Next the locations of failed elements in Figure 85 from Problem III-B(R) will be examined in light of the mesh in Figure 54 from Problem III-B and of experimental results from Rd. 10771 that were discussed in Section 6. First note from Figure 85 that no elements that have failed by tensile voids have escaped slideline erosion by 500  $\mu$ s. This is inconsistent with the experimental result of Figure 27, which shows at least nine large, discrete voids distributed around the midsurface protuberance. Moreover there are no elements that have failed by tensile voids in the mesh at 50  $\mu$ s, either among elements in the midsurface that will shortly erode away or elsewhere (Figure 82). On the other hand the mesh in Figure 85 has retained numerous RHA elements that have failed by shear banding. These occur mainly in the vicinity of the hole boundary and between the entrance surface and the midsurface. In contrast Figure 54 shows a more uniform distribution of predicted shear bands with respect to elevation in the plate. Figure 27 from the experiment shows two or three shear bands detected near the entrance surface, consistent with a cluster of failed elements in Figure 85. Most of the shear bands in Figure 27 lie within the midsurface protuberance. This feature of the experimental distribution is more consistent with the mesh from Problem III-B(R) at 50  $\mu$ s than at 500  $\mu$ s.

Mass lost by the target plate is plotted as a function of time in Figure 87 for Problems III-B and III-B(R). At all times after 5  $\mu$ s, the mass loss in Problem III-B(R) is less than that in Problem III-B. At 500  $\mu$ s, the net mass loss,  $\Delta M$ , is 97.2 g in Problem III-B(R) and 105.5 g in Problem III-B (Table 5), corresponding to an 8.5% difference. This difference of 8.3 g bounds the difference at all earlier times. The percentage difference between  $\Delta M$  from the two problems is larger than that found above for the quantity  $\bar{r}_{hole}$ . This last comparison is correlated with the flatter hole profile (i.e., less  $z$  dependence of hole radius) at 500  $\mu$ s for Problem III-B(R) than for Problem III-B.

$t_{.95}$  is found from Figure 87 to be 158.3  $\mu$ s for Problem III-B(R). This represents a 13.7% decrease from the result of 183.4  $\mu$ s from Problem III-B (Table 5). These  $t_{.95}$  results from both problems satisfy the experimental bound of Equation (3).

The results for  $\bar{r}_{hole}$ ,  $\Delta M$  and  $t_{.95}$  from Problem III-B(R) are added to Table 6. Activation of the shear band failure model with the finer mesh has produced some of the same general effects as in Section 8 with the coarser mesh: The final perforation hole has grown substantially larger and has been placed in closer agreement with experiment in terms of size, as witnessed by results for  $\bar{r}_{hole}$  and  $\Delta M$ . Also, the duration of the hole growth process, as measured by  $t_{.95}$ , has been significantly increased over the results obtained with neither failure model or with only the tensile void model active and has been placed in agreement with the bound derived from the radiographs of Figure 12. The shape of the final hole profile from Problem III-B(R) is flatter than both the results from Problem III-B and from Rd. 10771. However, variation of the parameters  $\epsilon_{erode}^p$  and  $\Delta\epsilon_{fail}^p$  in series of problems with the finer mesh could presumably have recovered agreement with the experimental hole shape.

The final issue to consider is the added CPU times associated with the finer mesh. All calculations described in this report have been performed on the Cray X-MP/48 computer operated by the U.S. Army Ballistic Research Laboratory. The CPU times expended in running Problems I-C, I-C(R), II-C, II-C(R), III-B and III-B(R) out to 500  $\mu$ s are listed in Table 7. CPU times for Problems I-C and II-C are very similar, as are those for Problems I-C(R) and II-C(R). Thus for both the coarser and the finer target mesh, activation of only the tensile void failure model

has been accompanied not only by little effect on results for  $\bar{r}_{hole}$ ,  $\Delta M$  and  $t_{.95}$ , but also by little increase in required CPU time. In contrast, for both meshes activation of the shear band failure model has been accompanied by substantial reduction in required CPU time. The main reason for this reduction is probably related to the time step, determined in EPIC-2 by means of the Courant stability condition (Johnson 1976). According to this condition, at any given time in the calculation the time step is limited by the current dimensions of the smallest non-eroded element. In problems with the shear band failure model active, more target elements become eroded and fewer highly distorted elements remain attached to the plate. This prevents the time step from becoming as small as in the other problems. Doubling the mesh fineness is seen in Table 7 to have increased the required CPU time by factors of 7.7, 7.8 and 9.0 in the case of Problems I-C, II-C and III-B, respectively. A factor of 8.0 increase was anticipated on the basis of two considerations: (i) Halving the initial element dimensions very roughly halves the time step throughout the course of the calculation. (ii) Quadrupling the number of elements very roughly quadruples the number of operations required at each time step.

The salient results from this section can be briefly summarized as follows: For each of the three problems run with the finer mesh of Figure 66, the final hole size, as measured both by  $\bar{r}_{hole}$  and  $\Delta M$ , is smaller than the result from the counterpart problem with the coarser mesh. The differences in terms of  $\bar{r}_{hole}$  are 13%, 7% and 5% for Problems I-C(R), II-C(R) and III-B(R), respectively. The differences in terms of  $\Delta M$  for these respective problems are 30%, 18% and 8.5%.  $\bar{r}_{hole}$  and  $\Delta M$  results from Problems I-C, II-C, I-C(R) and II-C(R) are all substantially smaller than the experimental results, while results for these quantities from Problems III-B and III-B(R) are all in reasonable agreement with experiment. Specifically,  $\bar{r}_{hole}$  and  $\Delta M$  are respectively 0.5% and 30.% smaller than the experimental results in the case of Problem III-B and respectively 5% and 40.% smaller in the case of Problem III-B(R). The final hole shape from Problem III-B is also in reasonable agreement with experiment, but the final hole profile from Problem III-B(R) is flatter than according to experiment. The quantity  $t_{.95}$  has been increased in the case of Problems I-C(R) and II-C(R) by 210.% and 24%, respectively, but decreased by 13.7% in the case of Problem III-B(R) relative to the values obtained with the coarser mesh. The results for  $t_{.95}$  from Problems I-C, II-C, I-C(R) and II-C(R) are smaller than in the experiment, while those from Problems III-B and III-B(R) are consistent with experiment. Corresponding to the doubling of target mesh fineness,

CPU times on a Cray X-MP/48 have increased by factors of 7.7, 7.8 and 9.0 in the case of Problems I-C, II-C and III-B, respectively.

The above-cited quantitative differences between results for  $\bar{r}_{hole}$ ,  $\Delta M$  and  $t_{.95}$  from Problems III-B and III-B(R) provide measures of the degree to which the mesh of Figure 15 is adequate for studying parametric dependencies of the solution upon  $\epsilon_{erode}^p$ ,  $p_{fail}$  and  $\Delta\epsilon_{fail}^p$ , as was done in Section 8. This degree of adequacy must be weighed against the added expense in CPU time associated with performing parametric studies with the finer mesh of Figure 66. For most researchers, CPU times given in Table 7 for problems involving the refined mesh are prohibitive for performing the numerous runs required for parametric studies. A rational basis for the use of the mesh in Figure 15 is therefore indicated.

## 10. CONCLUDING REMARKS

This report has discussed the modeling of a particular experiment, in which a shaped charge warhead was fired at 15.23-charge-diameter standoff into a 13.0-mm-thick RHA plate. Two quantities evaluated from the experiment and that served as benchmarks for the calculations are  $\bar{r}_{hole}$ , the final hole radius averaged over the plate thickness, and  $\Delta M$ , the total mass lost by the plate. A third quantity, which was bounded on the basis of results from two experiments quite similar to Rd. 10771, is  $t_{.95}$ , the time after impact at which the plate has lost 95% of mass  $\Delta M$ . The experimental results obtained for  $\bar{r}_{hole}$ ,  $\Delta M$  and  $t_{.95}$  were 18.2 mm, 136 g, and the bound  $t_{.95} > 73.9 \mu s$ , respectively. A fourth benchmark was provided by a diagram showing locations of prominent voids and shear bands in a cross-section of the perforated plate from the original experiment.

A five-parameter geometric model for the leading jet particle was presented. Its parameters were evaluated on the basis of a radiograph. The particle's length, volume and centroid location were determined in the process.

Algorithms were developed to simulate material damage associated with the two micromechanical phenomena of voids and shear bands, both observed in micrographs of RHA specimens from the perforated plate. Each algorithm, or failure model, consists of an onset criterion and a post-onset prescription on stresses. The tensile void failure model, applied to both the OFHC copper of the

leading jet particle and the RHA steel of the target plate, introduces the parameter  $p_{fail}$  for each of the two metals.  $p_{fail}$  is the negative value of pressure which when reached in an element causes that element to thereafter be restricted from bearing any deviatoric stress or hydrostatic tension. The shear band failure model, applied only to the steel, employs as its onset criterion the Zener-Hollomon condition. This model introduces the single parameter  $\Delta\epsilon_{fail}^p$ , the additional equivalent plastic strain which a failed element can support beyond the level it had attained at the time of shear banding onset. These algorithms were installed into Lagrangian hydrocode EPIC-2.

A finite element mesh was developed for the leading jet particle and for the target plate. That for the target plate consisted of 3200 isosceles right triangles, each with its longest edge equal to 1.3 mm in length. The contact surface between the meshes for the leading copper jet particle and the RHA target plate were modeled by means of the eroding slideline algorithm contained in EPIC-2. This eroding slideline algorithm introduces the material parameter  $\epsilon_{erode}^p$ , a critical equivalent plastic strain, for each of OFHC copper and RHA steel. With these initial meshes fixed, eight series of five problems each were run. In each problem  $\epsilon_{erode}^p$  was assigned the same value for both materials.

The first series had neither failure model active for the two metals. The only parameter varied was  $\epsilon_{erode}^p$ , over the range of values 0.25, 0.50, 0.75, 1.25 and 2.00. All five problems predicted a plate hole that is smaller and whose formation is completed earlier than in the experiment. The largest values obtained for  $\bar{r}_{hole}$ ,  $\Delta M$  and  $t_{.95}$  in this series were 13.9 mm, 27.7 g, and 19.4  $\mu$ s, respectively, corresponding to respective  $\epsilon_{erode}^p$  values of 2.00, 0.75, and 2.00.

The experiment was then remodeled using EPIC-2 with only the tensile void failure model activated. Throughout this second problem series, parameter  $p_{fail}$  was assigned the value -3.00 GPa for both RHA and copper. Activation of the tensile void failure model alone did not significantly increase  $\bar{r}_{hole}$  or  $\Delta M$ . Neither was  $t_{.95}$  enlarged significantly, except for the case of  $\epsilon_{erode}^p$  equal to 2.00.

Activation of both the tensile void and the shear band failure models for Problem Series III through VIII did allow for substantial increases in  $\bar{r}_{hole}$ ,  $\Delta M$  and  $t_{.95}$ .  $p_{fail}$  was again fixed at -3.00 GPa for both metals. Each of the four problems

for which  $(\epsilon_{erode}^p, \Delta\epsilon_{fail}^p)$  was assigned the values (0.50, 0.00), (0.75, 0.10), (1.25, 0.25) or (2.00, 0.50) produced an  $\bar{r}_{hole}$  value within 4% of the experimental result. Of these four problems, the one involving (0.50, 0.00) produced the closest agreement with experiment in terms of the final hole profile's general shape and the final location of shear bands within a cross-section of the target plate. None of these problems predicted a sufficient portion of the plate's final cross-section to be taken up by voids. These four problems all yielded  $\Delta M$  results that were lower than that of the experiment, by 22%, 18%, 18% and 30%, respectively. Evidently more highly compressed and bent RHA material remained attached to the plate in the calculations than in the experiment. On the other hand it was found possible to produce closer agreement with experiment in terms of  $\Delta M$  by tolerating more deviation in  $\bar{r}_{hole}$ . Thus a fifth problem, for which  $(\epsilon_{erode}^p, \Delta\epsilon_{fail}^p)$  was set to (0.75, 0.00), produced a  $\Delta M$  result within 4% of experiment, but an  $\bar{r}_{hole}$  result that was 11% larger than according to experiment. All calculations performed with both failure models active yielded  $t_{.95}$  results consistent with the experimental bound.

As just described, the tensile void and shear band failure models, when used in conjunction with the slideline erosion algorithm and a particular mesh for the jet particle and the target plate, allowed EPIC-2 to produce reasonable agreement with a single experiment in terms of final hole geometry, the rate of hole formation, and the net mass lost by the target plate. Three problems were then rerun with a target mesh having double the fineness it had in all previous runs. One of these problems involved no failure modeling, one involved the tensile void failure model only, and the third involved both the tensile void and the shear band failure models. For the two problems involving no failure modeling or only tensile failure modeling, no significant changes in  $\bar{r}_{hole}$ ,  $\Delta M$  and  $t_{.95}$  were produced by doubling the target mesh fineness. The final perforation hole remained too small and its formation completed prematurely in comparison with experiment. The problem with both tensile and shear banding failure models active that was rerun was the case of  $\epsilon_{erode}^p$  and  $\Delta\epsilon_{fail}^p$  equal to 0.50 and 0.00, respectively. This is the case that with the original mesh gave best overall agreement with experiment in terms of  $\bar{r}_{hole}$ ,  $\Delta M$ ,  $t_{.95}$ , the final hole profile and shear band location within a plate cross-section. Results for this problem with the refined mesh showed reductions in  $\bar{r}_{hole}$ ,  $\Delta M$  and  $t_{.95}$  from values obtained with the original mesh by 5%, 8.5% and 13.7%, respectively. The final hole profile became flatter (i.e., less elevation dependence in hole radius) than with the original mesh. The location of shear bands also became less dependent on

elevation. For this problem with both failure models active, the CPU time required on a Cray X-MP/48 demonstrated a factor of 9.0 increase over the time required with the original mesh. In light of this increase, the solution obtained for this problem with the original was judged to be sufficiently accurate to be useful.

Possibilities for follow-up work will now be considered. In the present study the criteria of  $\bar{r}_{hole}$ ,  $\Delta M$  and  $t_{.95}$  agreement with experiment have not uniquely determined the proper set of input values for the three parameters  $\epsilon_{erode}^p$ ,  $p_{fail}$  and  $\Delta\epsilon_{fail}^p$ . In particular, with  $p_{fail}$  fixed at -3.00 GPa for both RHA and copper, agreement was obtained for a range of  $\epsilon_{erode}^p$  and  $\Delta\epsilon_{fail}^p$  combinations. This consideration motivated the recently conducted set of experiments involving various conditions of standoff and target plate thickness (Raftenberg 1991, 1992). The same type of shaped charge warhead used in the two experiments cited in this report was also employed throughout this newer set of experiments. The question raised is whether all experiments in this combined database can be reasonably well-matched in terms of  $\bar{r}_{hole}$ ,  $\Delta M$  and  $t_{.95}$  by a single set of input values for parameters  $\epsilon_{erode}^p$ ,  $p_{fail}$  and  $\Delta\epsilon_{fail}^p$ . If satisfactory agreement cannot be obtained or if the three parameters remain under-determined, some revision of the material models used in the calculations may be indicated. These would include the models for flow stress, tensile failure and shear banding failure.

Table 1. Parameter Values for the Leading Jet Particle's Geometric Model

Parameter	Value (mm)
$L_C$	4.77
$L_S$	12.75
$L_B$	3.08
$R_S$	2.40
$R_B$	3.30

Table 2. Material Parameter Values for the Metals

Material Parameter	OFHC Copper	RHA
$\rho_0$ (kg/m <sup>3</sup> )	8945.	7823.
$G$ (GPa)	46.31	77.50
$K_1$ (GPa)	137.2	163.9
$K_2$ (GPa)	175.1	294.4
$K_3$ (GPa)	564.2	500.0
$\Gamma$	1.96	1.16
$A$ (GPa)	0.08963	0.7922
$B$ (GPa)	0.2916	0.5095
$N$	0.31	0.26
$C$	0.025	0.014
$M$	1.09	1.03
$T_r$ (K)	294.3	294.3
$T_m$ (K)	1355.9	1793.2

Table 3. Results from Problem Series I  
(No Failure Modeling in RHA or Cu)

Problem	$\varepsilon_{erode}^p$	$\bar{r}_{hole}$ (mm)	$\Delta M$ (g)	$t_{.95}$ ( $\mu s$ )
I-A	0.25	9.6	27.1	15.9
I-B	0.50	10.3	27.4	16.4
I-C	0.75	11.0	27.7	16.1
I-D	1.25	12.1	23.4	15.6
I-E	2.00	13.9	20.3	19.4

Table 4. Results from Problem Series II  
(Tensile Failure Modeling in RHA & Cu,  $p_{fail} = -3.00$  GPa;  
No Shear Band Failure Modeling)

Problem	$\varepsilon_{erode}^p$	$\bar{r}_{hole}$ (mm)	$\Delta M$ (g)	$t_{.95}$ ( $\mu s$ )
II-A	0.25	9.7	27.9	10.5
II-B	0.50	10.6	28.6	15.3
II-C	0.75	10.9	27.2	22.7
II-D	1.25	12.2	24.9	23.1
II-E	2.00	15.0	22.8	89.3

Table 5. Results from Problem Series III Through VIII  
(Tensile Failure Modeling in RHA & Cu,  $p_{fail} = -3.00$  GPa;  
Shear Band Failure Modeling in RHA,  $\Delta\epsilon_{fail}^p$  Varied)

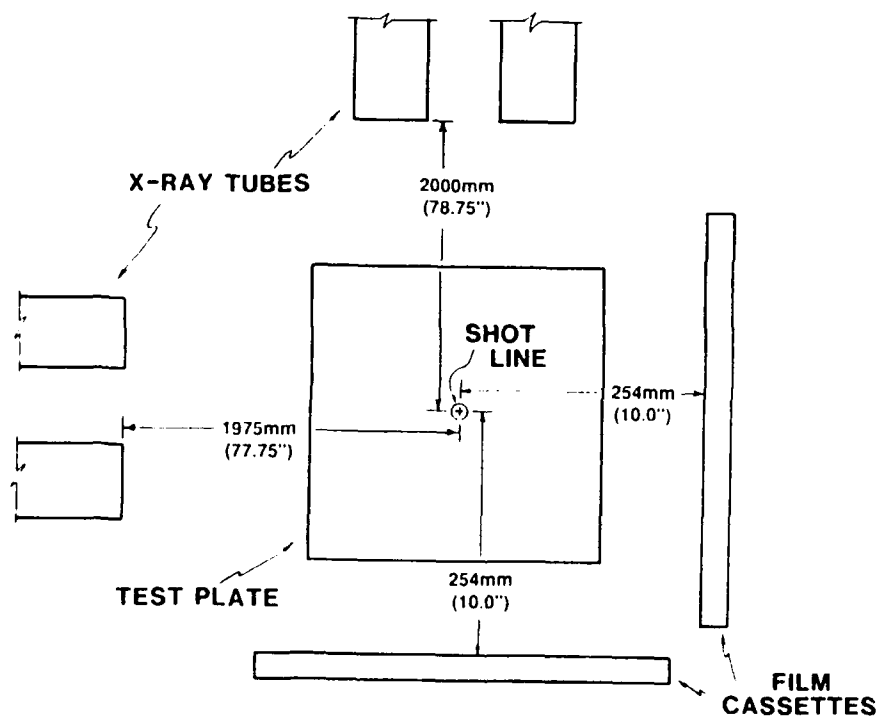
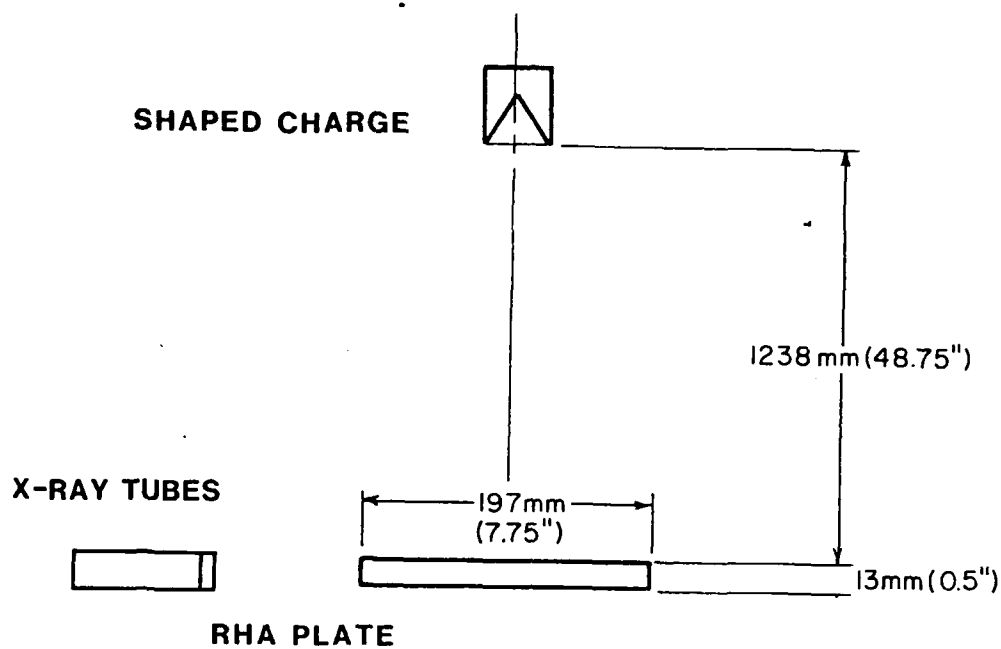
Problem	$\epsilon_{erode}^p$	$\Delta\epsilon_{fail}^p$	$\bar{r}_{hole}$ (mm)	$\Delta M$ (g)	$t_{.95}$ ( $\mu s$ )
III-A	0.25	0.00	15.5	76.1	224.7
III-B	0.50	0.00	18.1	105.5	183.4
III-C	0.75	0.00	20.2	130.3	192.3
III-D	1.25	0.00	23.2	171.4	323.3
III-E	2.00	0.00	26.3	220.7	267.7
IV-A	0.25	0.10	14.1	65.2	228.9
IV-B	0.50	0.10	16.2	83.3	228.4
IV-C	0.75	0.10	18.7	110.9	293.3
IV-D	1.25	0.10	21.9	152.5	332.7
IV-E	2.00	0.10	24.8	193.9	381.4
V-A	0.25	0.25	12.1	45.8	289.5
V-B	0.50	0.25	15.3	72.9	395.1
V-C	0.75	0.25	17.4	95.3	329.4
V-D	1.25	0.25	18.9	112.2	358.7
V-E	2.00	0.25	22.3	158.3	446.3
VI-A	0.25	0.50	11.5	40.5	305.9
VI-B	0.50	0.50	12.3	45.6	310.2
VI-C	0.75	0.50	13.1	49.5	212.7
VI-D	1.25	0.50	16.0	76.7	389.5
VI-E	2.00	0.50	17.7	94.8	81.6
VII-A	0.25	0.75	11.0	36.7	382.8
VII-B	0.50	0.75	11.9	40.8	267.6
VII-C	0.75	0.75	12.8	47.7	217.4
VII-D	1.25	0.75	14.9	63.8	192.2
VII-E	2.00	0.75	17.0	85.2	249.7
VIII-A	0.25	1.00	10.7	34.7	323.8
VIII-B	0.50	1.00	11.4	38.1	180.0
VIII-C	0.75	1.00	12.3	41.8	235.4
VIII-D	1.25	1.00	14.2	55.6	180.6
VIII-E	2.00	1.00	17.1	80.4	232.7

Table 6. Results with the Refined Mesh

Problem	$\epsilon_{erode}^p$	$\Delta\epsilon_{fail}^p$	$p_{fail}$ (GPa)	$\bar{r}_{hole}$ (mm)	$\Delta M$ (g)	$t_{.95}$ ( $\mu s$ )
I-C(R)	0.75	N.A.	N.A.	9.7	21.3	49.9
II-C(R)	0.75	N.A.	-3.00	10.2	23.1	28.1
III-B(R)	0.50	0.00	-3.00	17.3	97.2	158.3

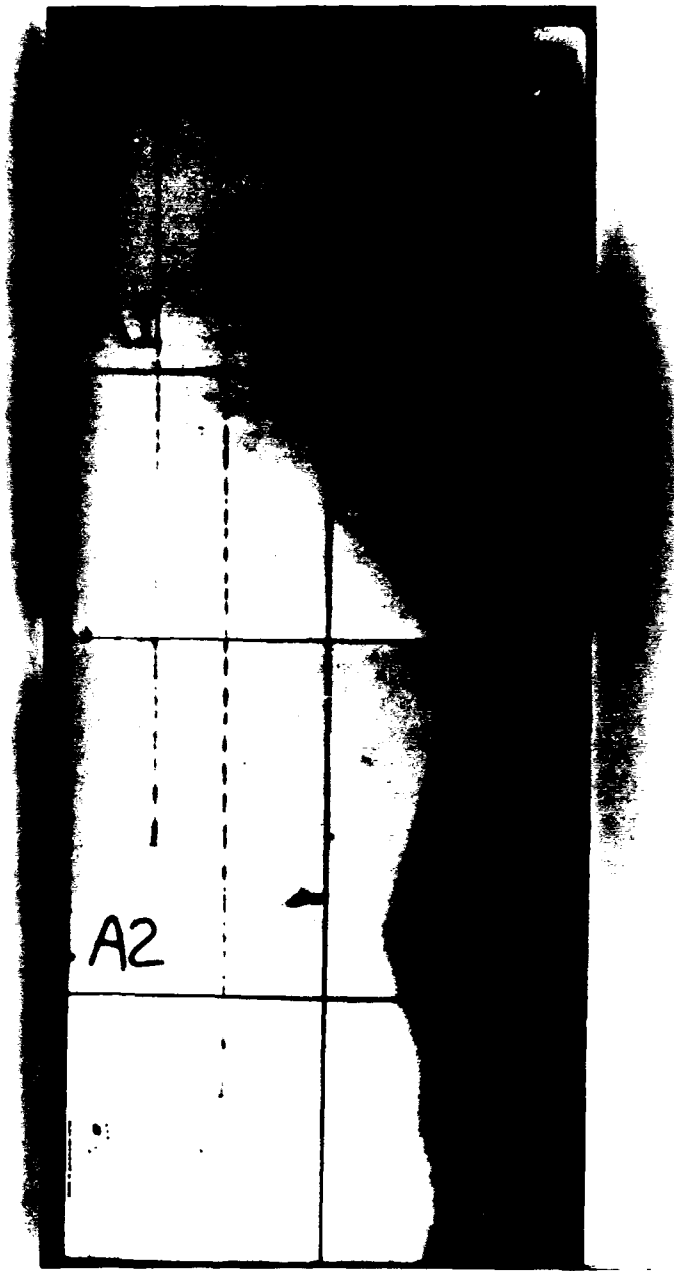
Table 7. CPU Times on a Cray X-MP/48 for Six Problems

Problem	$\epsilon_{erode}^p$	$\Delta\epsilon_{fail}^p$	$p_{fail}$ (GPa)	CPU Time (hrs)
I-C	0.75	N.A.	N.A.	0.93
I-C(R)	0.75	N.A.	N.A.	7.19
II-C	0.75	N.A.	-3.00	0.93
II-C(R)	0.75	N.A.	-3.00	7.27
III-B	0.50	0.00	-3.00	0.53
III-B(R)	0.50	0.00	-3.00	4.78



Note: Drawing is not to scale.

Figure 1. Experimental Setup for Rd. 10771.



Rd. 10771

Figure 2. Flash Radiographs of the Jet at 161.5 and 181.4  $\mu$ s After Explosive Initiation.



Rd. 10771

Figure 3. Flash Radiographs of the Jet and RHA Plate at 181.0 and 226.3  $\mu$ s After Explosive Initiation.



Rd. 10771

Figure 4. Enlargement of Flash Radiograph of the Jet and RHA Plate at 226.3  $\mu$ s After Explosive Initiation.



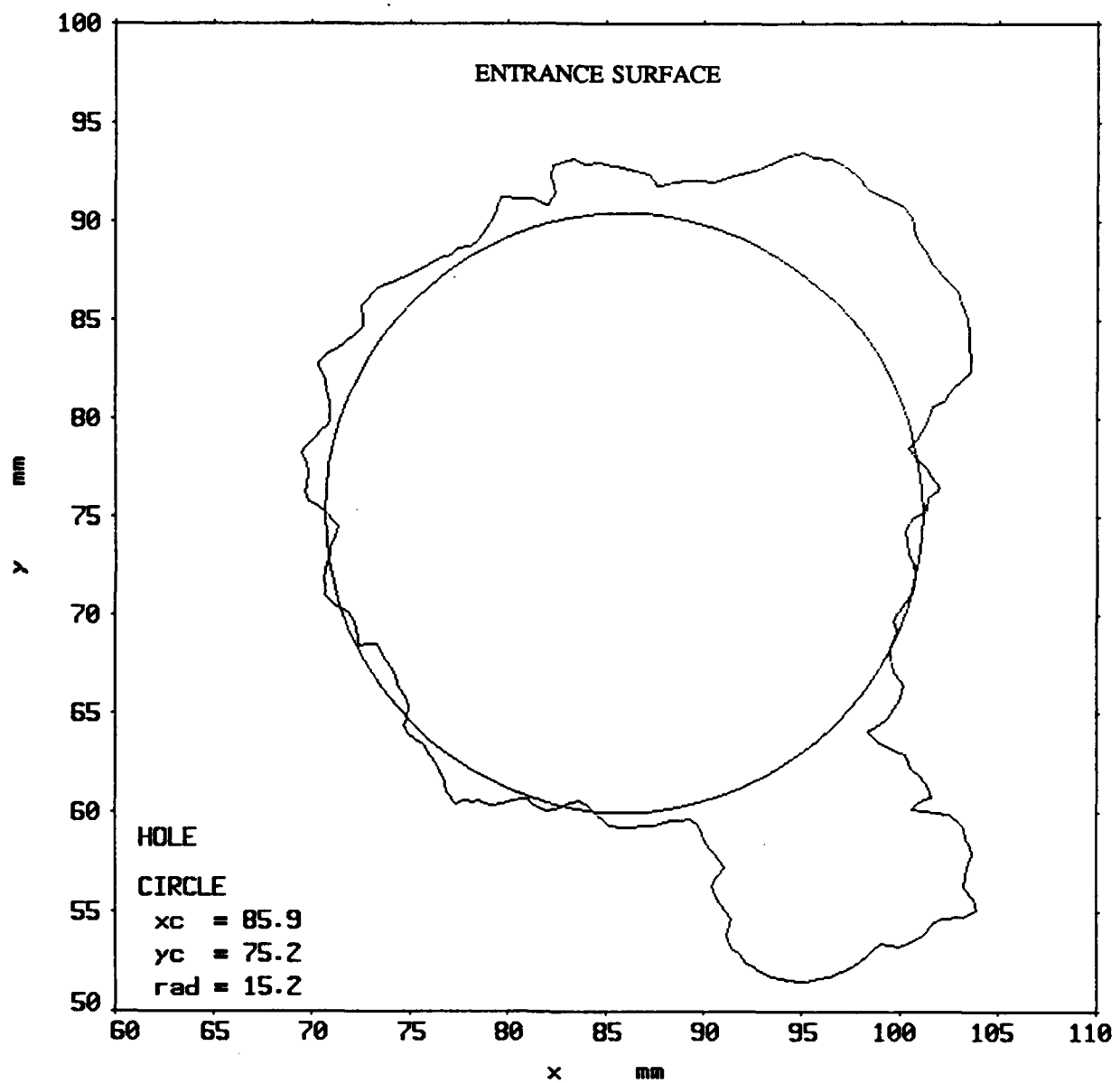
Rd. 10771

Figure 5. Photograph of the Perforated Plate's Entrance Surface.



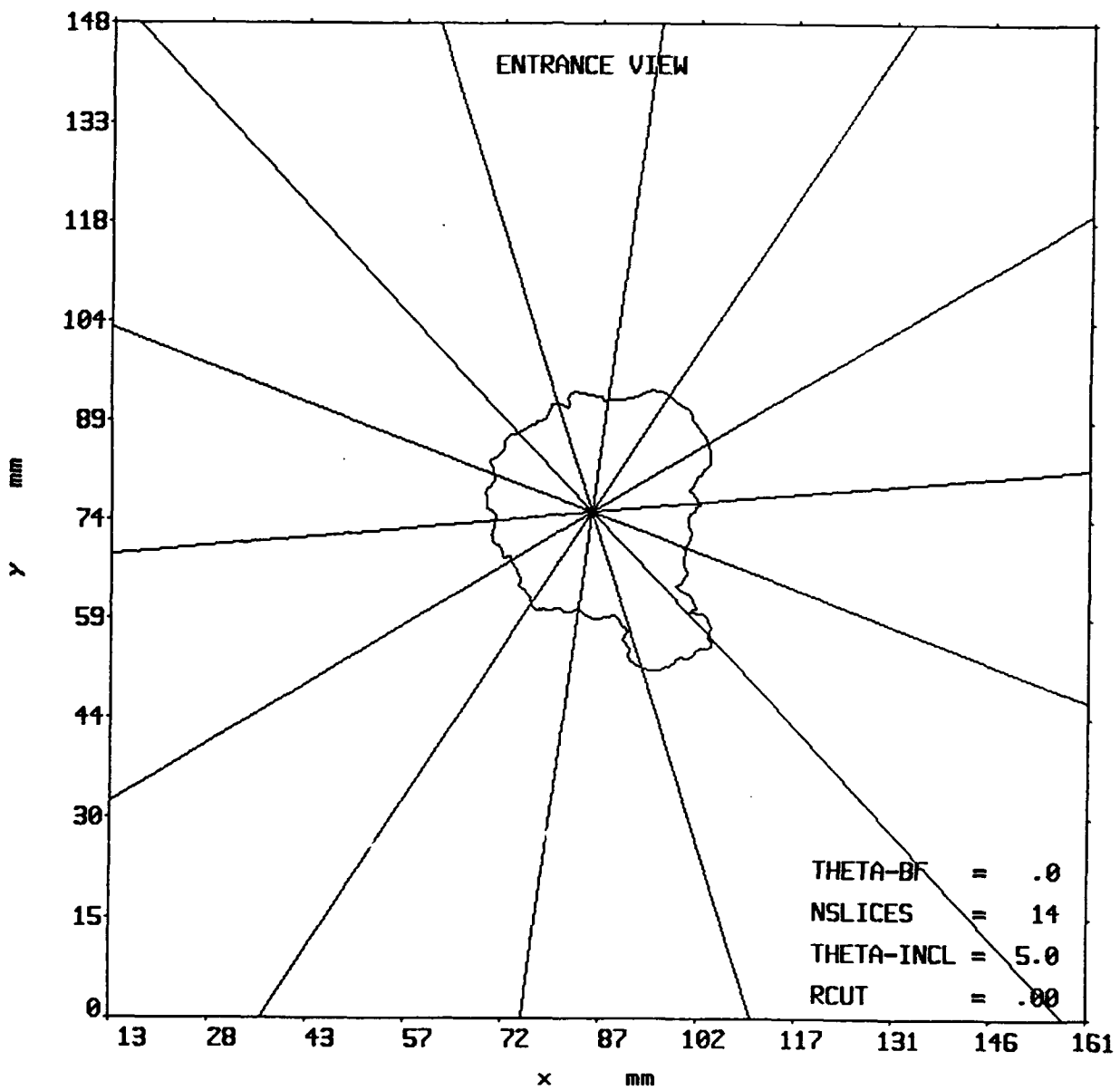
Rd. 10771

Figure 6. Photograph of the Perforated Plate's Exit Surface.



Rd. 10771

Figure 7. Perforation Hole in RHA Plate Fitted by a Circle.



Rd. 10771

Figure 8. Construction of Radial Slices to be Removed From Perforated Plate.

Rd 10771



10 9 8 7 6 5 4 3 2 1

Figure 9. Removal of Five Radial Slices From Perforated Plate.

Rd 10771

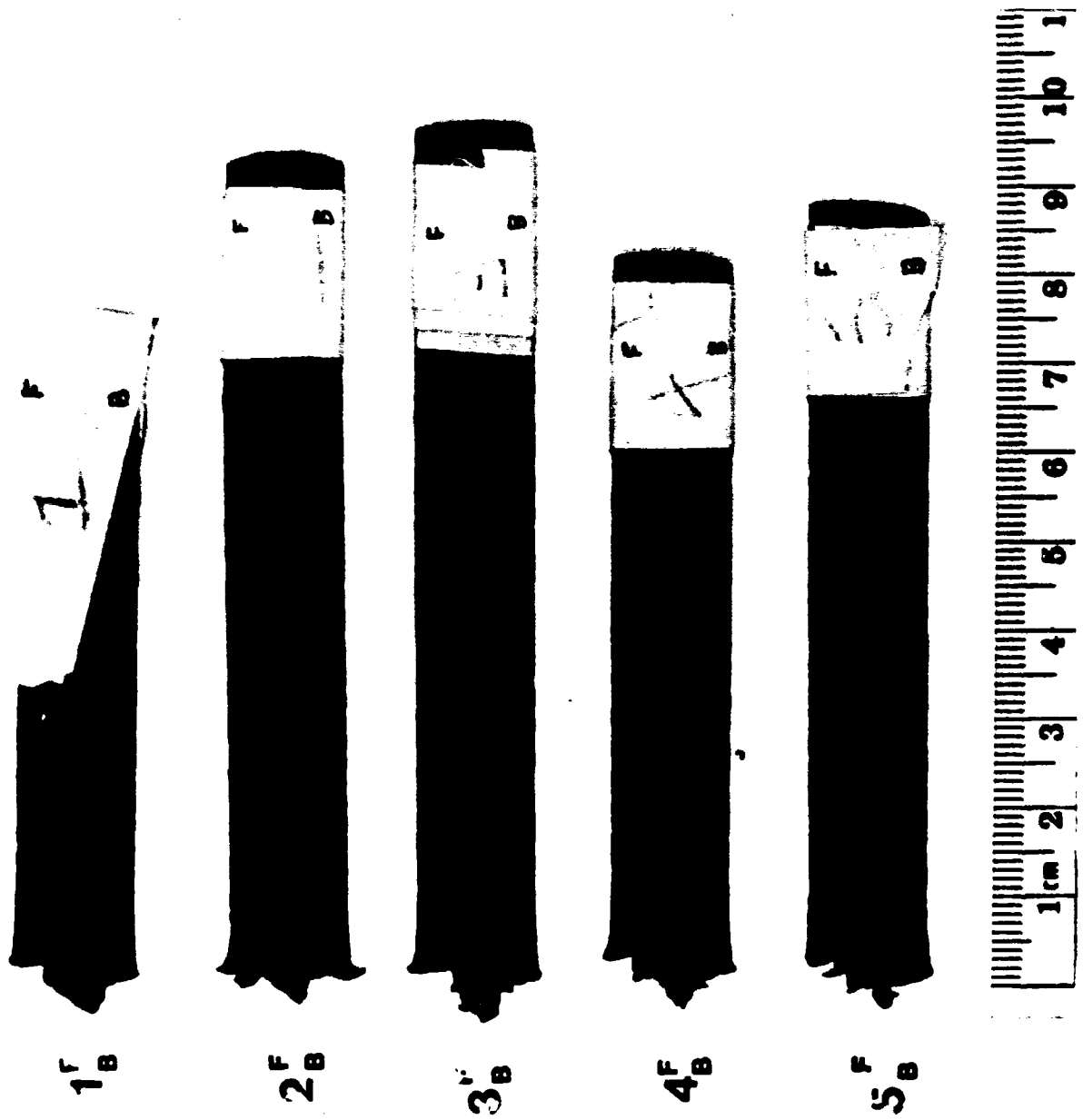
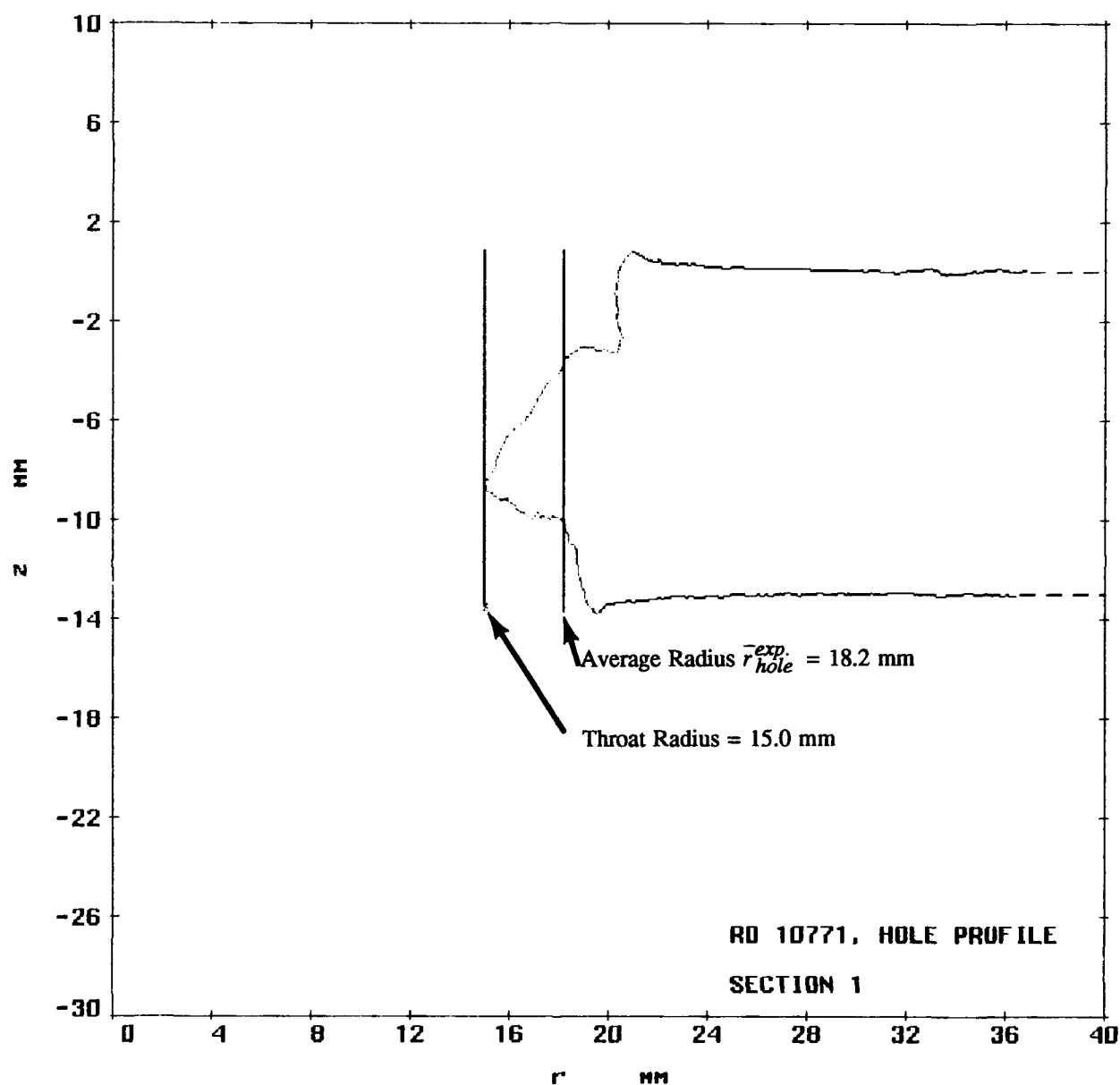


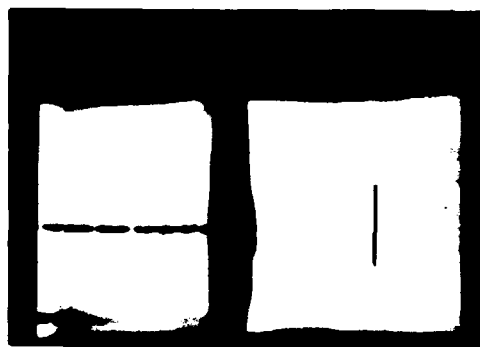
Figure 10. Five Radial Slices From the Perforated Plate.



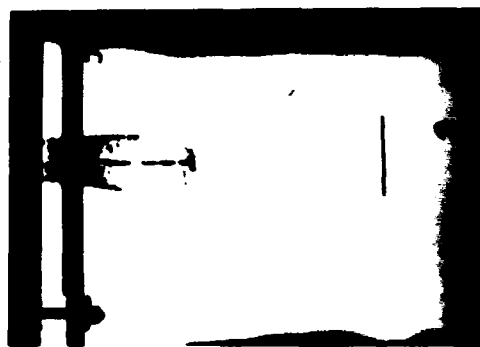
NOTE:  $\bar{r}_{hole}^{exp.}$  calculation based on red portion of boundary.

Figure 11. Digitized Boundary of a Slice From the Perforated Plate and Calculation of the Throat Radius and  $\bar{r}_{hole}^{exp.}$  From Rd. 10771.

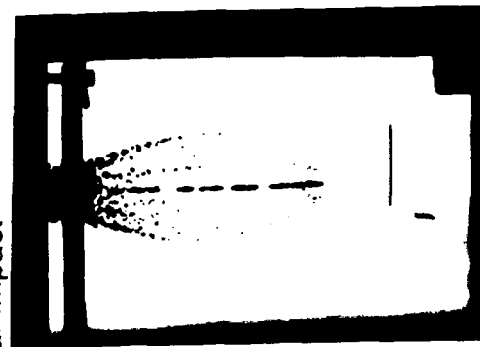
Rds. 4190 & 4189. Times Relative to Time of Initial Impact



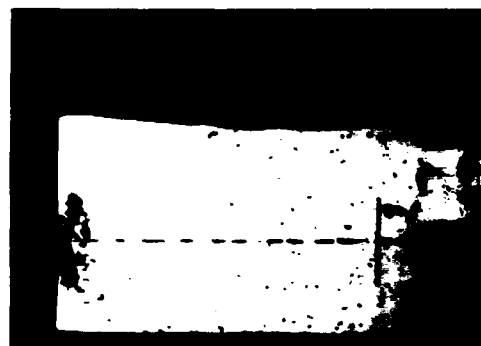
$t = 1.7 \mu s$



$t = 18.2 \mu s$



$t = 33.2 \mu s$



$t = 73.9 \mu s$



$t = 143.2 \mu s$



$t = 213.0 \mu s$

Figure 12. Flash Radiographs at Various Times From Rds. 4190 and 4189.

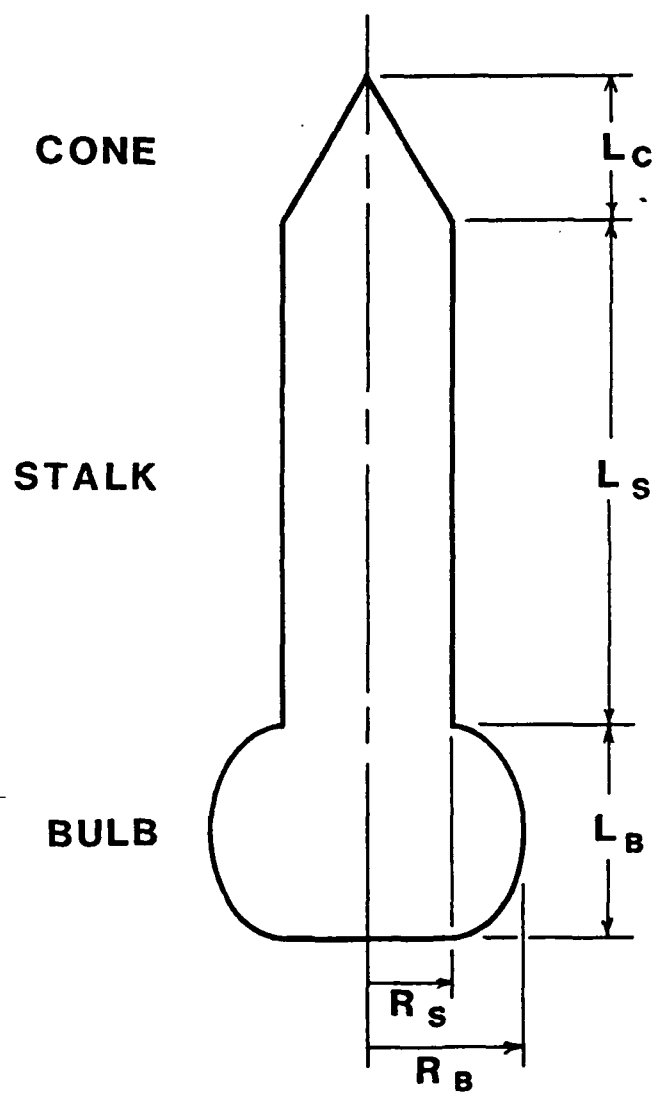


Figure 13. Five-Parameter Geometric Model for the Leading Jet Particle.

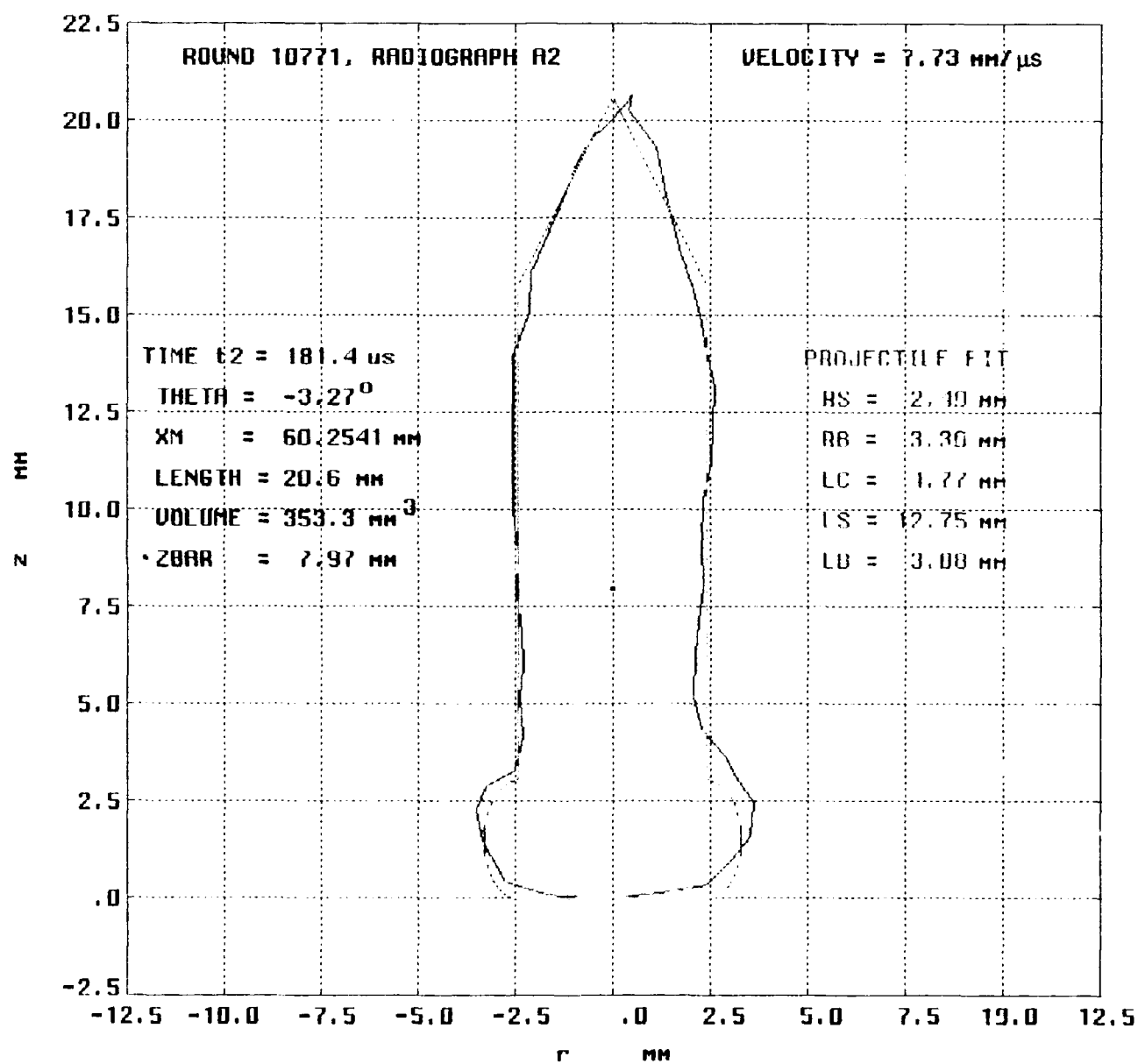


Figure 14. The Jet Particle Model Fitted to the Radiograph at 8.6 μs Before Impact.

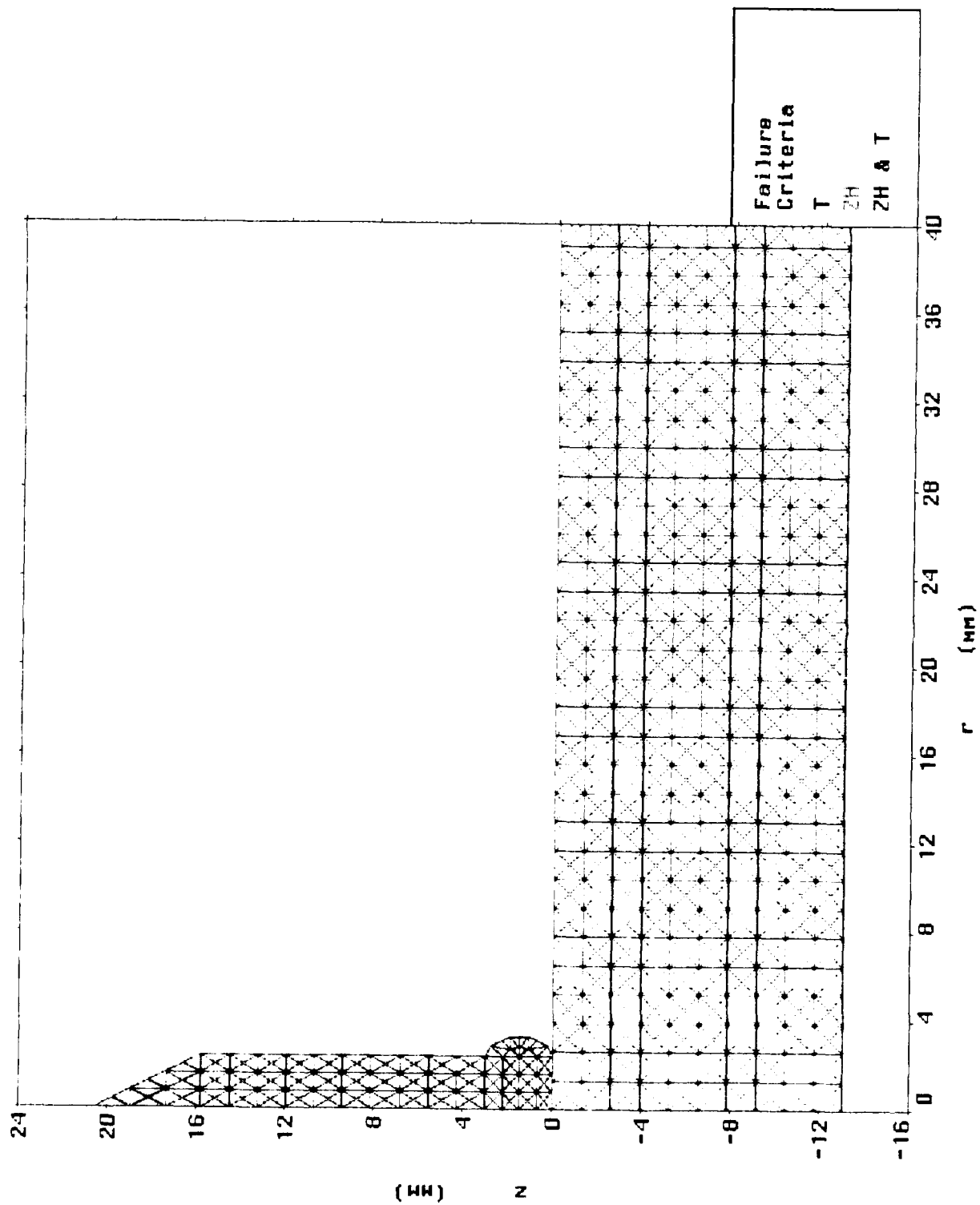


Figure 15. The Initial Mesh Used in Sections 5, 7, and 8.

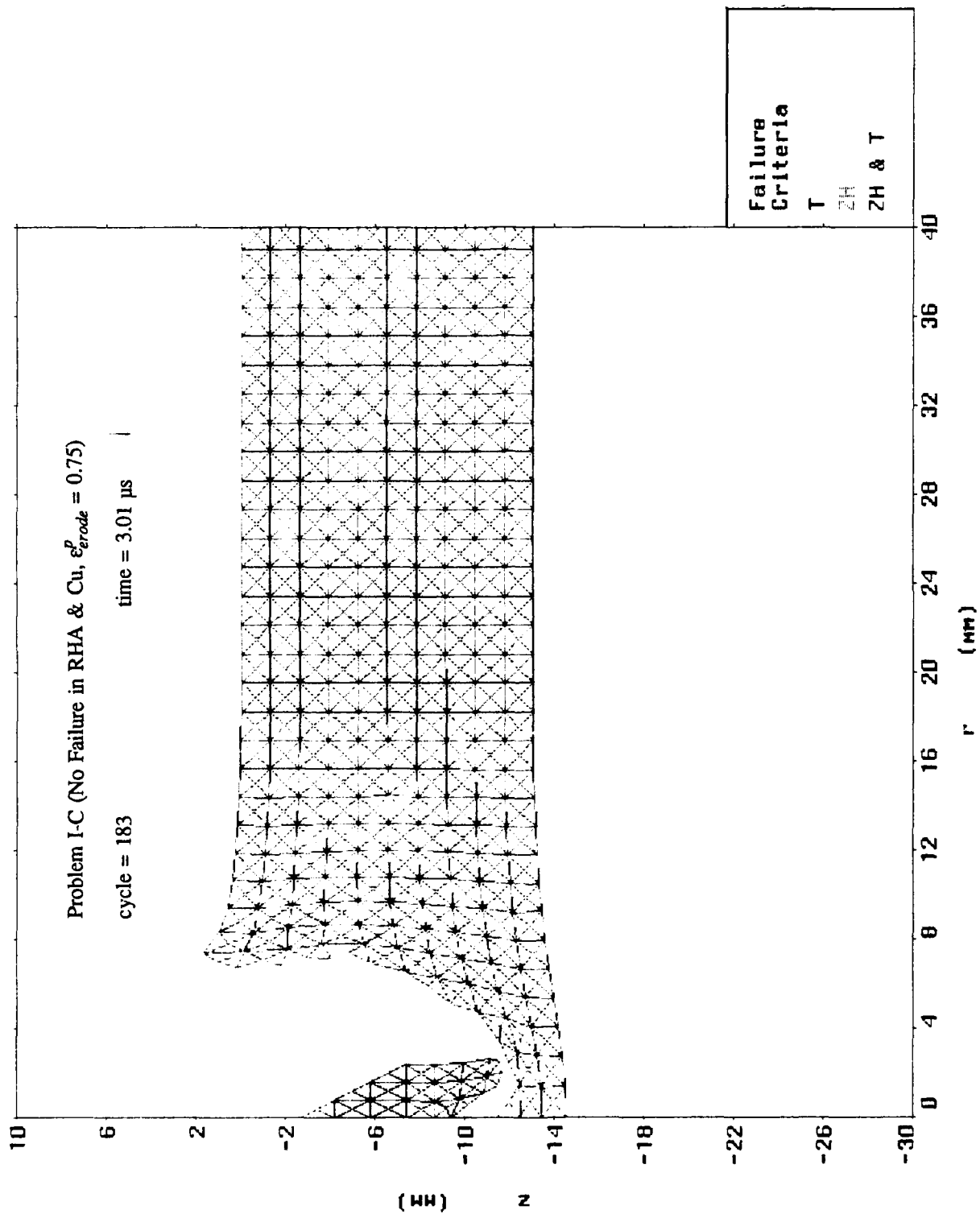


Figure 16. Mesh Plot at 3.01  $\mu$ s After Impact for Problem I-C.

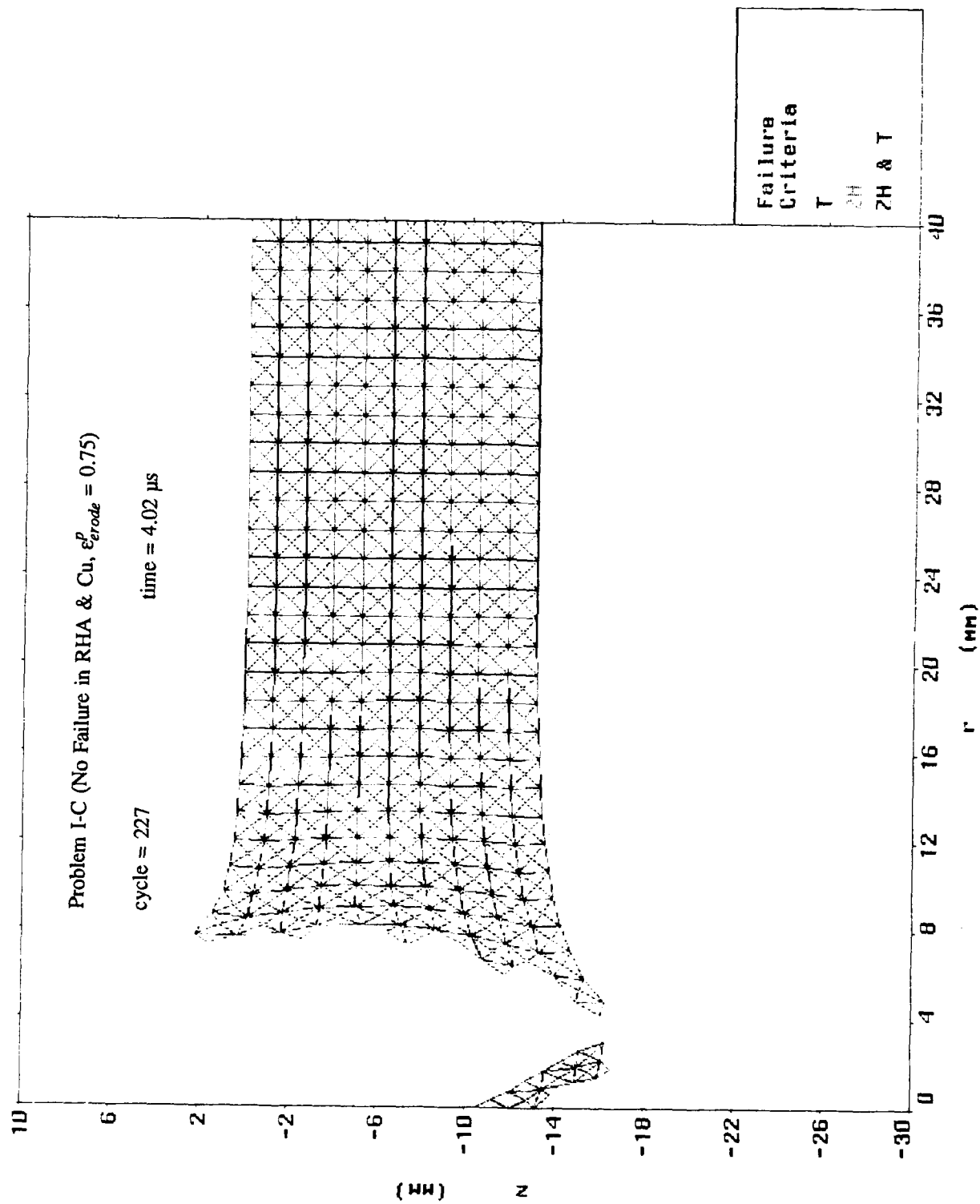


Figure 17. Mesh Plot at 4.02  $\mu\text{s}$  After Impact for Problem I-C.

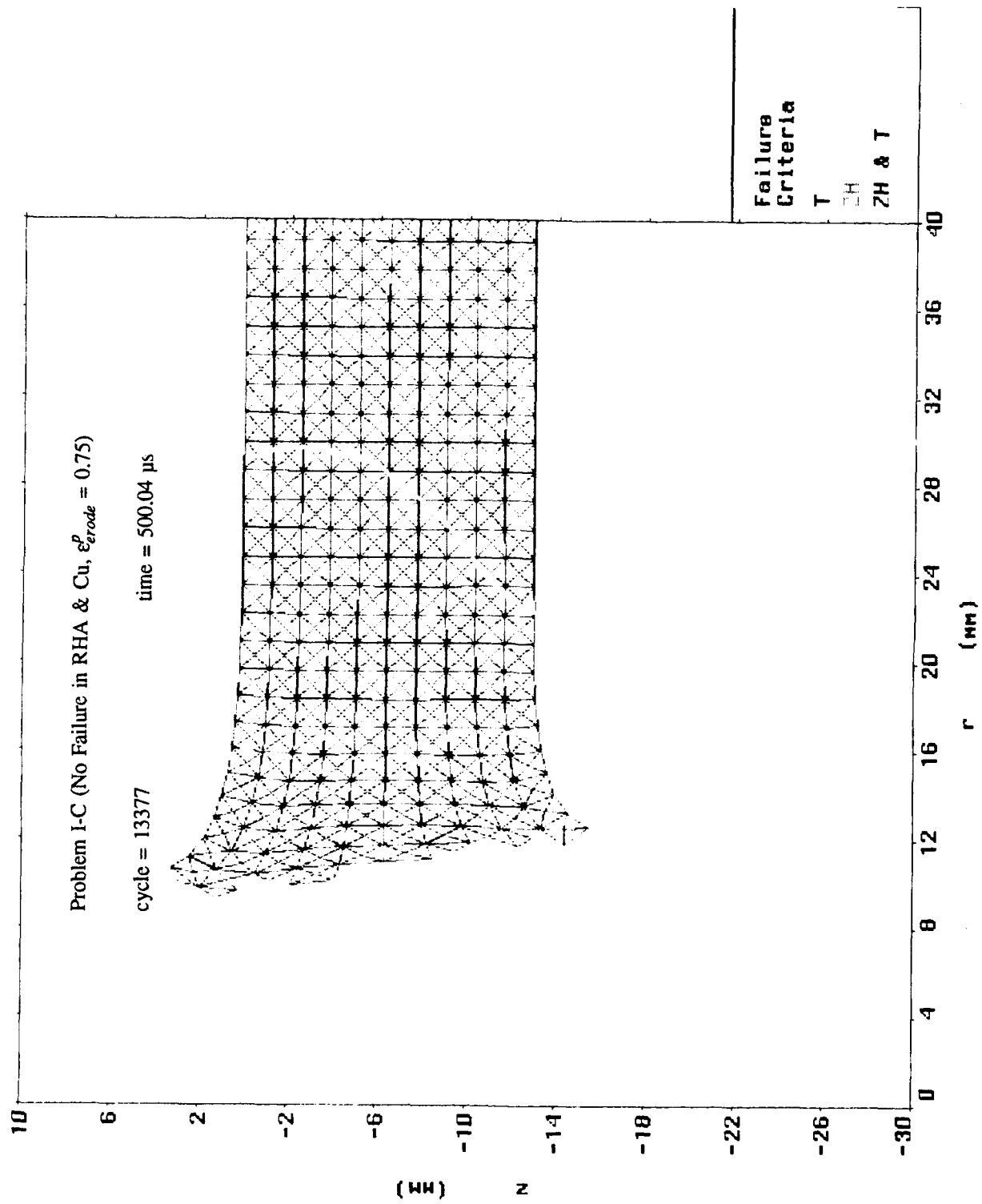


Figure 18. Mesh Plot at 500.04  $\mu$ s After Impact for Problem I-C.

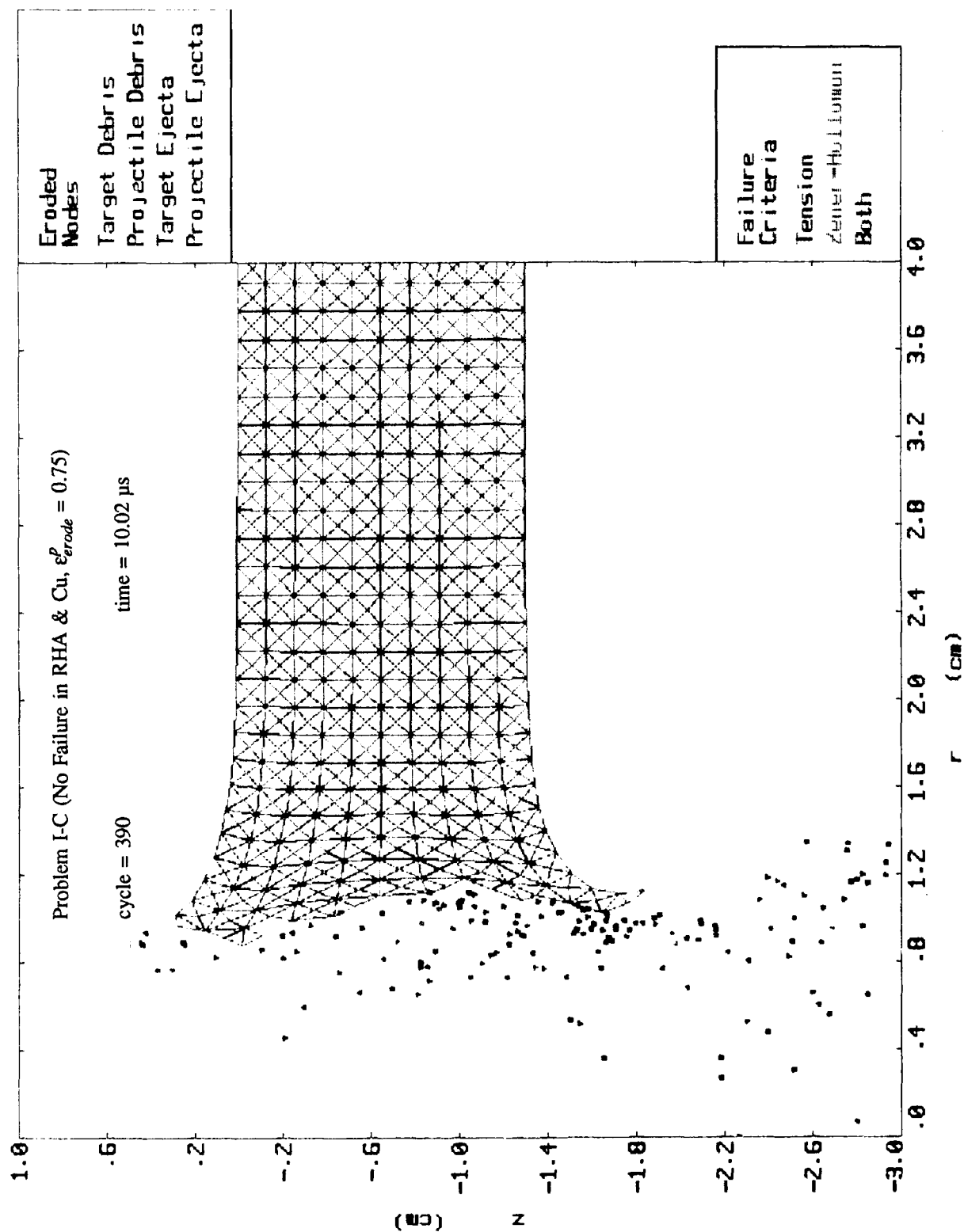
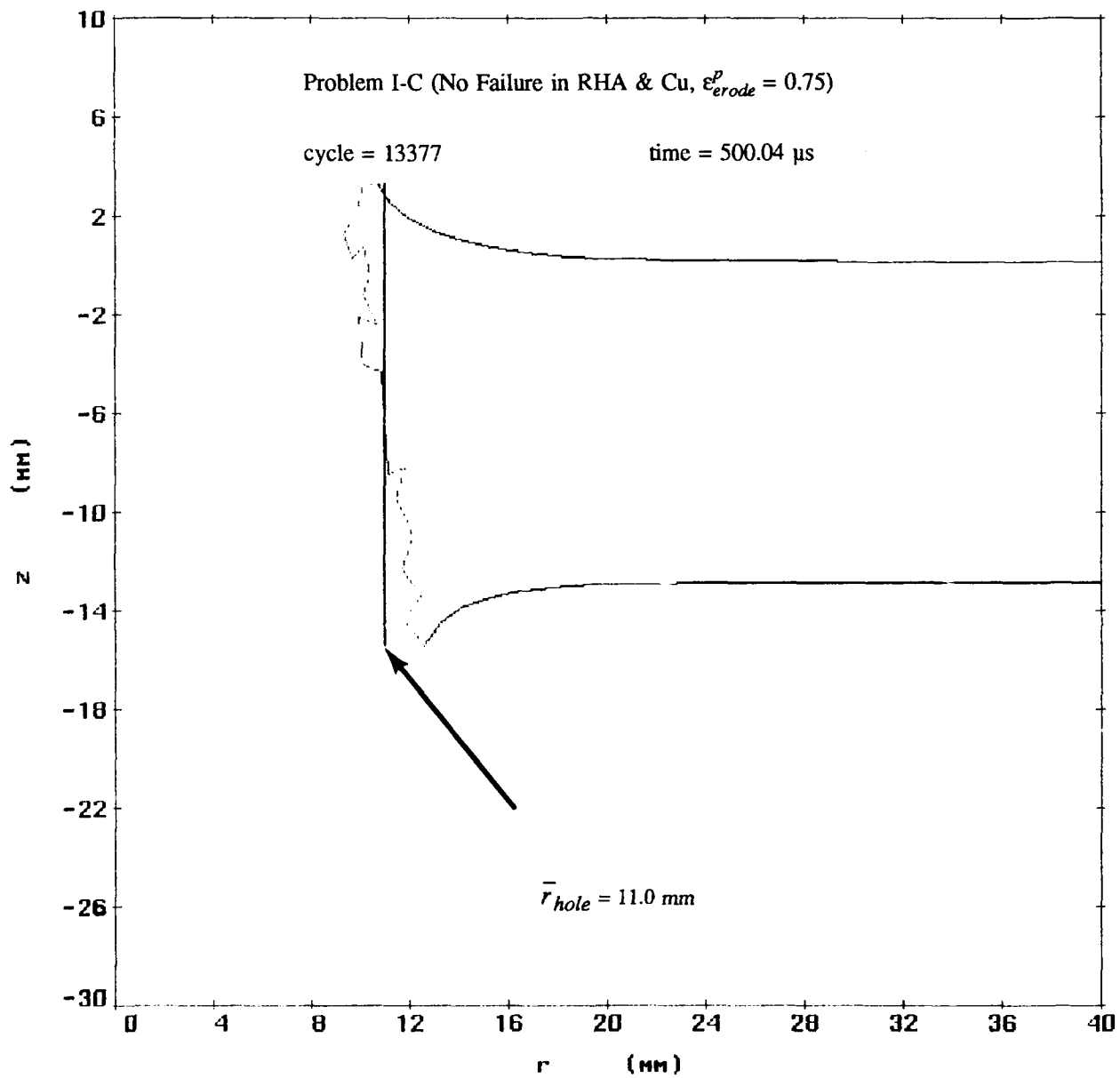


Figure 19. Mesh Plot at 10.02  $\mu$ s After Impact for Problem I-C, With Disembodied Nodes of Ejecta and Debris Included.



NOTE:  $\bar{r}_{hole}$  calculation based on red portion of boundary.

Figure 20. Mesh Boundary at 500.04  $\mu$ s and Calculation of  $\bar{r}_{hole}$  From Problem I-C.

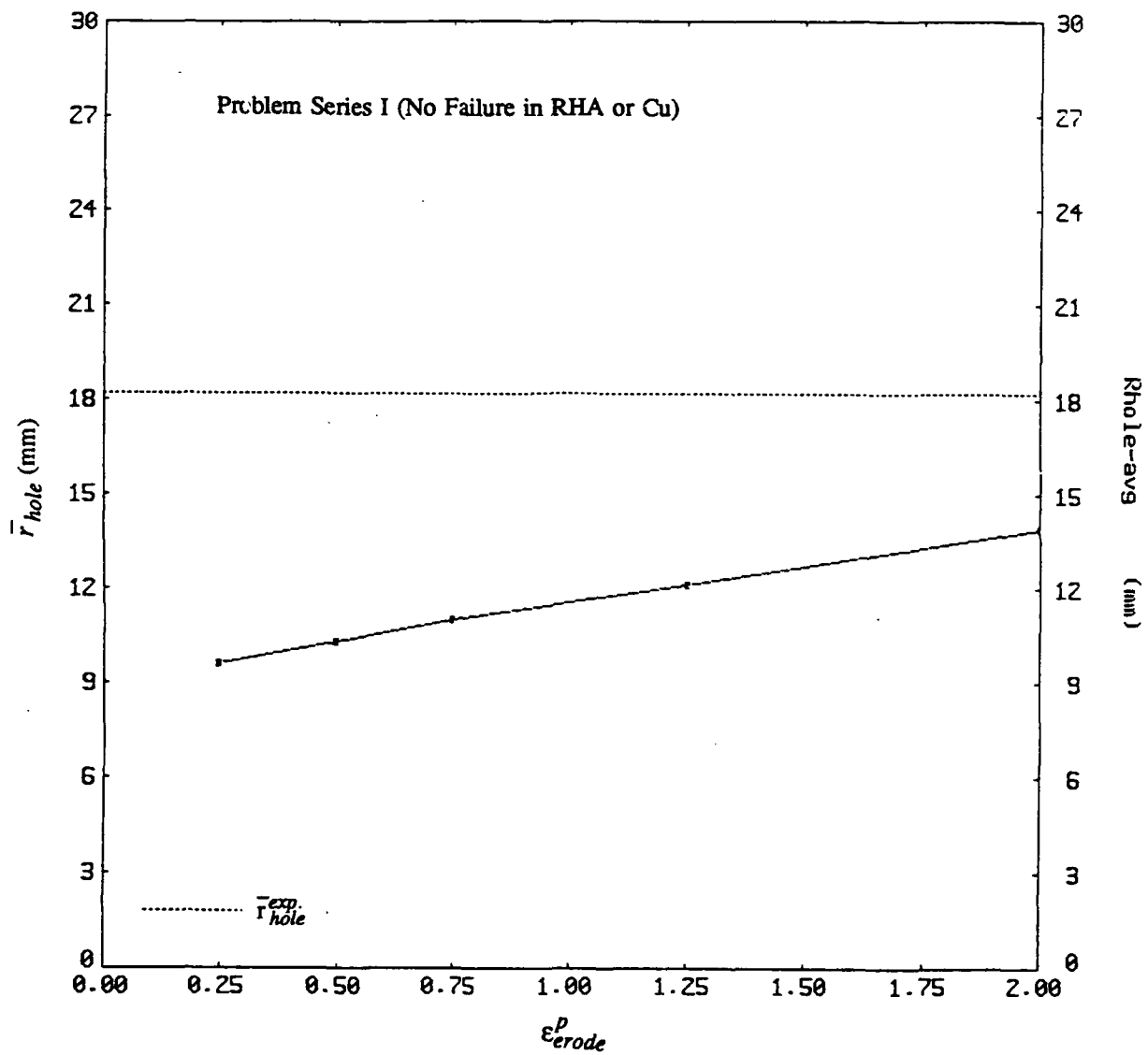


Figure 21. Computed  $\bar{r}_{hole}$  vs.  $\epsilon_{erode}^p$  for Problem Series I.

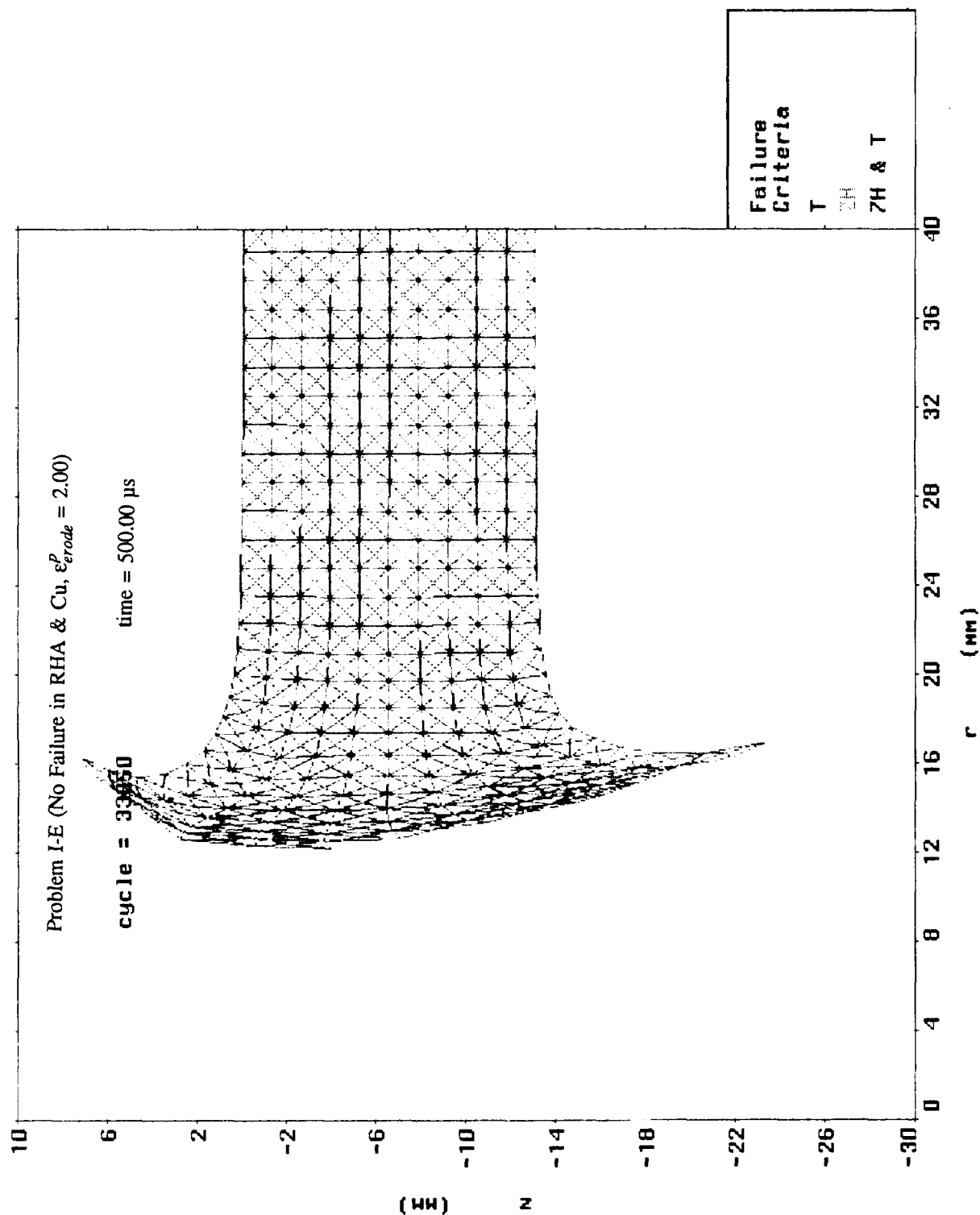


Figure 22. Mesh Plot at 500.00  $\mu$ s After Impact for Problem I-E.

Problem Series I (No failure in RHA or Cu)

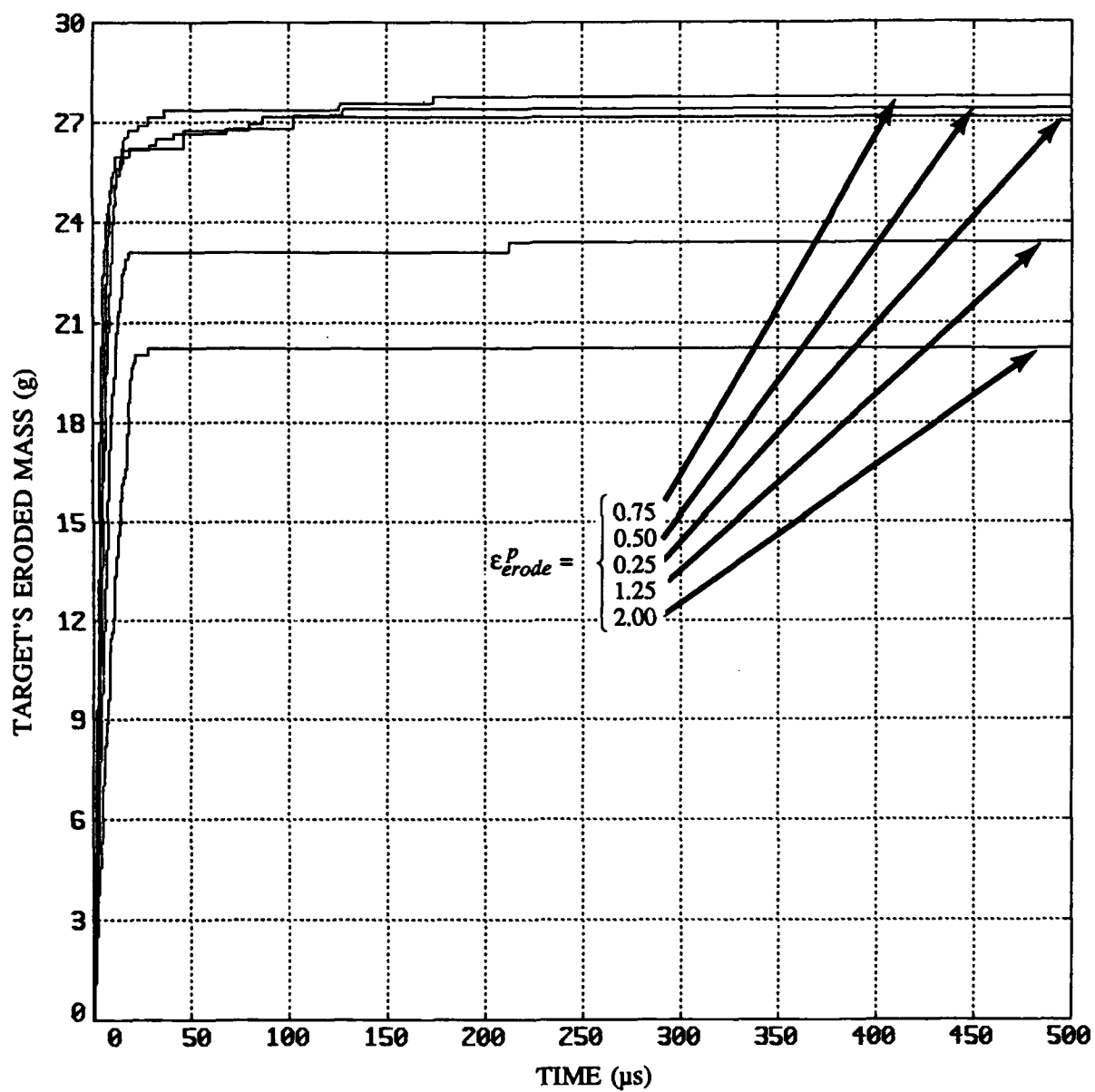


Figure 23. Mass Lost From Target Plate vs. Time for Problem Series I.



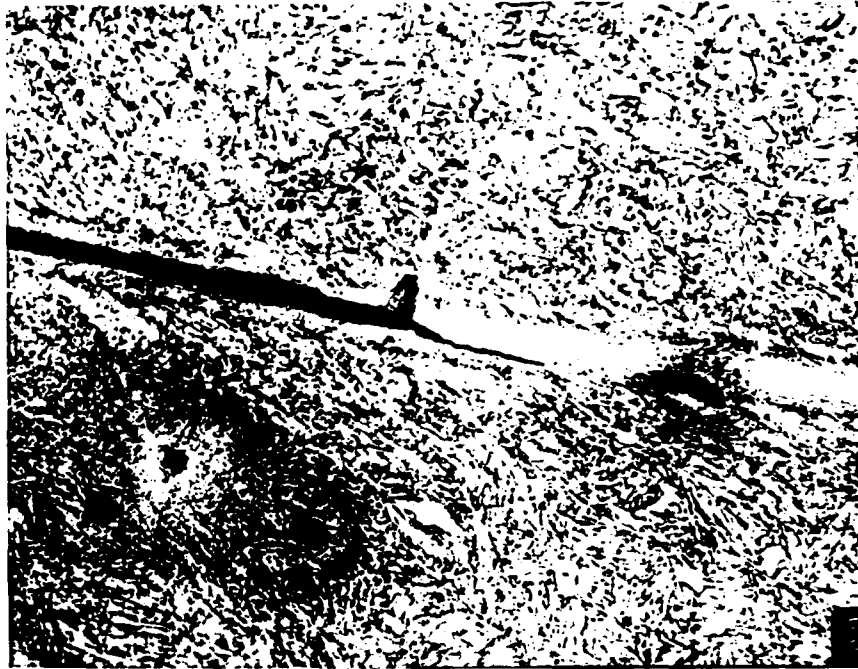
SEM; 4,000x; 2% Nital etch.

Figure 24. Micrograph of a Fracture Surface Formed by Void Coalescence in the RHA Target Plate of Rd. 10771.



SEM; 3,700x; 2% Nital etch.

Figure 25. Micrograph of a Shear Band in the RHA Target Plate of Rd. 10771.



Optical Micrograph, 800x, 2% Nital etch.

Figure 26. Micrograph of a Crack That Extends Along a Shear Band in the RHA Plate of Rd. 10771.

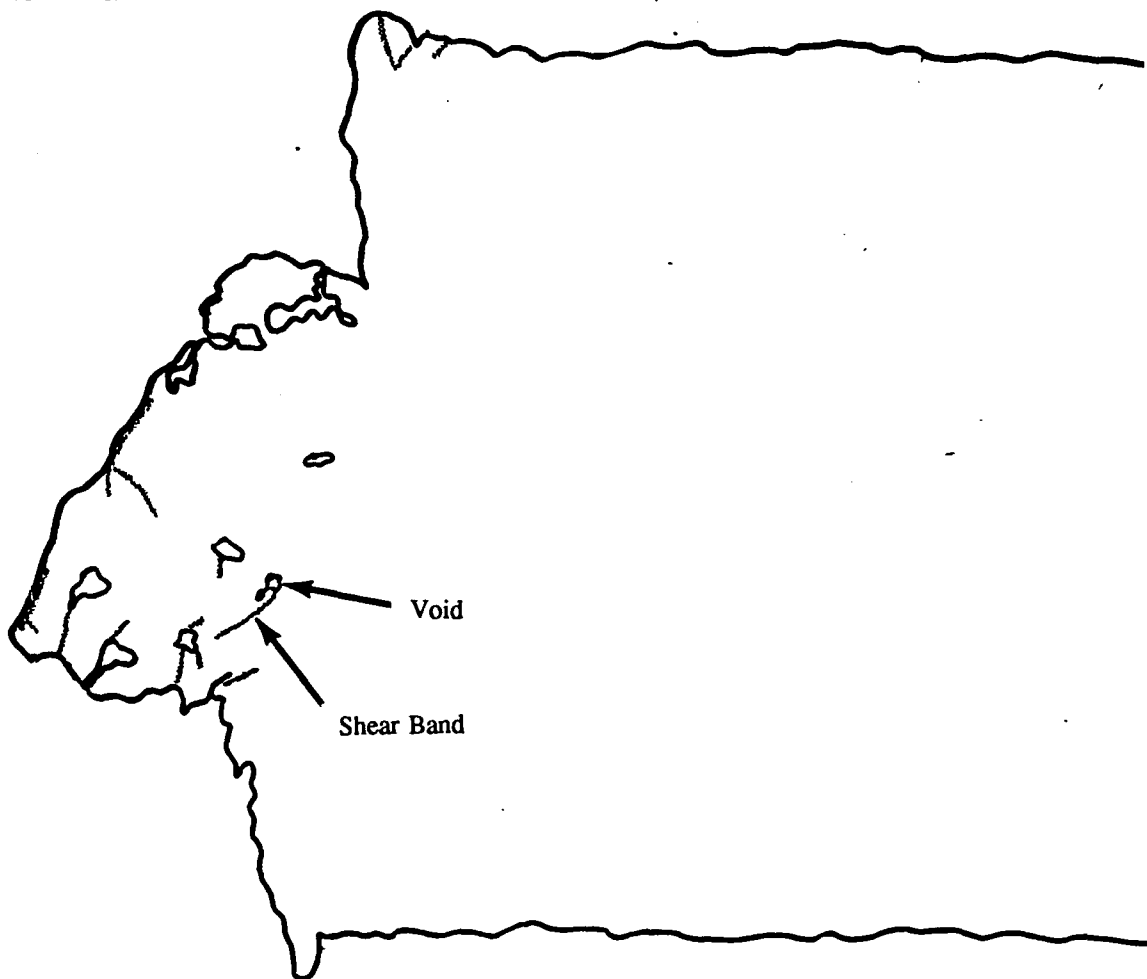


Figure 27. Sketch Showing Locations of Prominent Voids and Shear Bands in a Radial Slice From the RHA Plate of Rd. 10771.

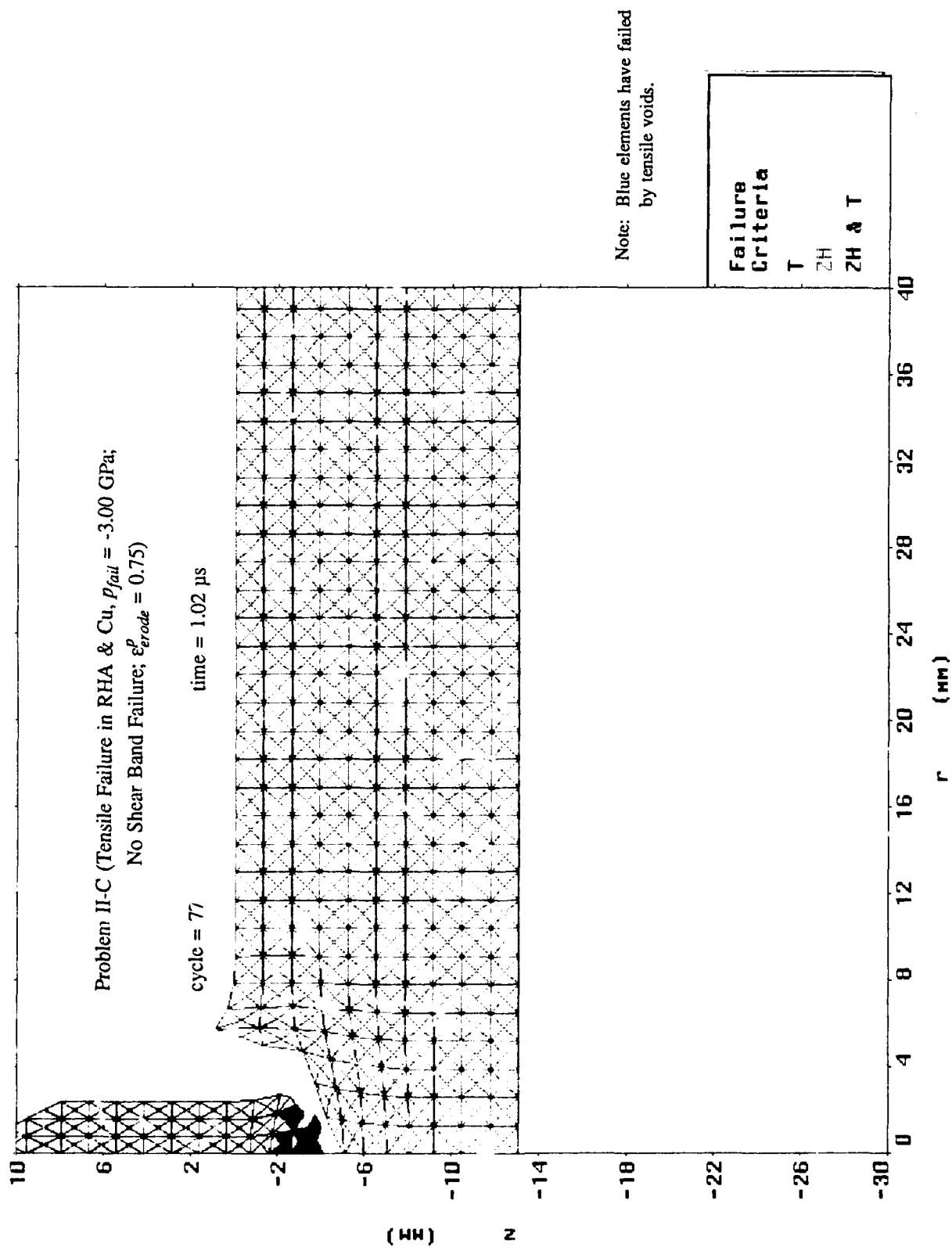


Figure 28. Mesh Plot at 1.02  $\mu$ s After Impact for Problem II-C.

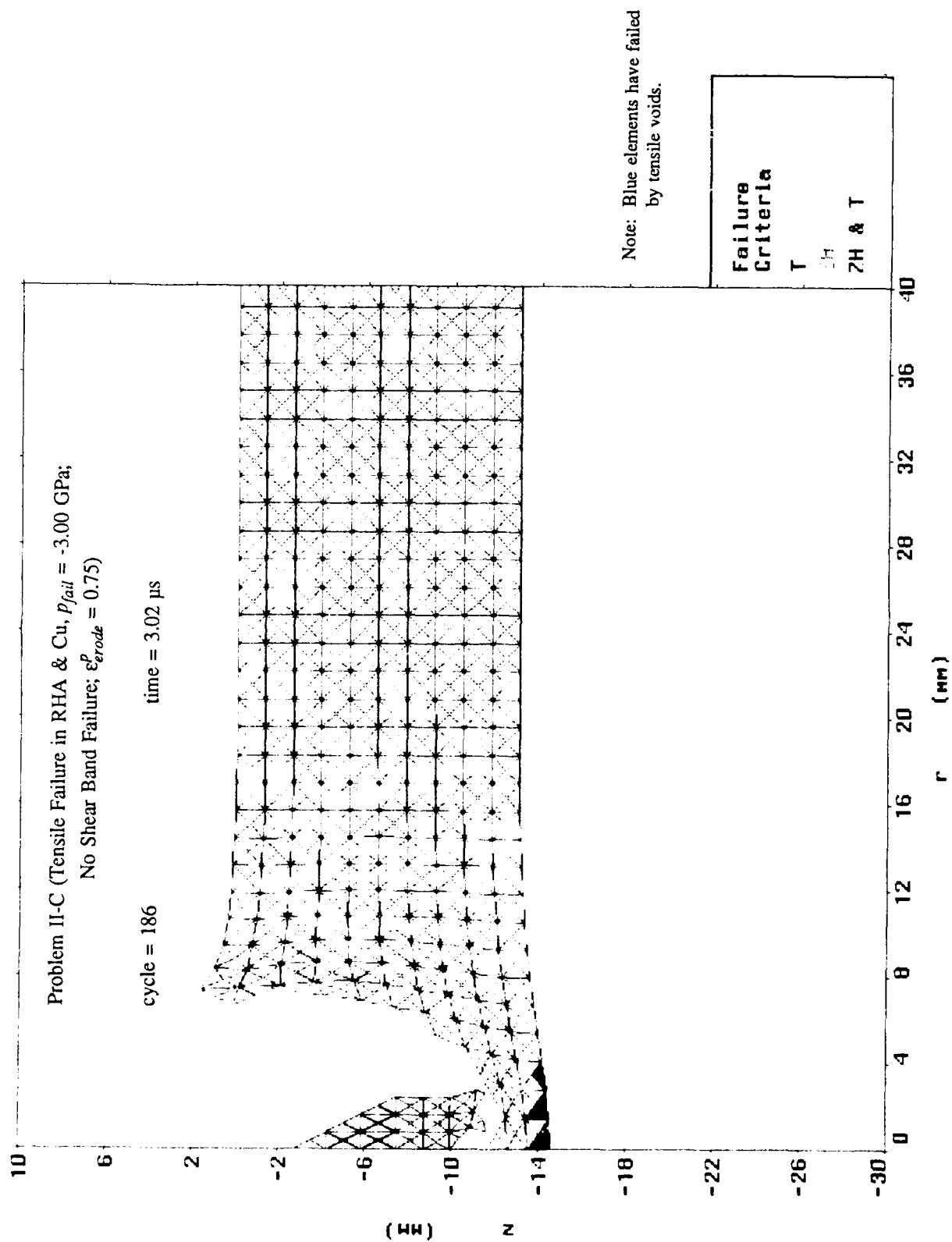


Figure 29. Mesh Plot at 3.02  $\mu$ s After Impact for Problem II-C.

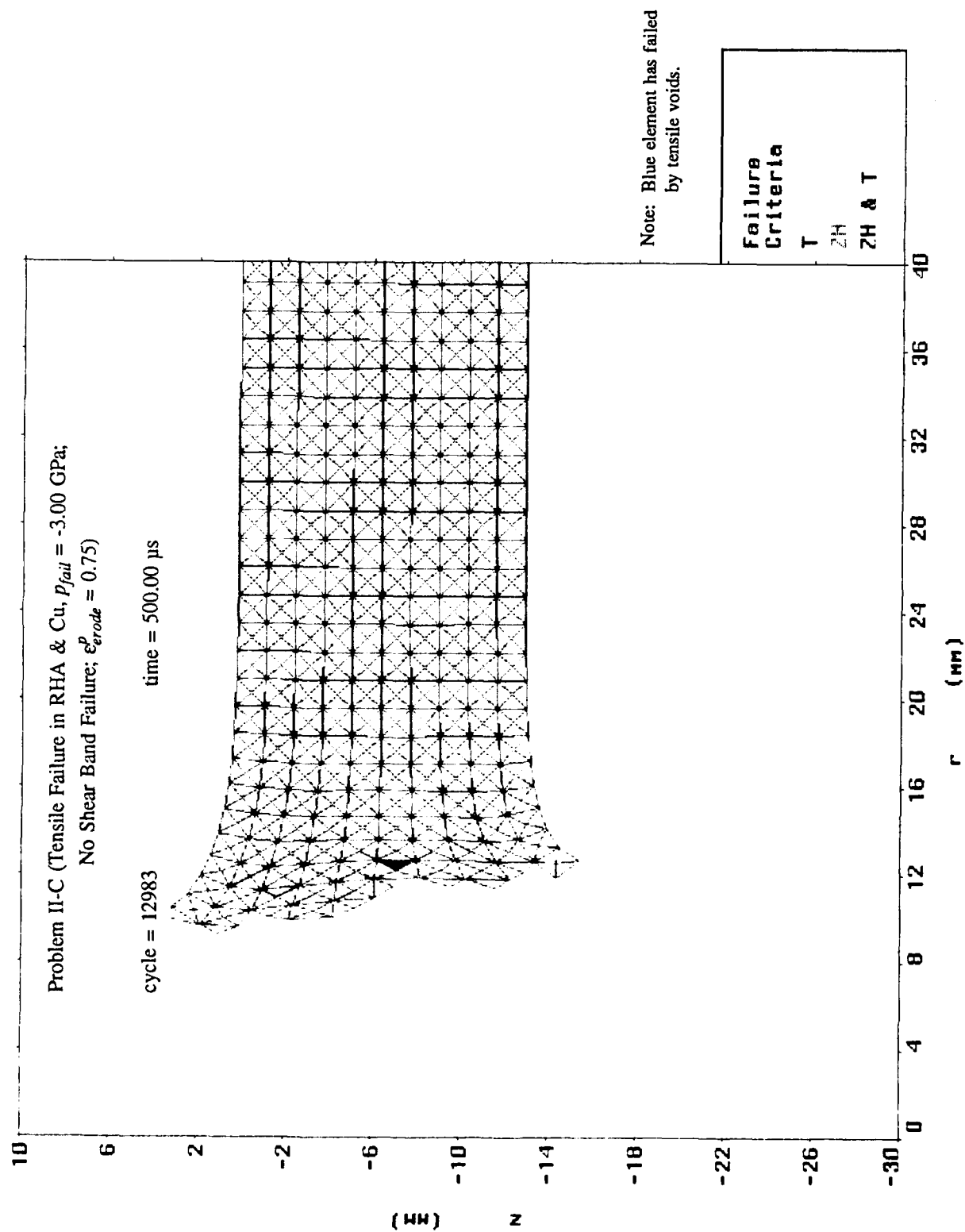


Figure 30. Mesh Plot at 500.00  $\mu$ s After Impact for Problem II-C.

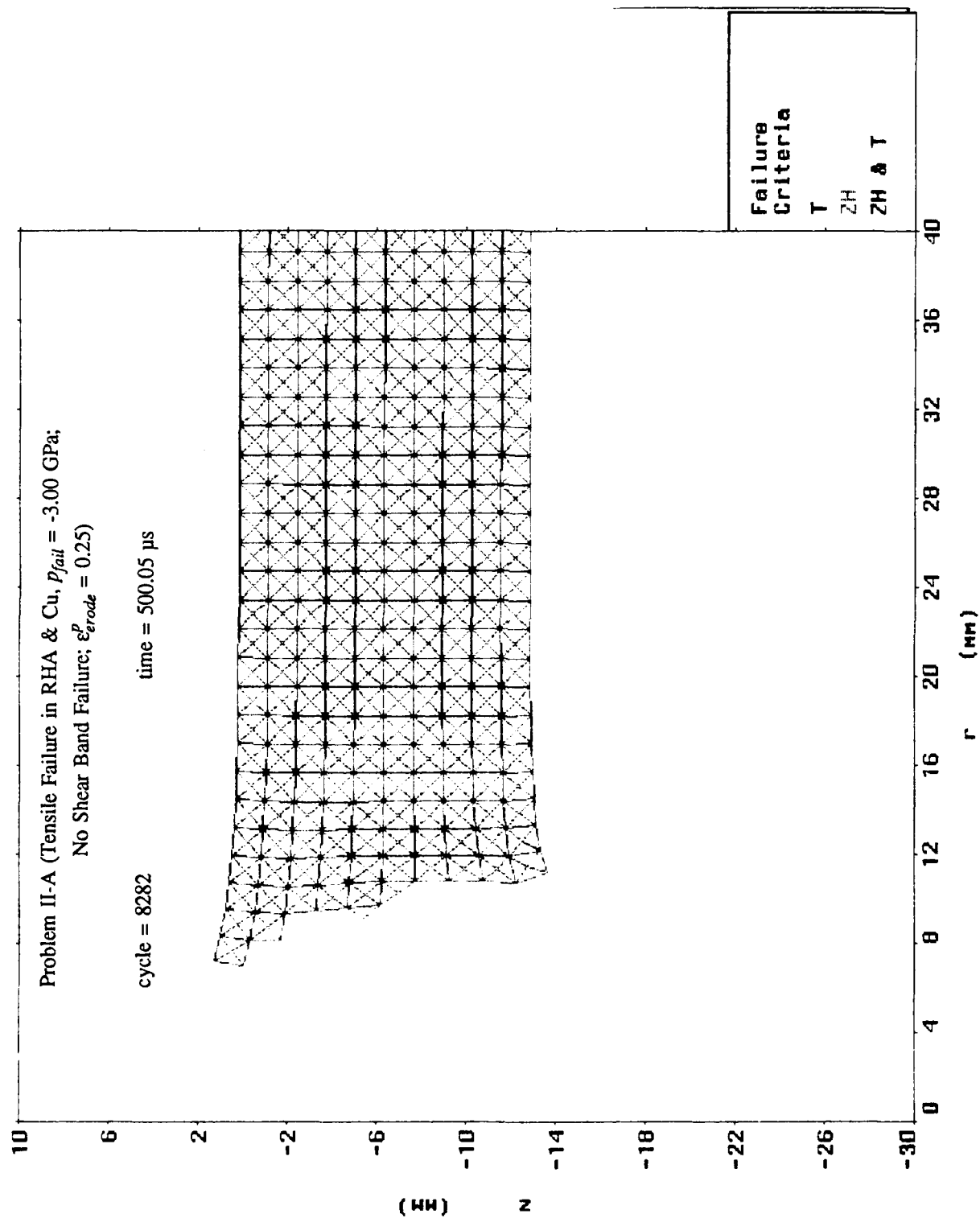


Figure 31. Mesh Plot at 500.05  $\mu$ s After Impact for Problem II-A.

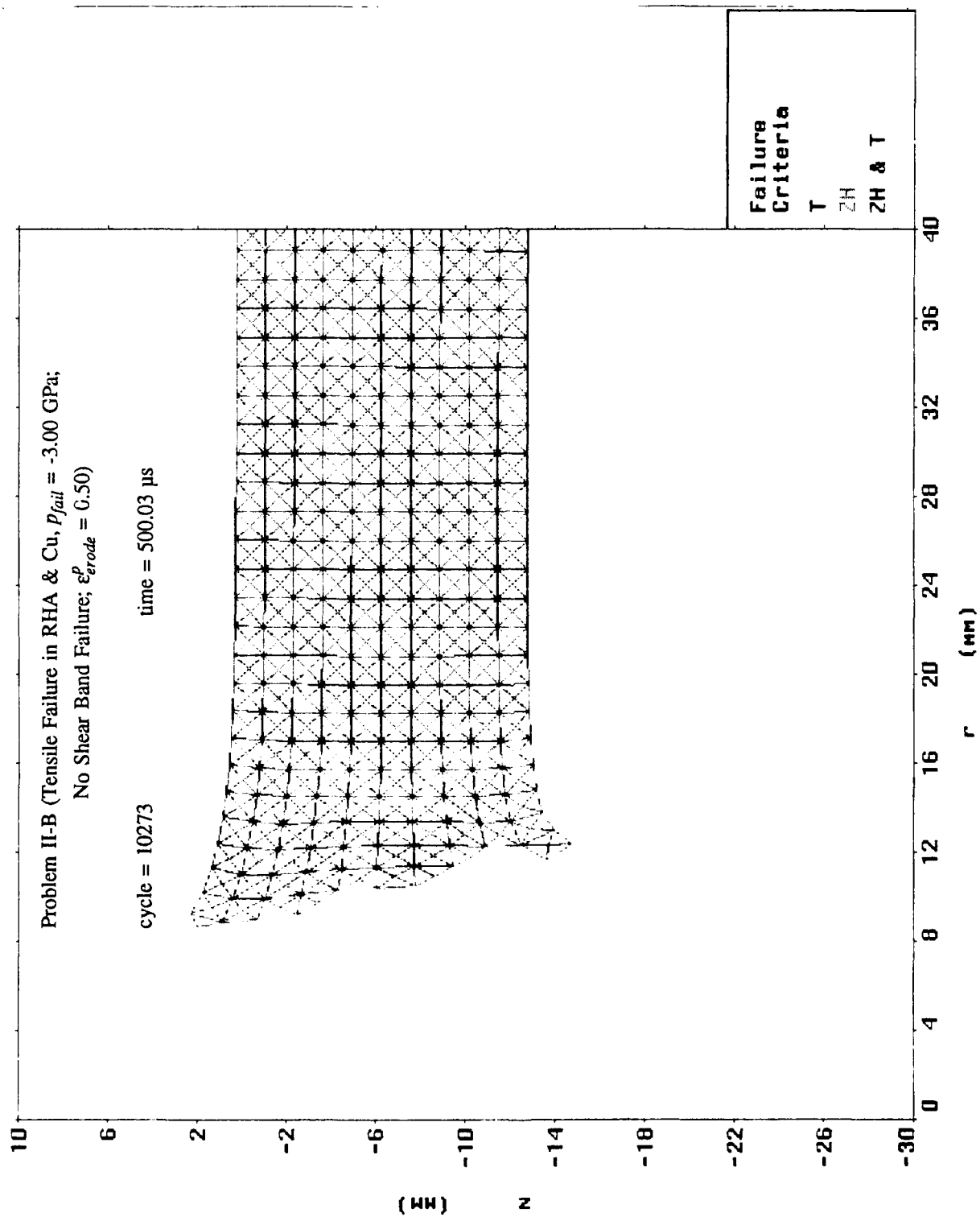


Figure 32. Mesh Plot at 500.03  $\mu$ s After Impact for Problem II-B.

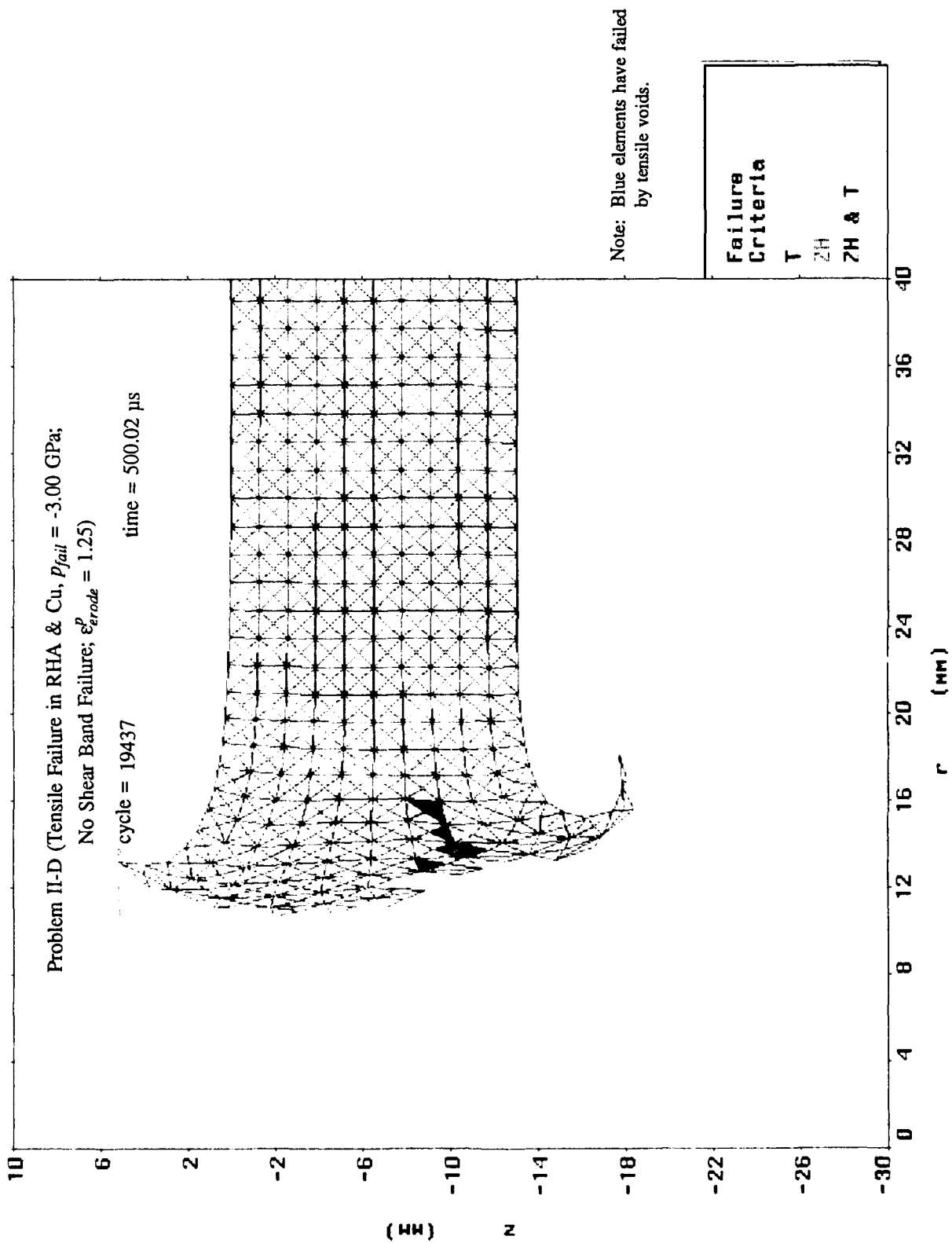


Figure 33. Mesh Plot at 500.02  $\mu$ s After Impact for Problem II-D.

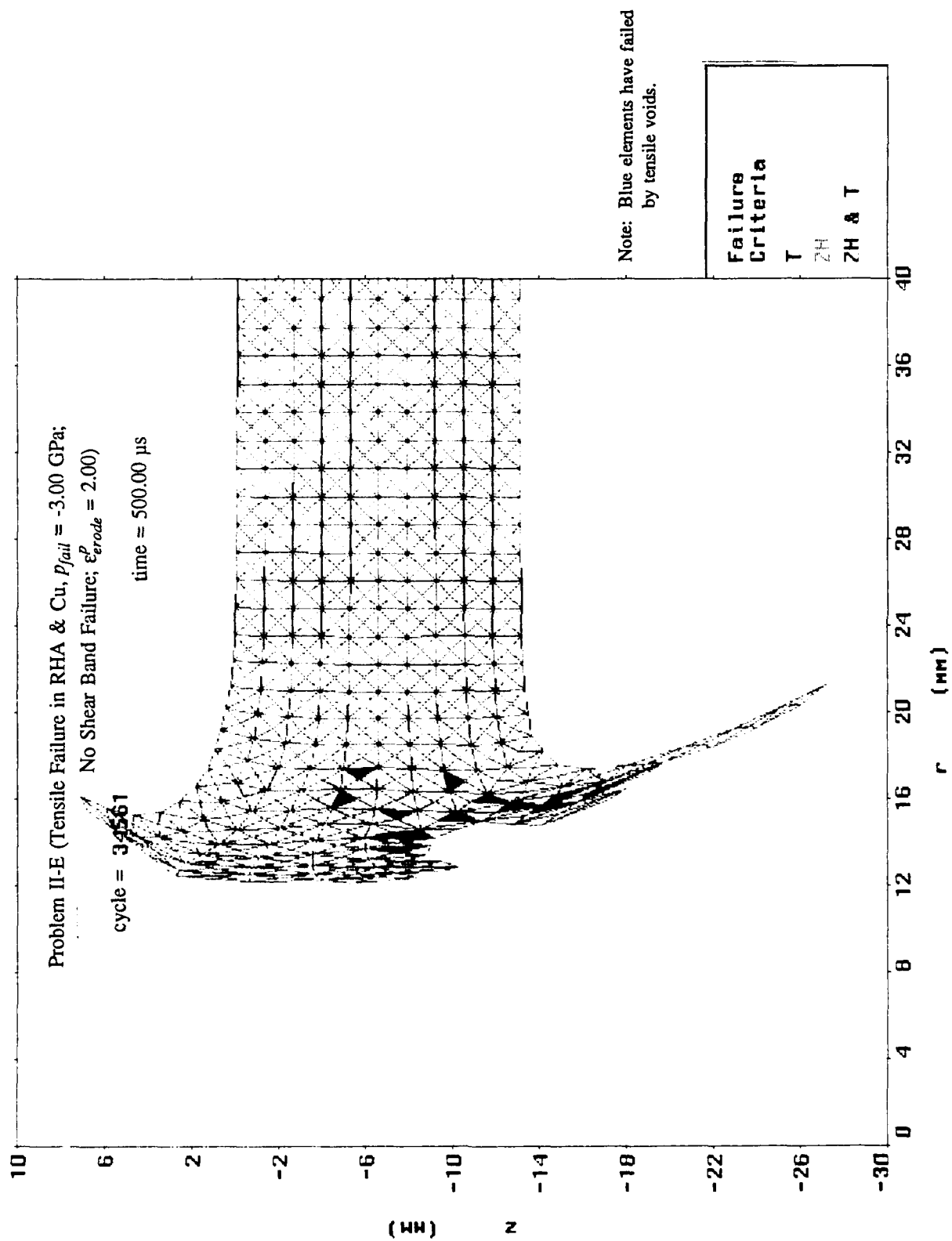


Figure 34. Mesh Plot at 500.00  $\mu$ s After Impact for Problem II-E.

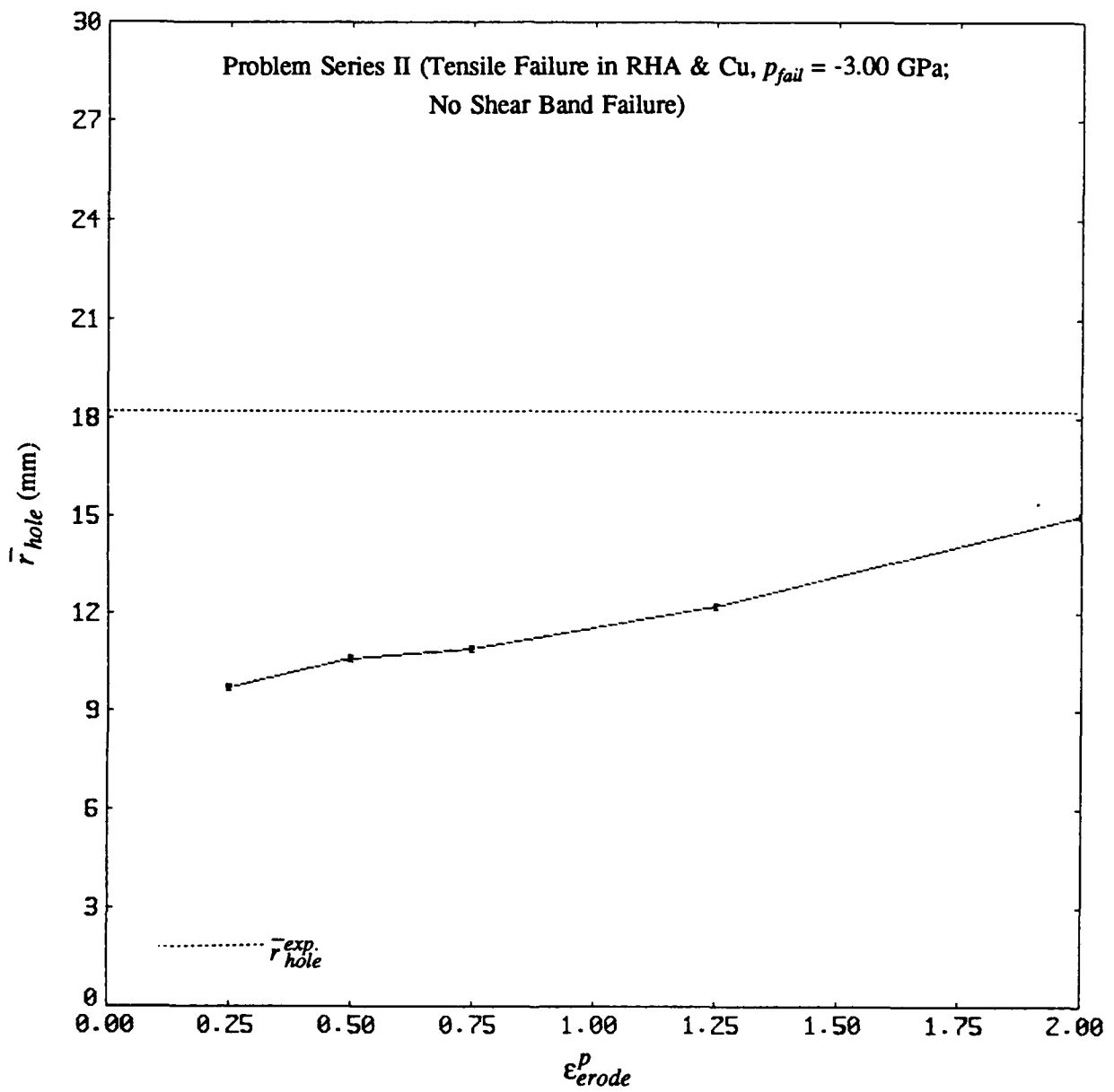


Figure 35. Computed  $\bar{r}_{hole}$  vs.  $\epsilon_{erode}^p$  for Problem Series II.

Problem Series II (Tensile Failure in RHA & Cu,  $p_{fail} = -3.00$  GPa;  
No Shear Band Failure)

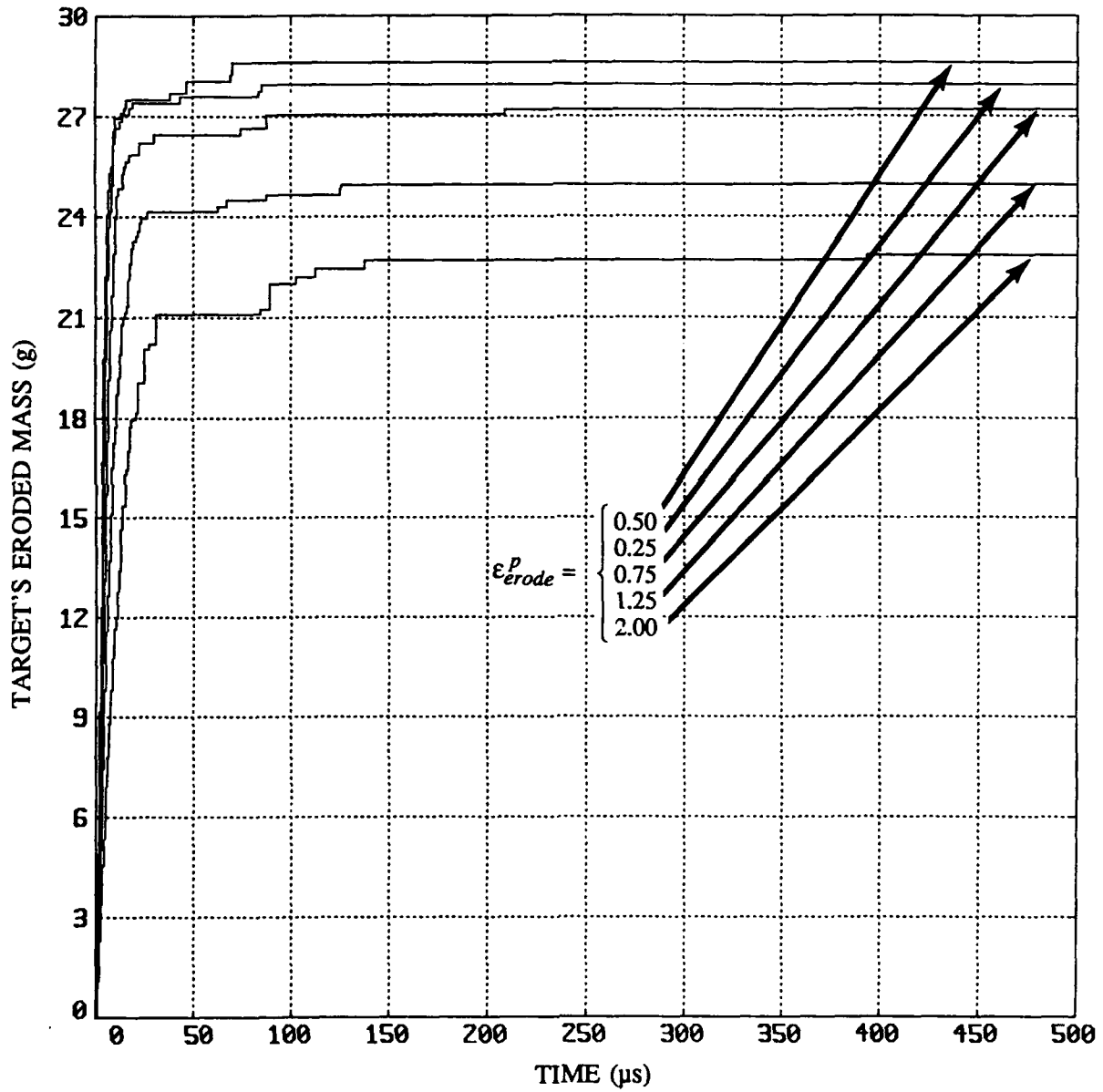
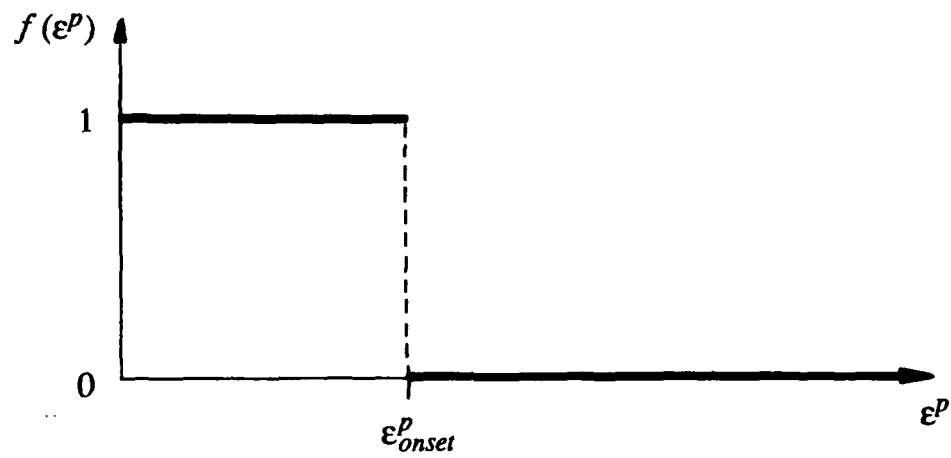
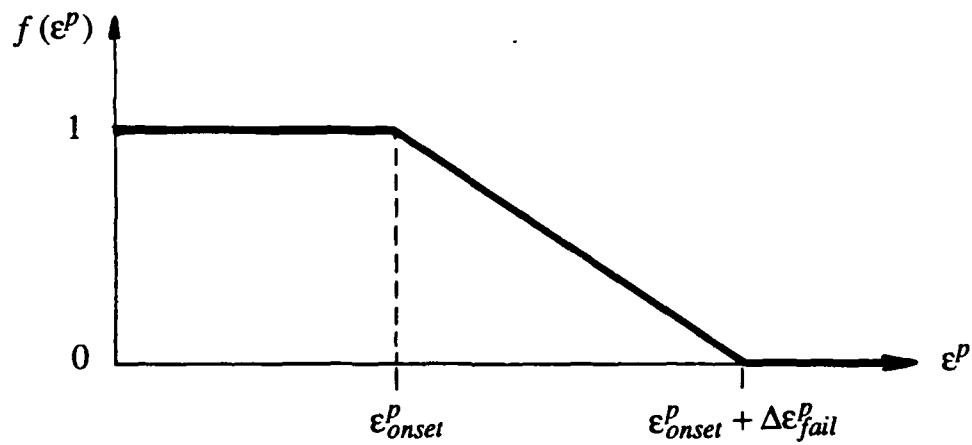


Figure 36. Mass Lost From Target Plate vs. Time for Problem Series II.



(a)  $\Delta\epsilon_{fail}^p = 0$



(b)  $\Delta\epsilon_{fail}^p > 0$

Figure 37. The Deviatoric-Stress Reduction Function Used With the Shear Band Failure Model.

Problem Series III Through VIII (Tensile Failure in RHA & Cu,  $p_{fail} = -3.00$  GPa;  
Shear Band Failure in RHA,  $\Delta\epsilon_{fail}^p$  Varied)

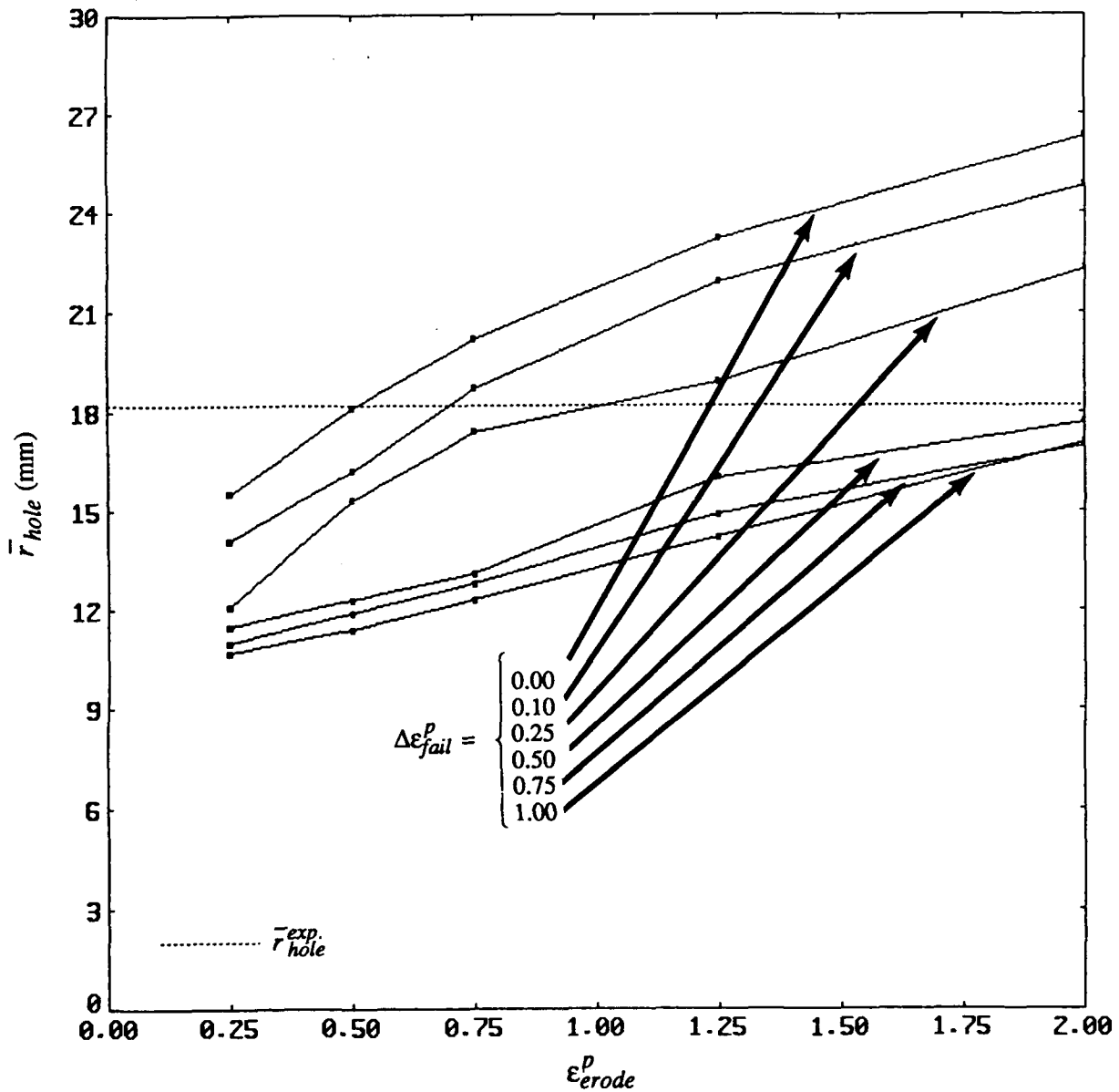


Figure 38. Computed  $\bar{r}_{hole}$  vs.  $\epsilon_{erode}^p$  With  $\Delta\epsilon_{fail}^p$  a Parameter  
for Problem Series III Through VIII.

Problem Series III Through VIII (Tensile Failure in RHA & Cu,  $p_{fail} = -3.00$  GPa;  
Shear Band Failure in RHA,  $\Delta\epsilon_{fail}^p$  Varied)

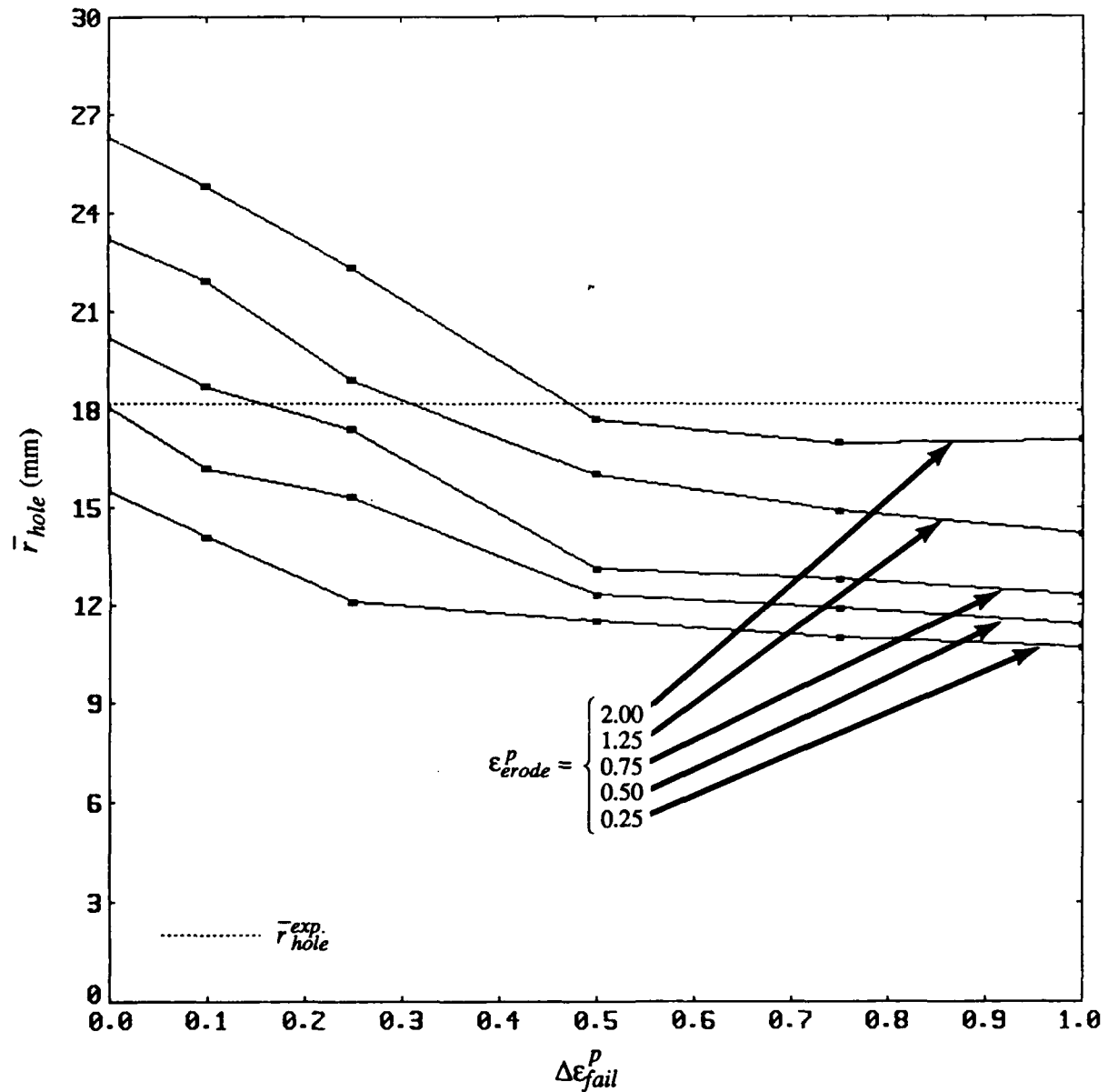


Figure 39. Computed  $\bar{r}_{hole}$  vs.  $\Delta\epsilon_{fail}^p$  With  $\epsilon_{erode}^p$  a Parameter for  
Problem Series III Through VIII.

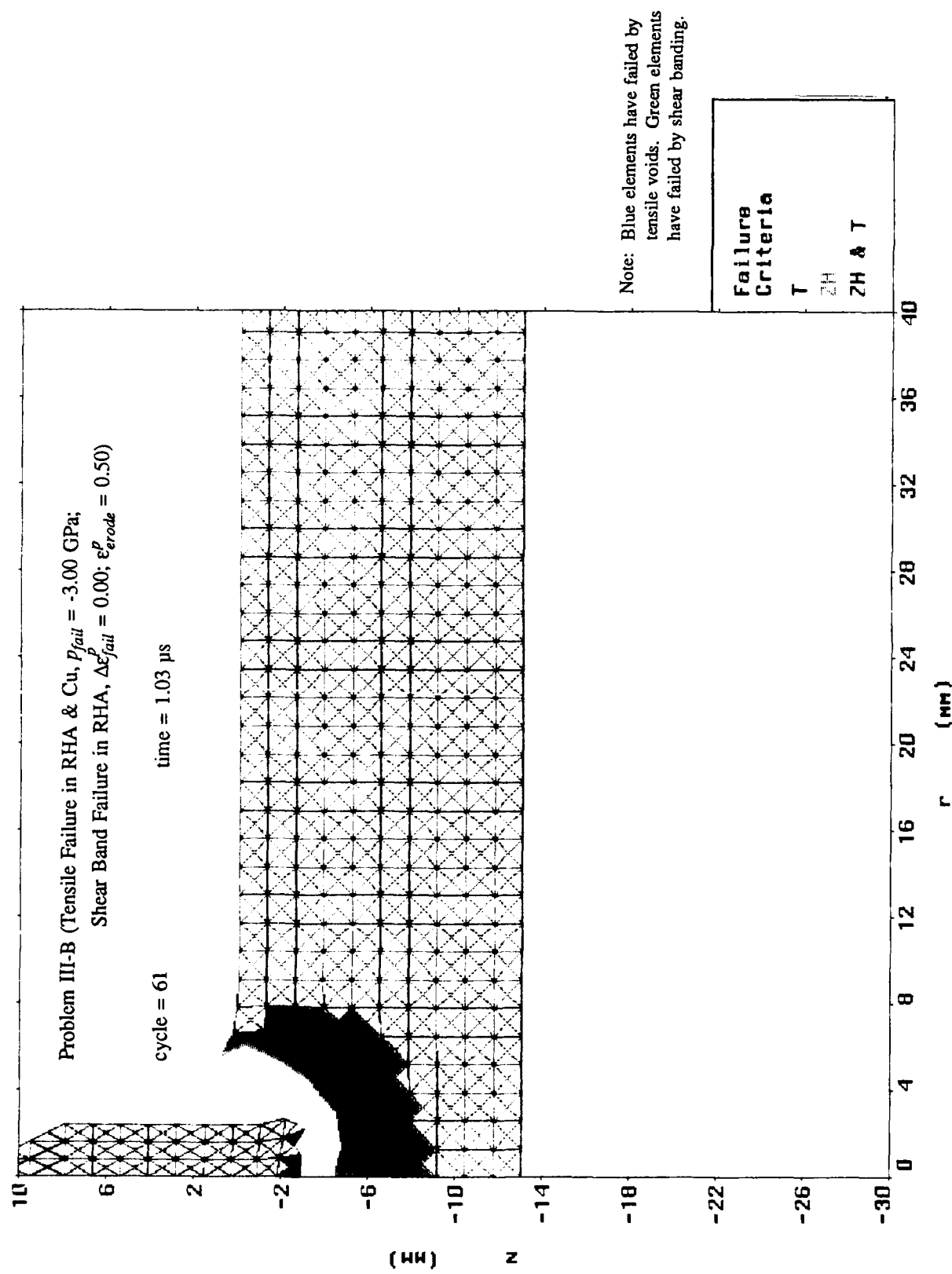


Figure 40. Mesh Plot at 1.03  $\mu$ s After Impact for Problem III-B.

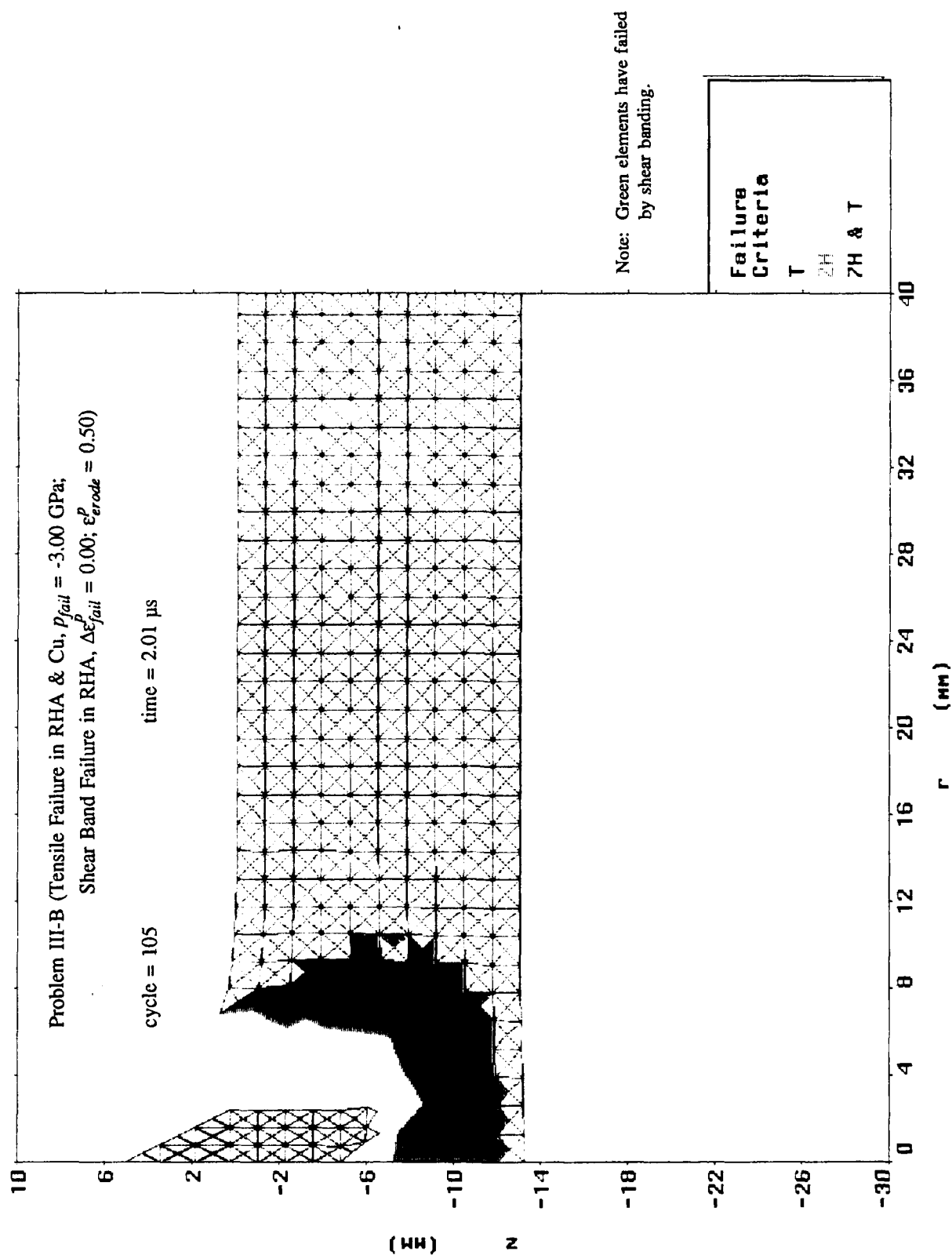


Figure 41. Mesh Plot at 2.01  $\mu$ s After Impact for Problem III-B.

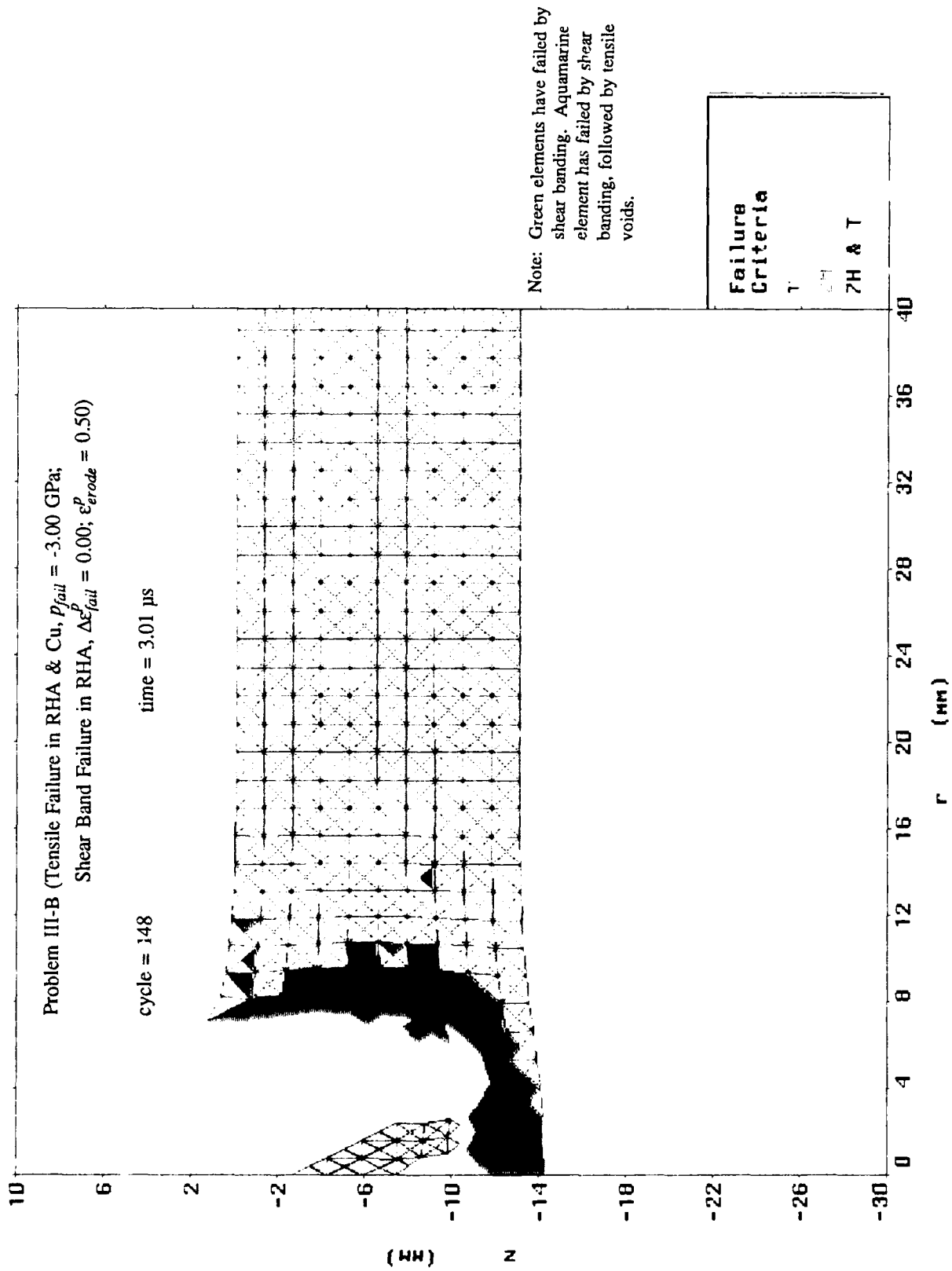


Figure 42. Mesh Plot at 3.01  $\mu$ s After Impact for Problem III-B.

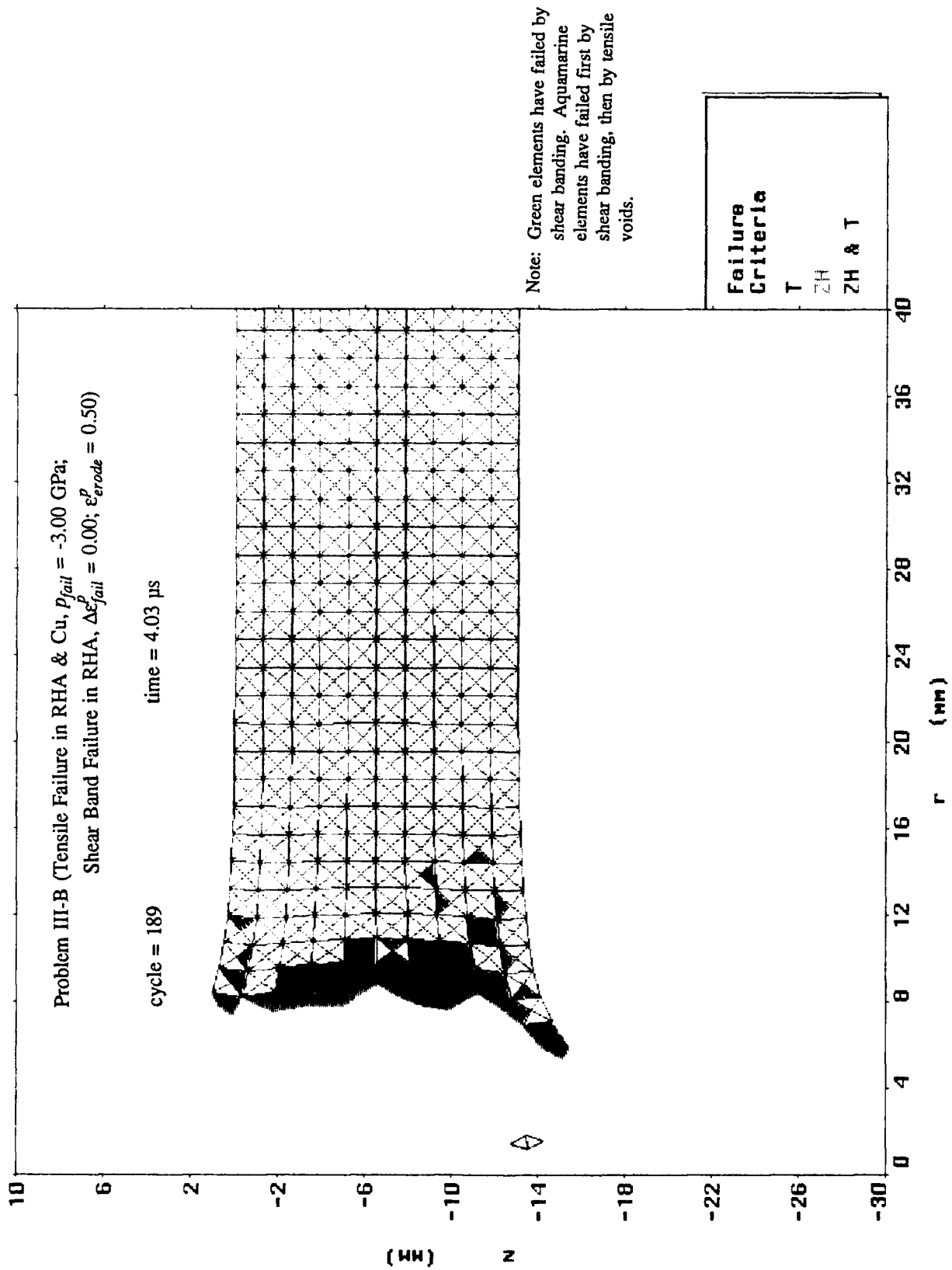


Figure 43. Mesh Plot at 4.03  $\mu$ s After Impact for Problem III-B.

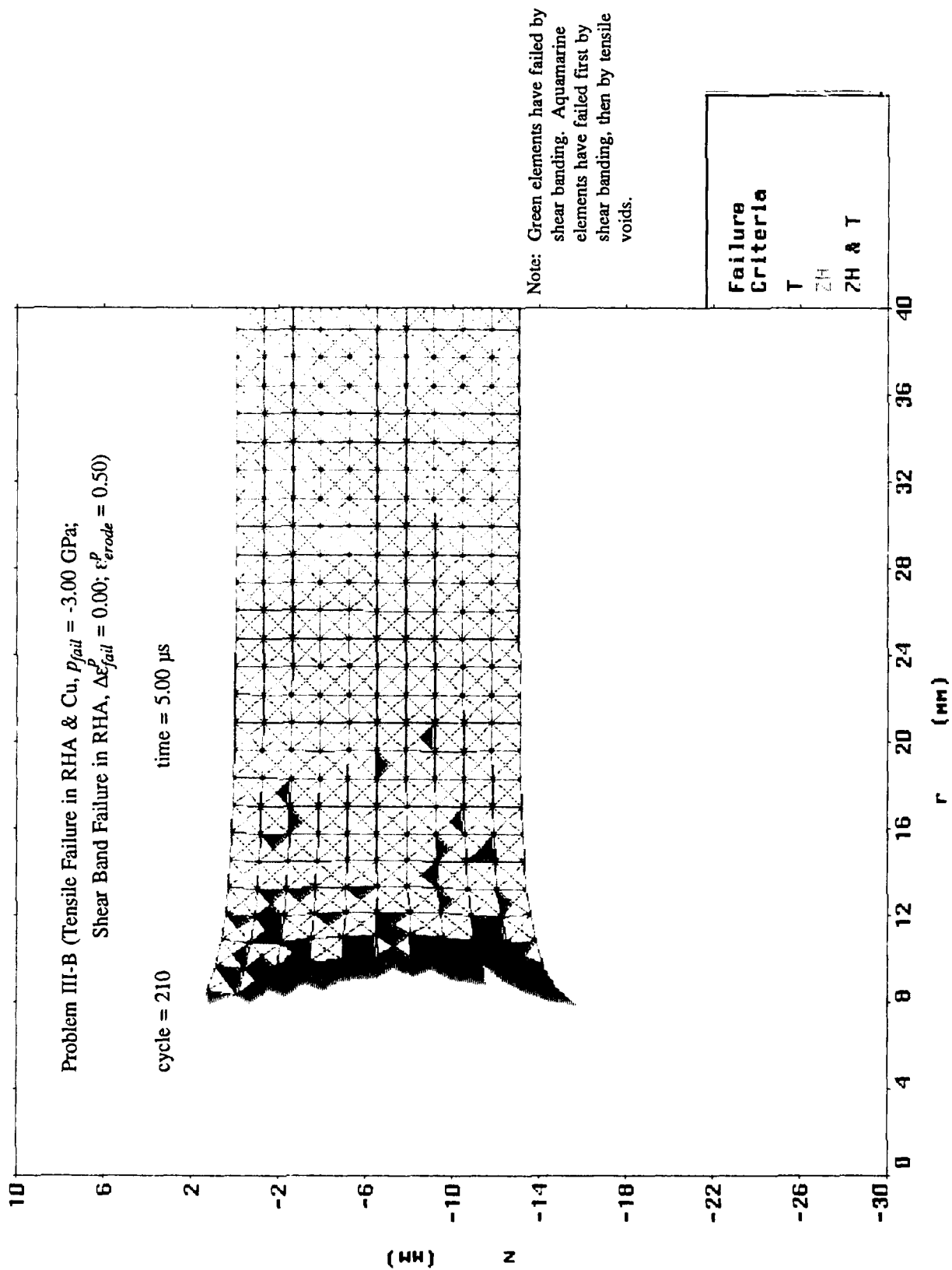


Figure 44. Mesh Plot at 5.00  $\mu$ s After Impact for Problem III-B.

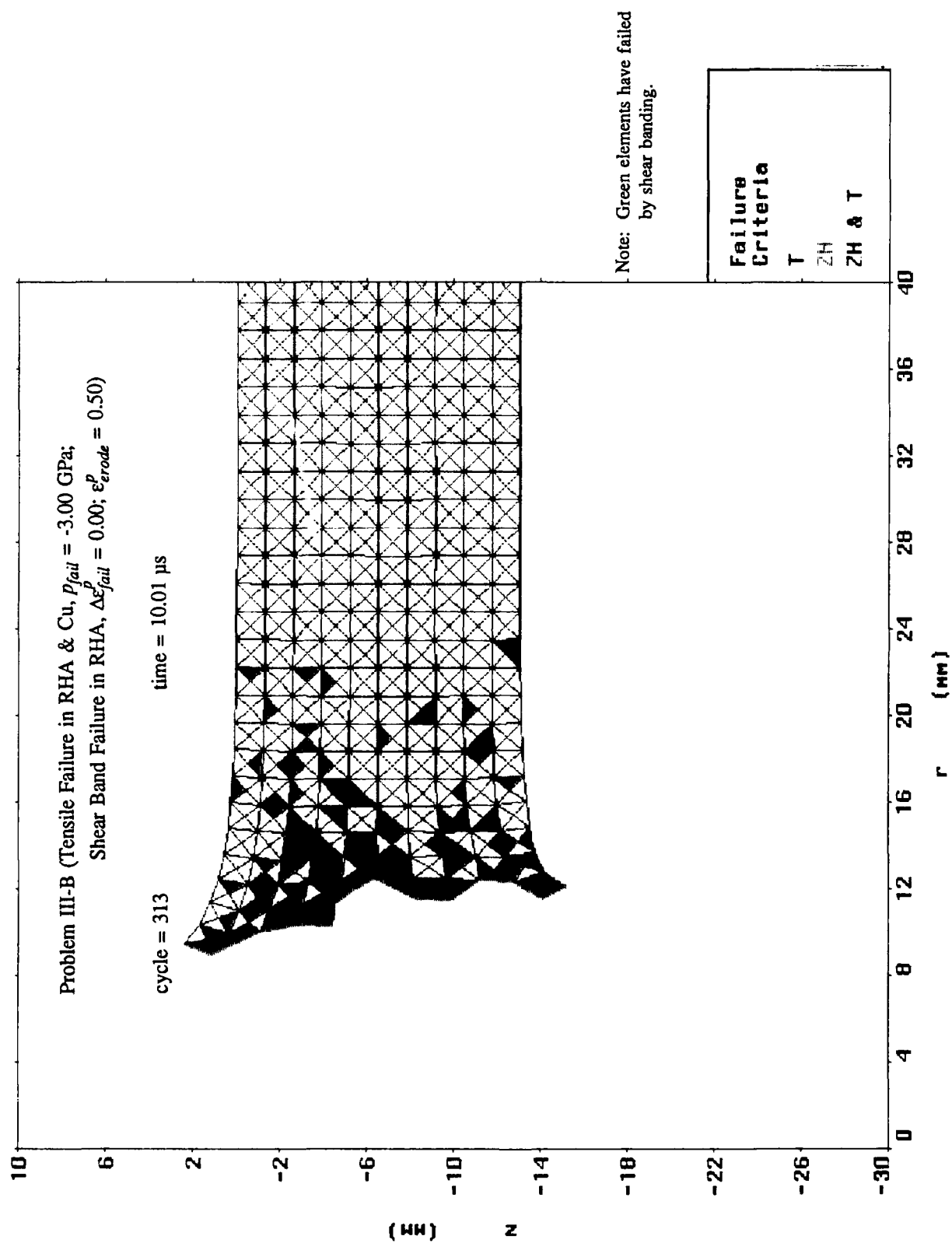


Figure 45. Mesh Plot at 10.01  $\mu$ s After Impact for Problem III-B.

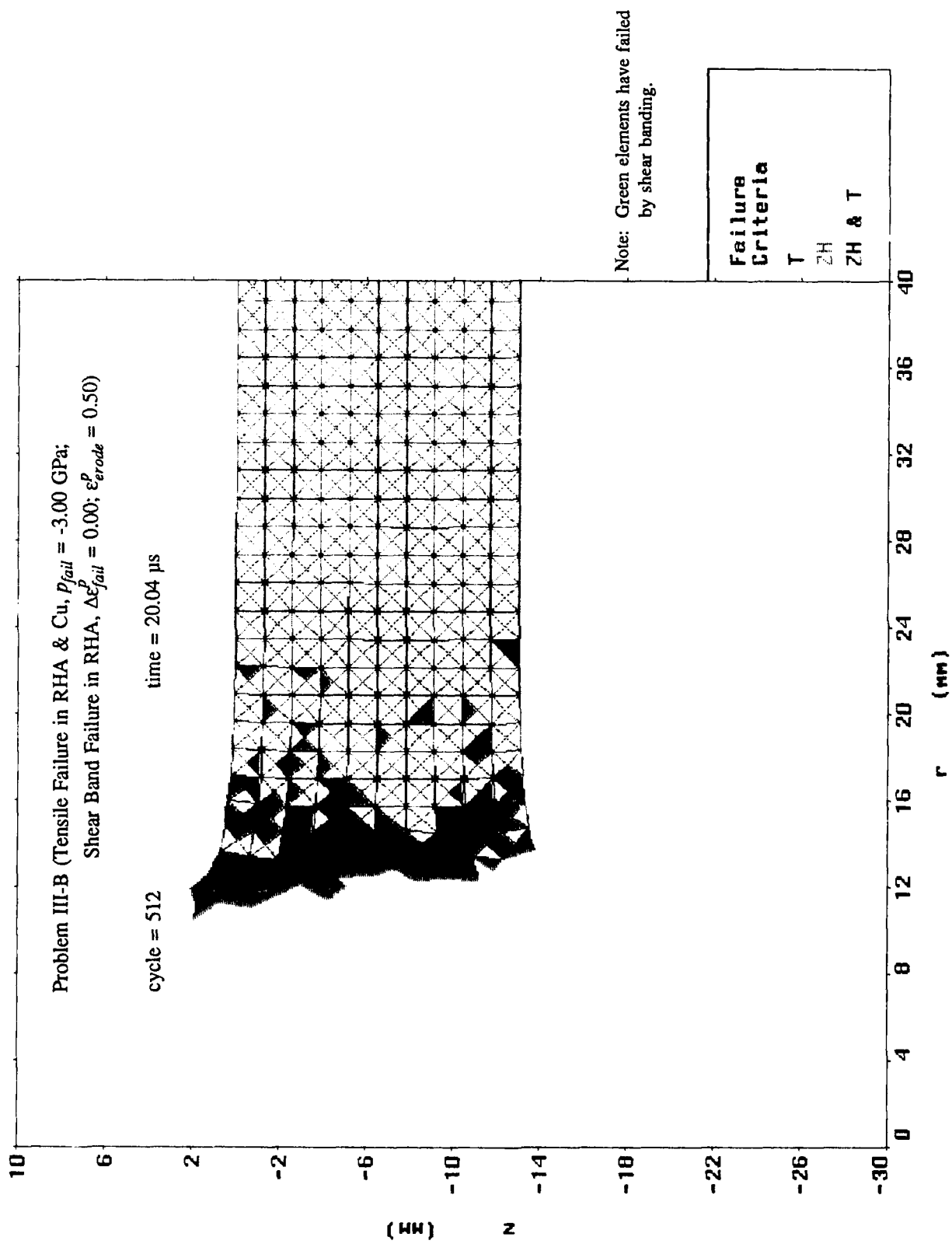


Figure 46. Mesh Plot at 20.04  $\mu$ s After Impact for Problem III-B.

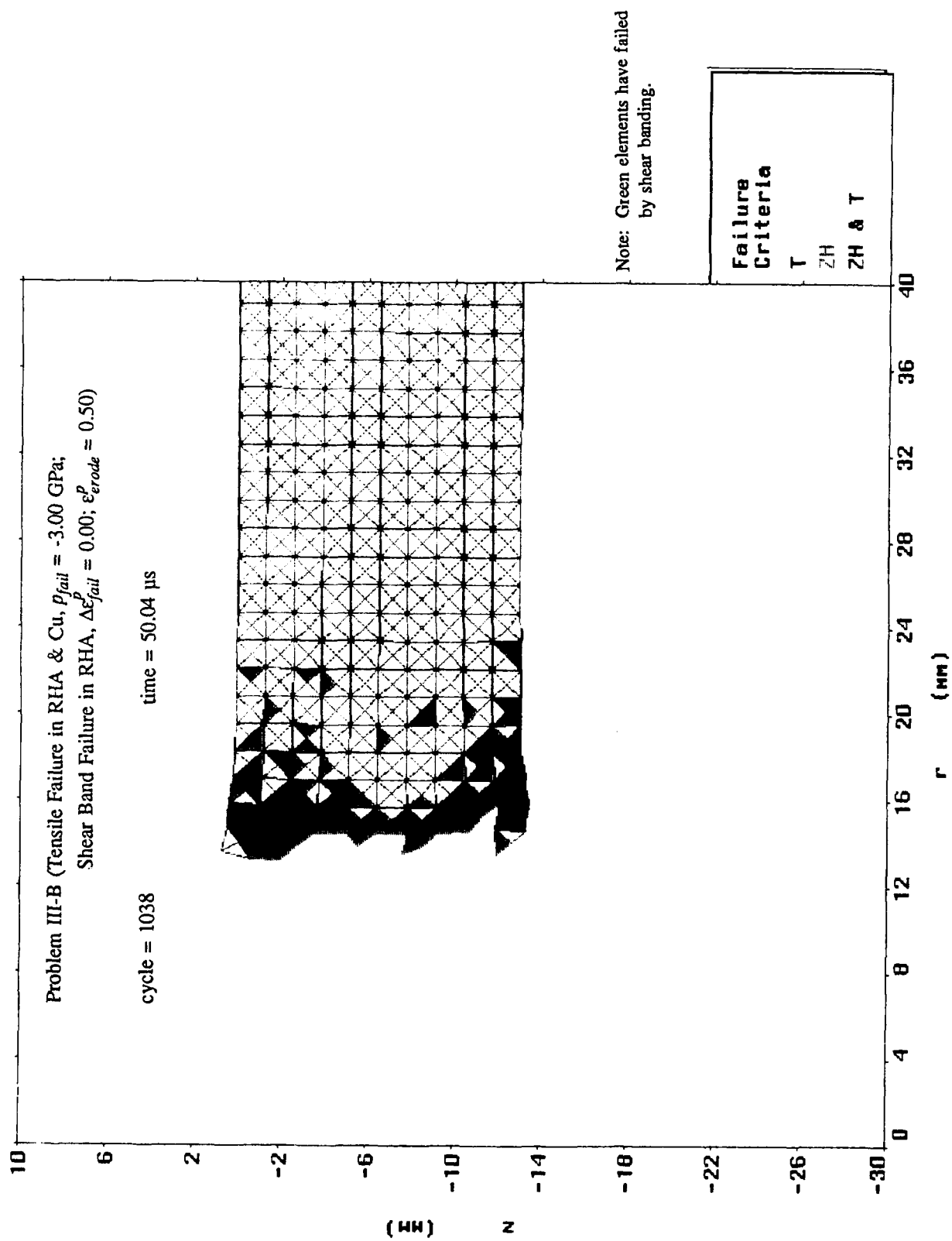


Figure 47. Mesh Plot at 50.04  $\mu$ s After Impact for Problem III-B.

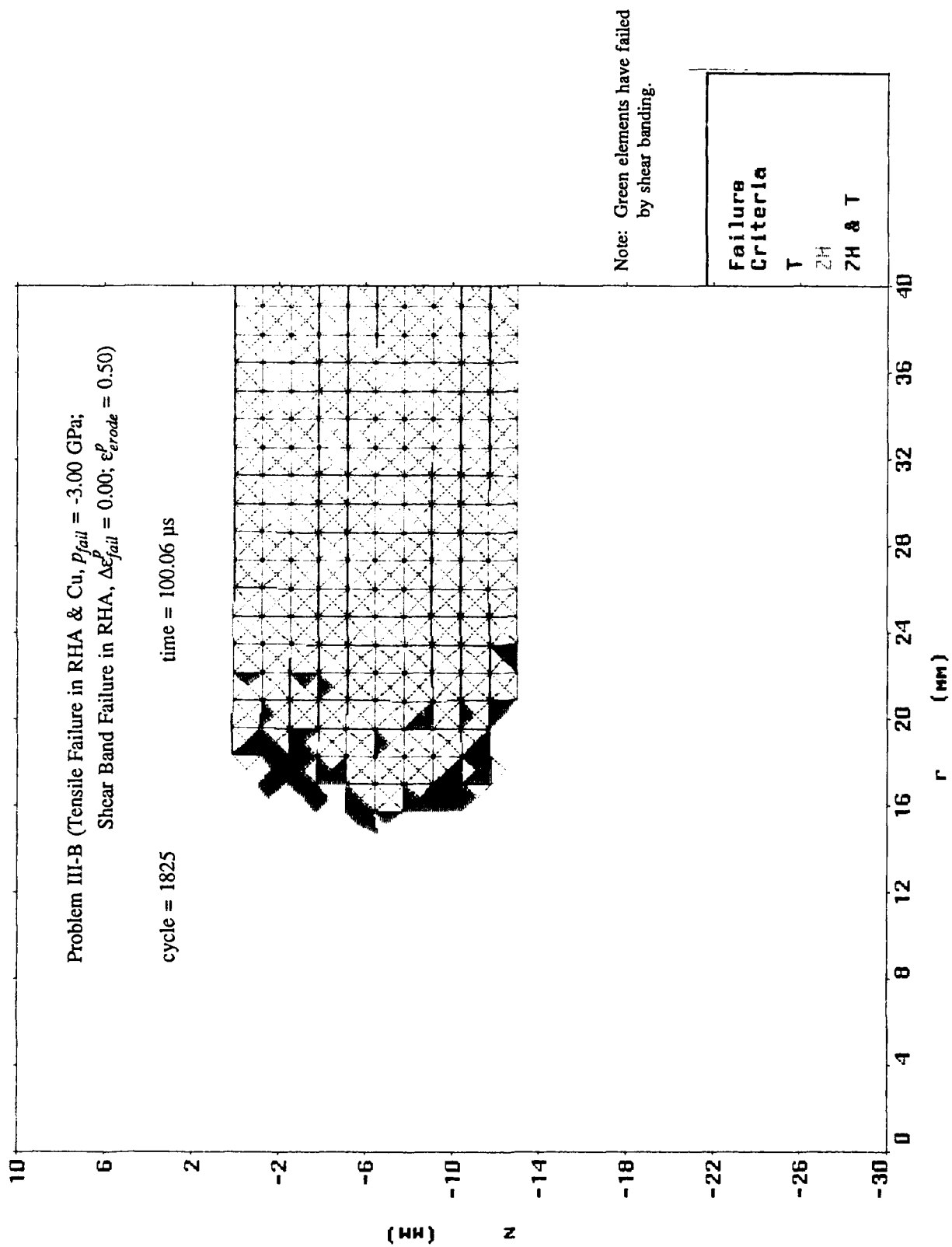


Figure 48. Mesh Plot at 100.06  $\mu$ s After Impact for Problem III-B.

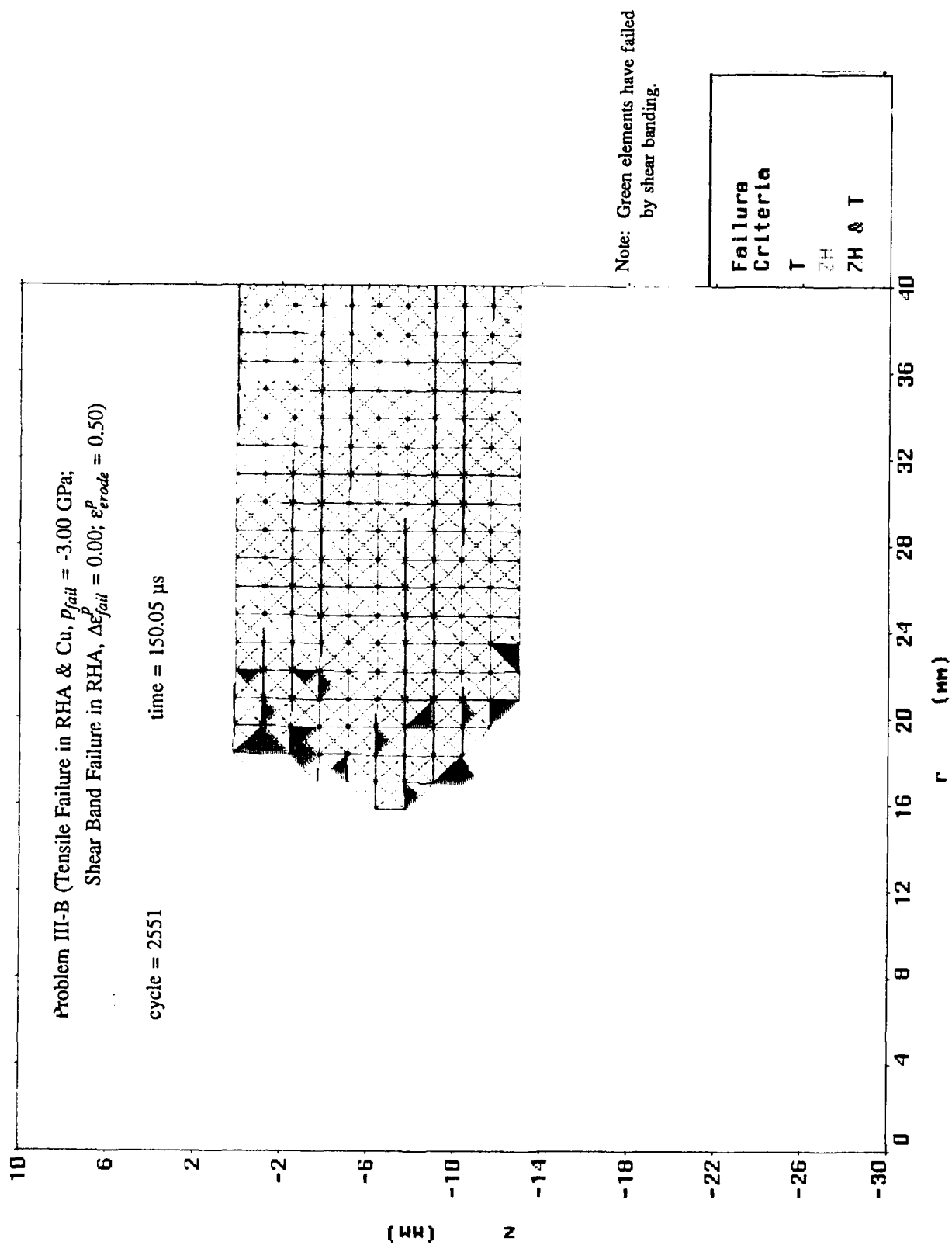


Figure 49. Mesh Plot at 150.05  $\mu$ s After Impact for Problem III-B.

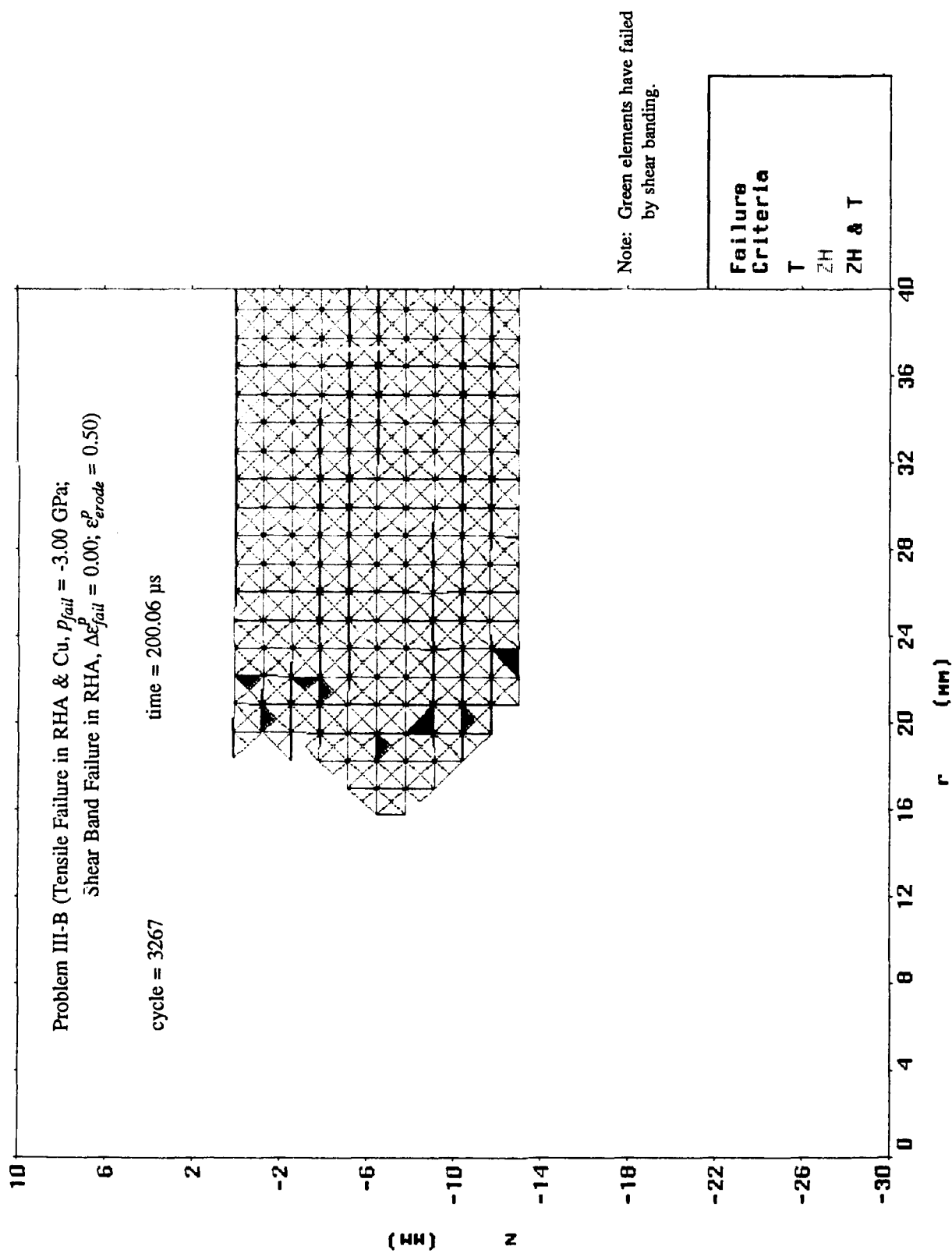


Figure 50. Mesh Plot at 200.06  $\mu s$  After Impact for Problem III-B.

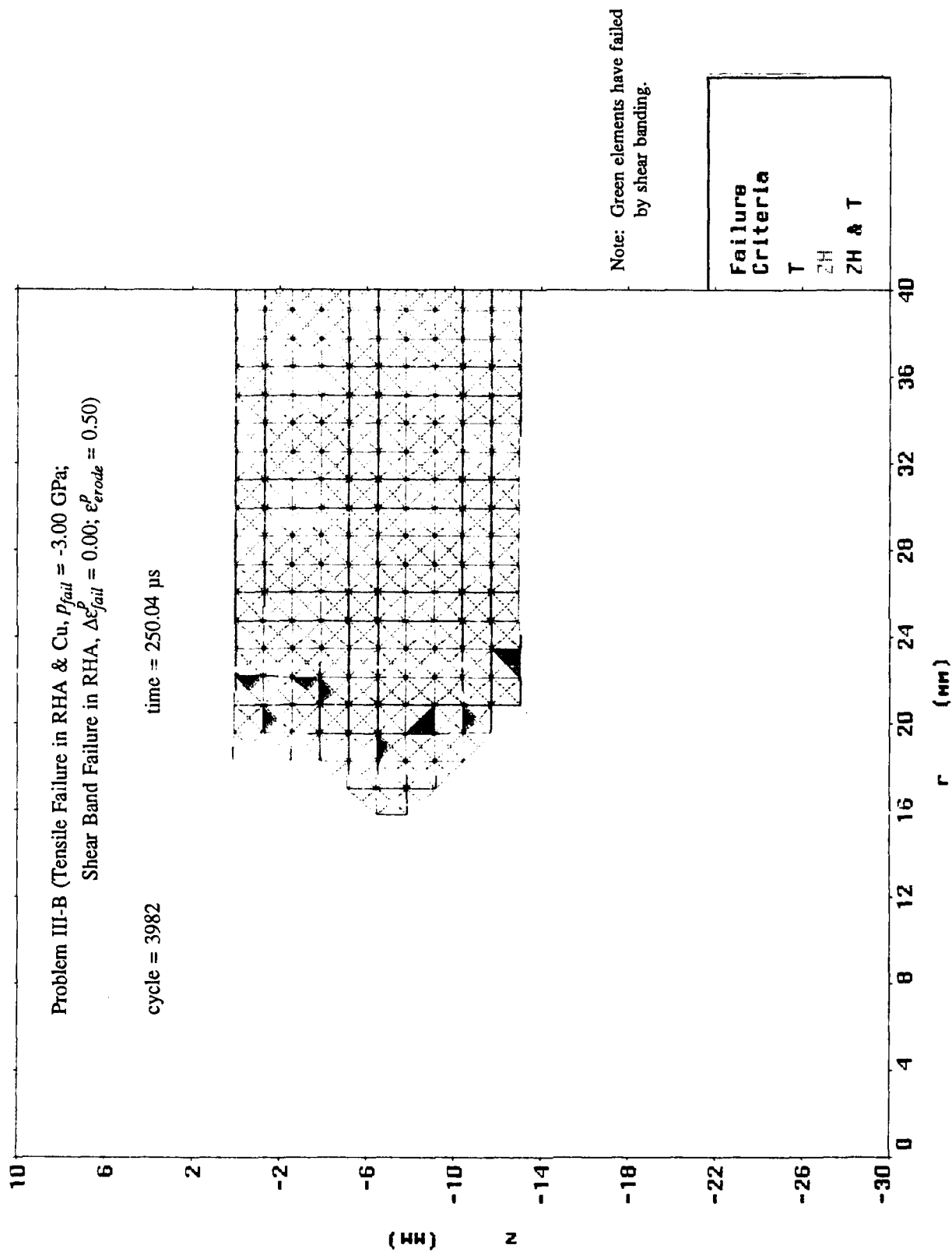


Figure 51. Mesh Plot at 250.04  $\mu$ s After Impact for Problem III-B.

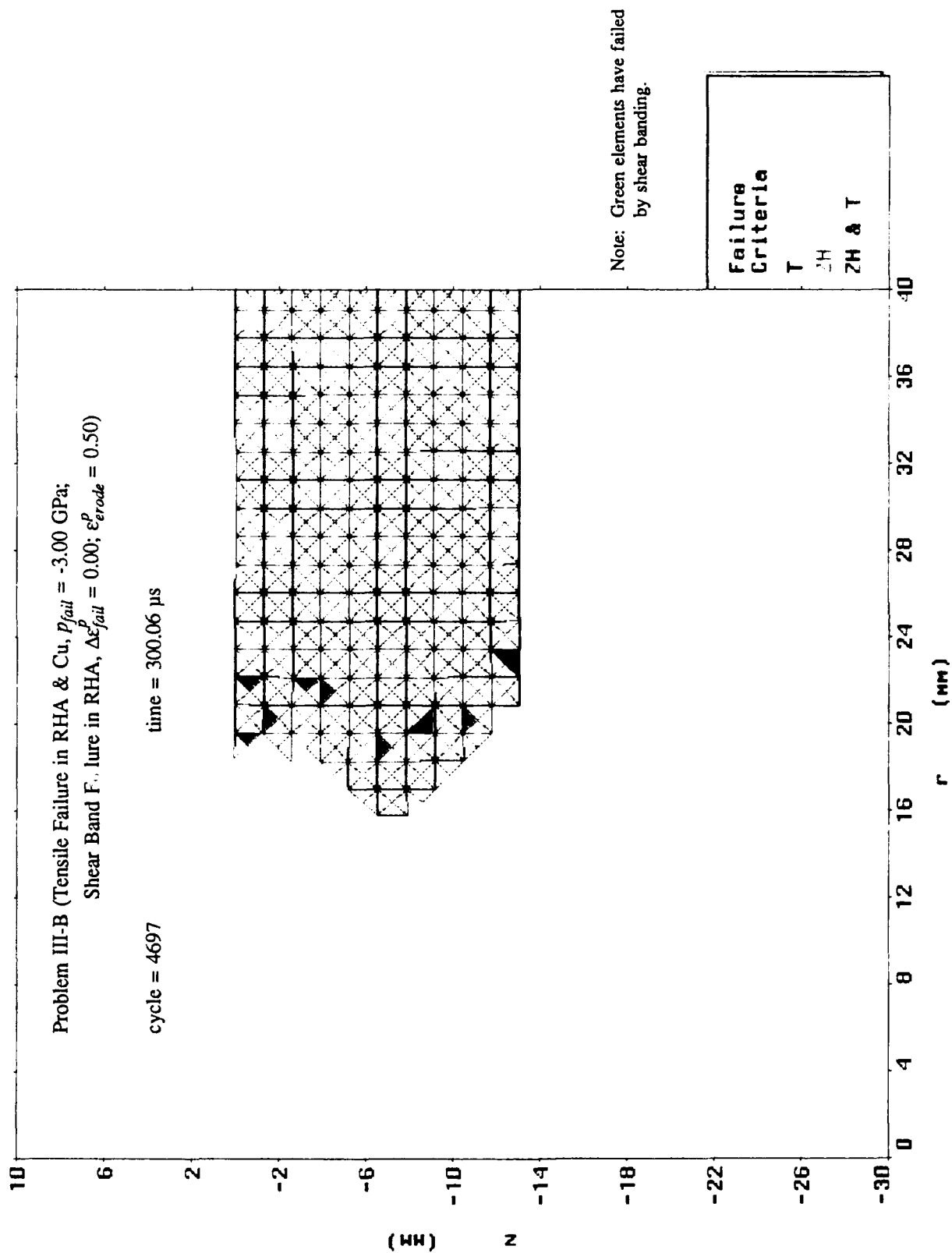


Figure 52. Mesh Plot at 300.06  $\mu$ s After Impact for Problem III-B.

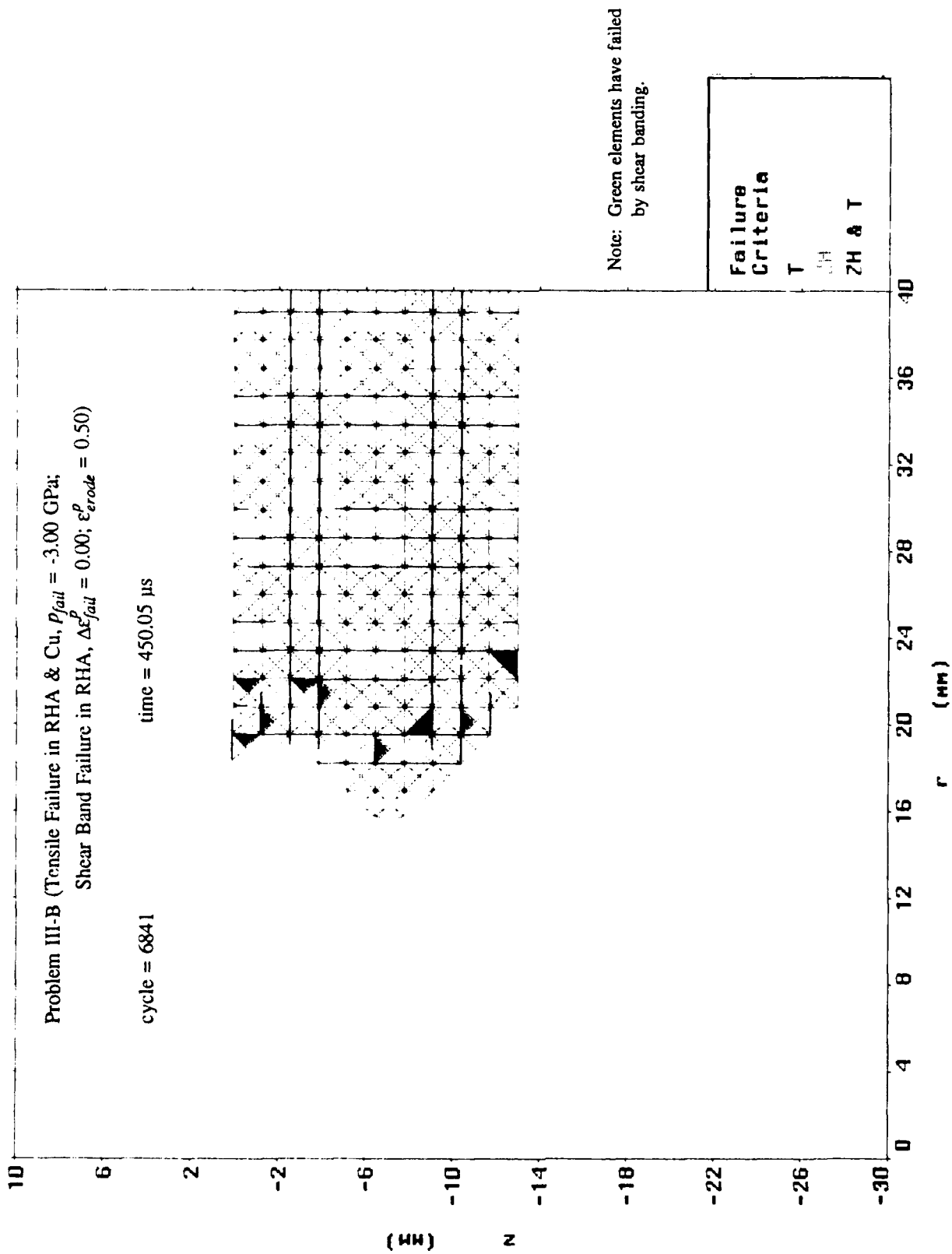


Figure 53. Mesh Plot at 450.05  $\mu$ s After Impact for Problem III-B.

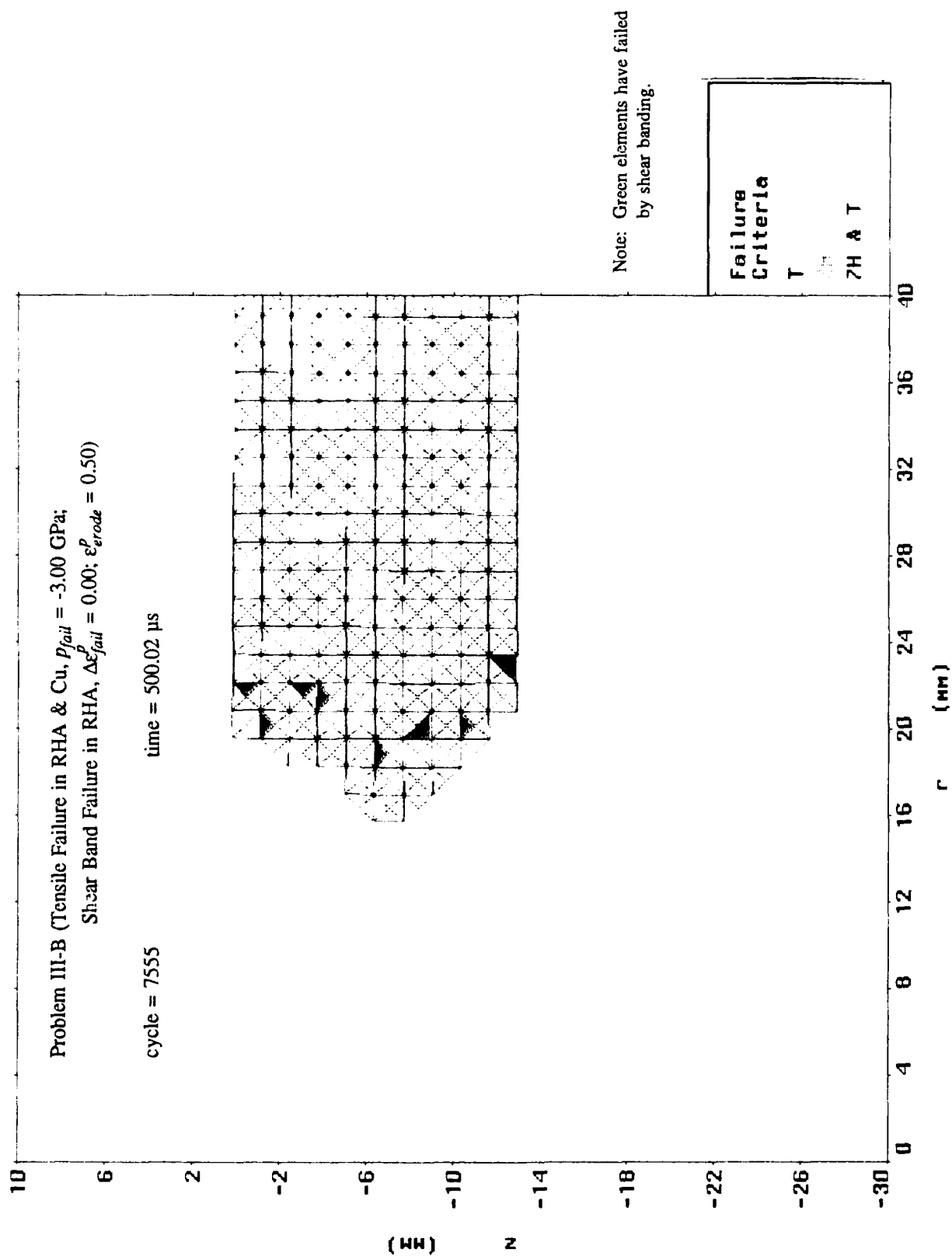


Figure 54. Mesh Plot at 500.02  $\mu$ s After Impact for Problem III-B.

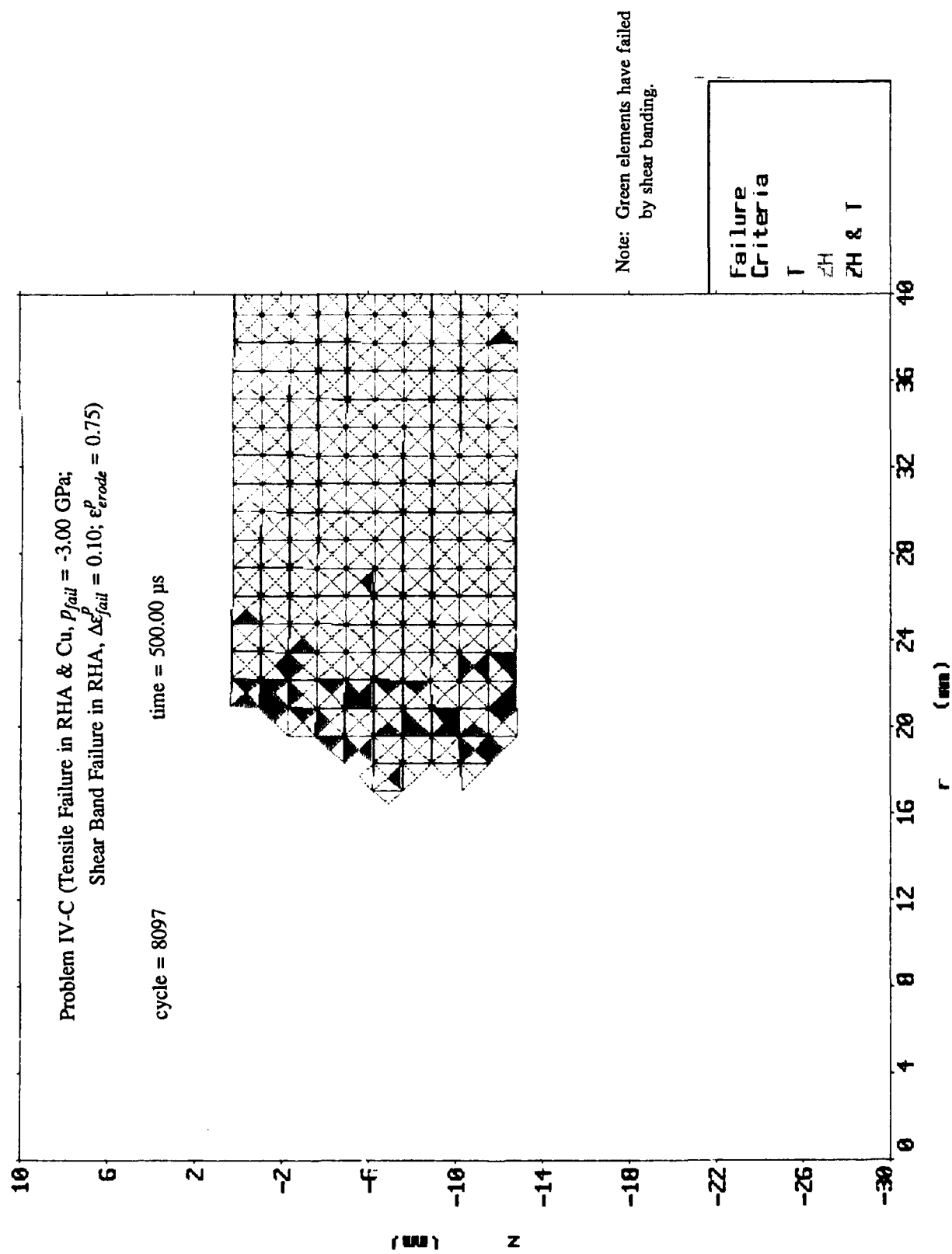


Figure 55. Mesh Plot at 500.00  $\mu$ s After Impact for Problem IV-C.

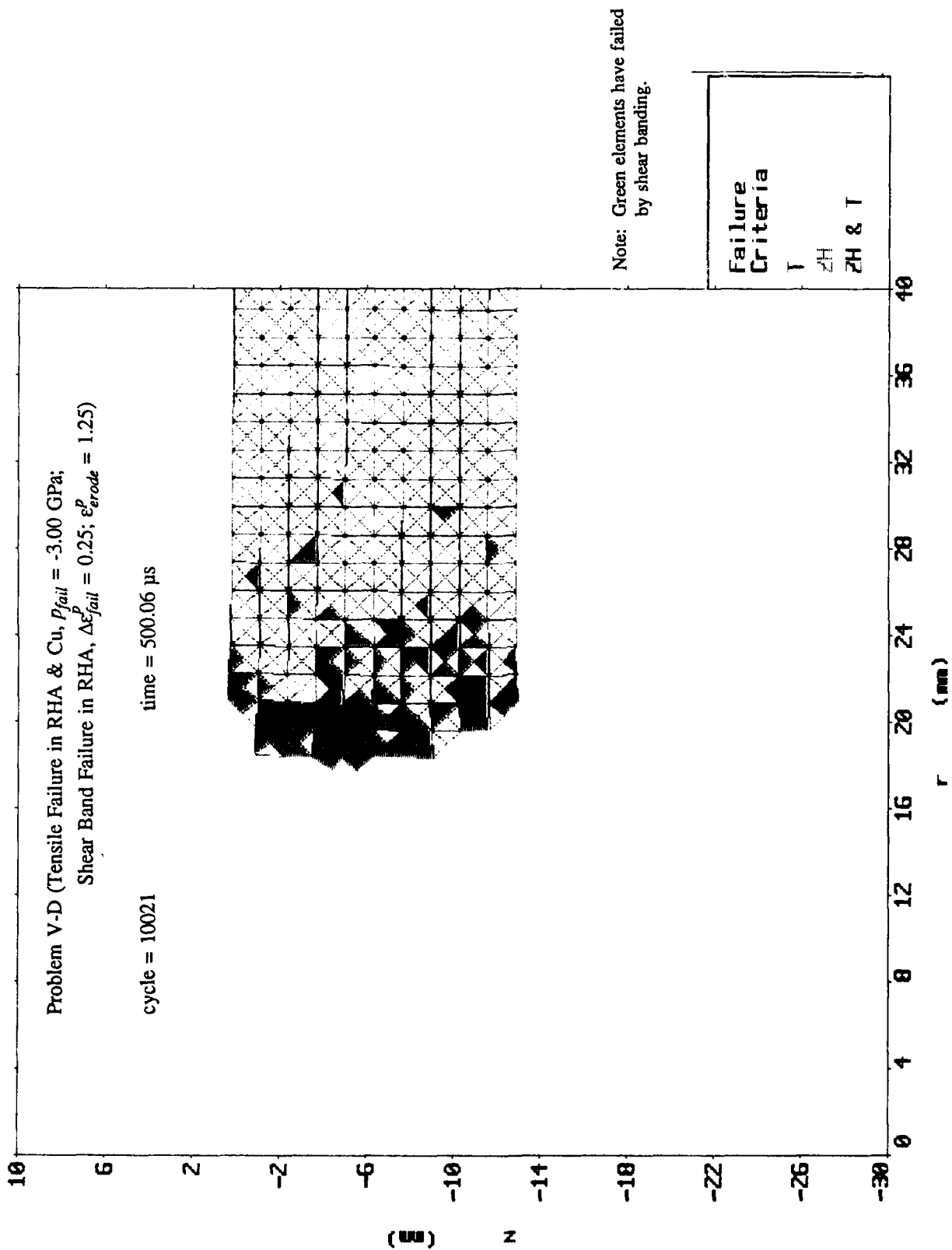


Figure 56. Mesh Plot at 500.06  $\mu$ s After Impact for Problem V-D.

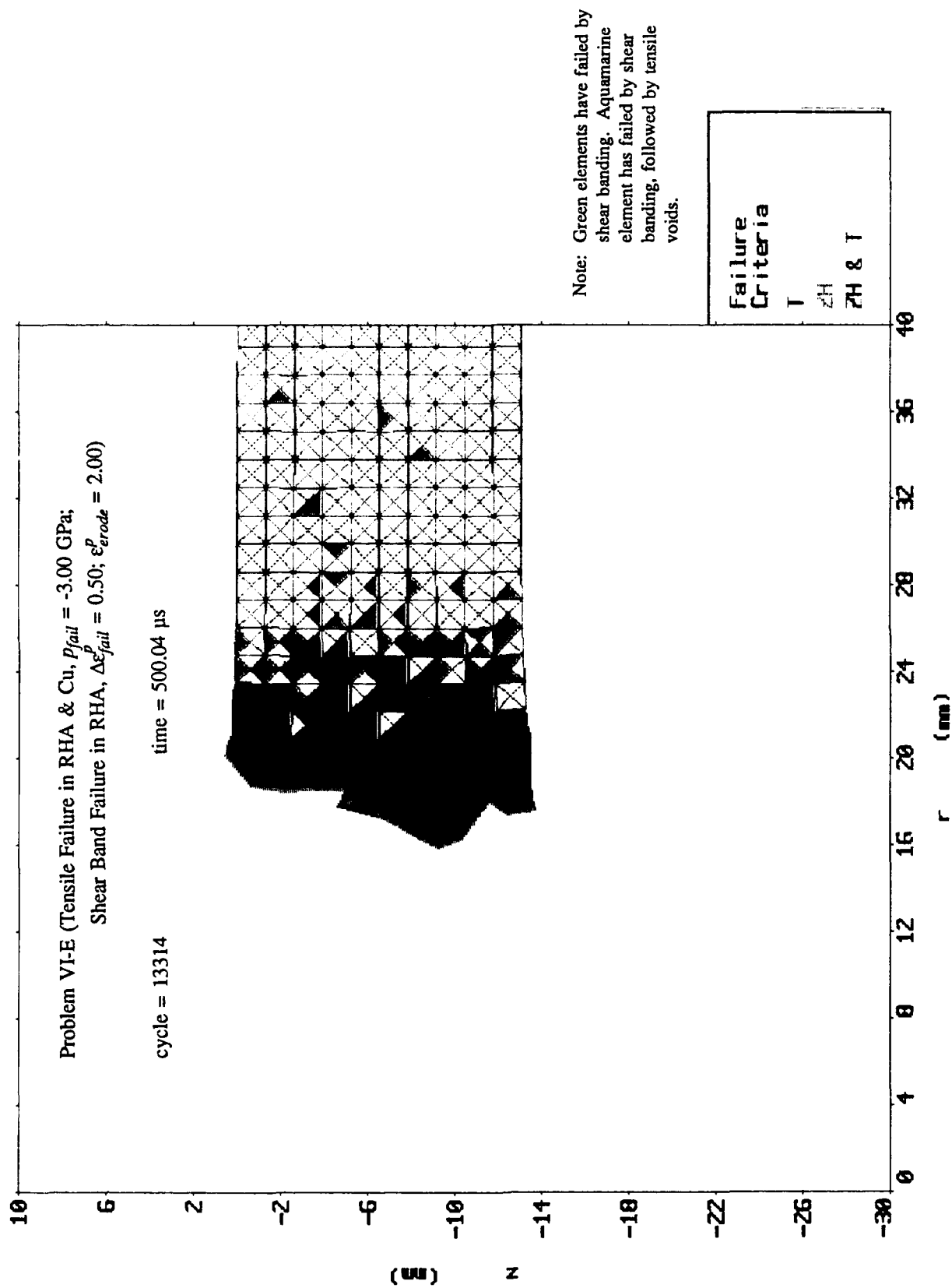


Figure 57. Mesh Plot at 500.04  $\mu$ s After Impact for Problem VI-E.

Problem Series III (Tensile Failure in RHA & Cu,  $p_{fail} = -3.00$  GPa;  
Shear Band Failure in RHA,  $\Delta \epsilon_{fail}^p = 0.00$ )

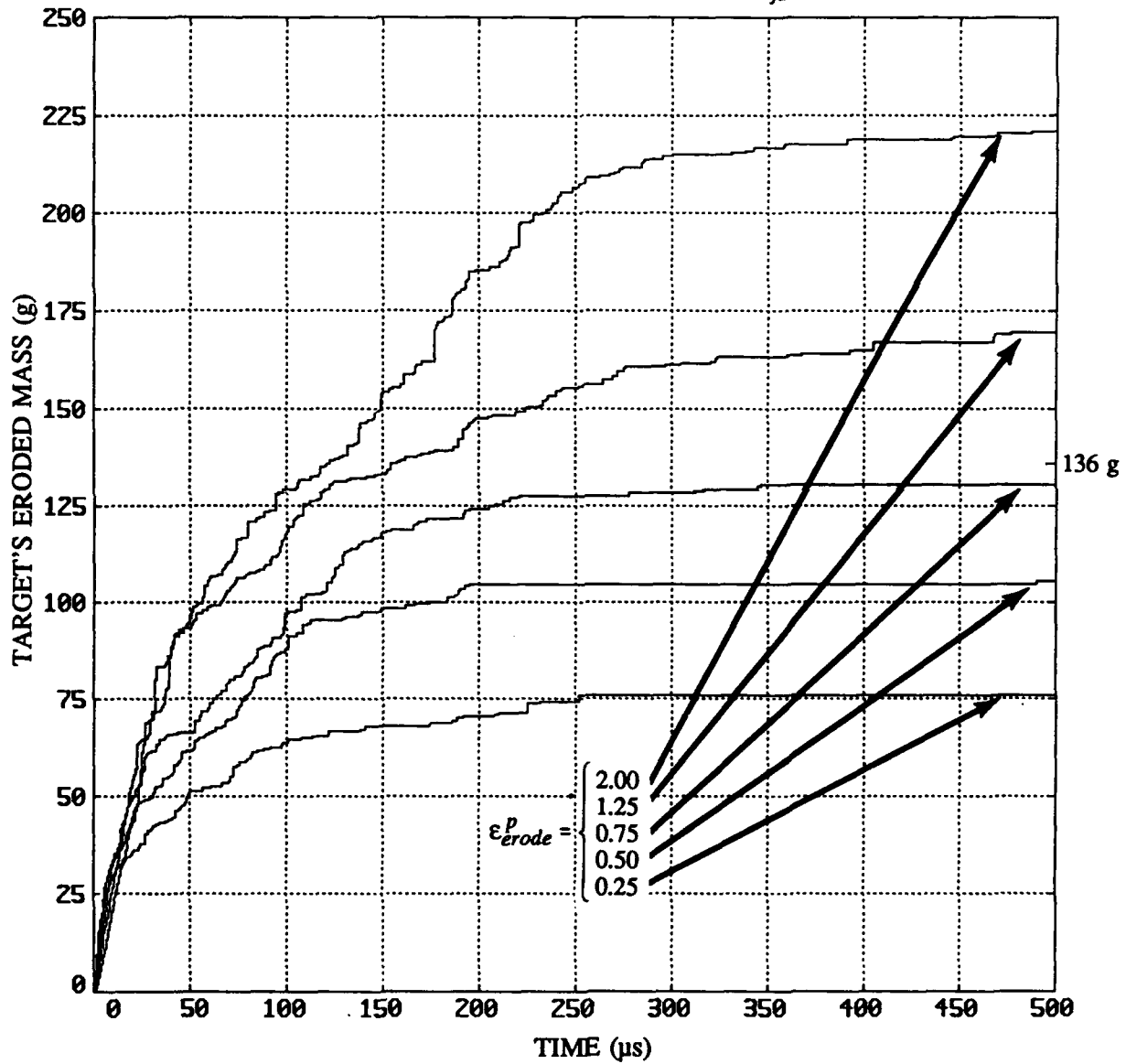


Figure 58. Mass Lost From Target Plate vs. Time for Problem Series III.

Problem Series IV (Tensile Failure in RHA & Cu,  $p_{fail} = -3.00$  GPa;  
 Shear Band Failure in RHA,  $\Delta \epsilon_{fail}^p = 0.10$ )

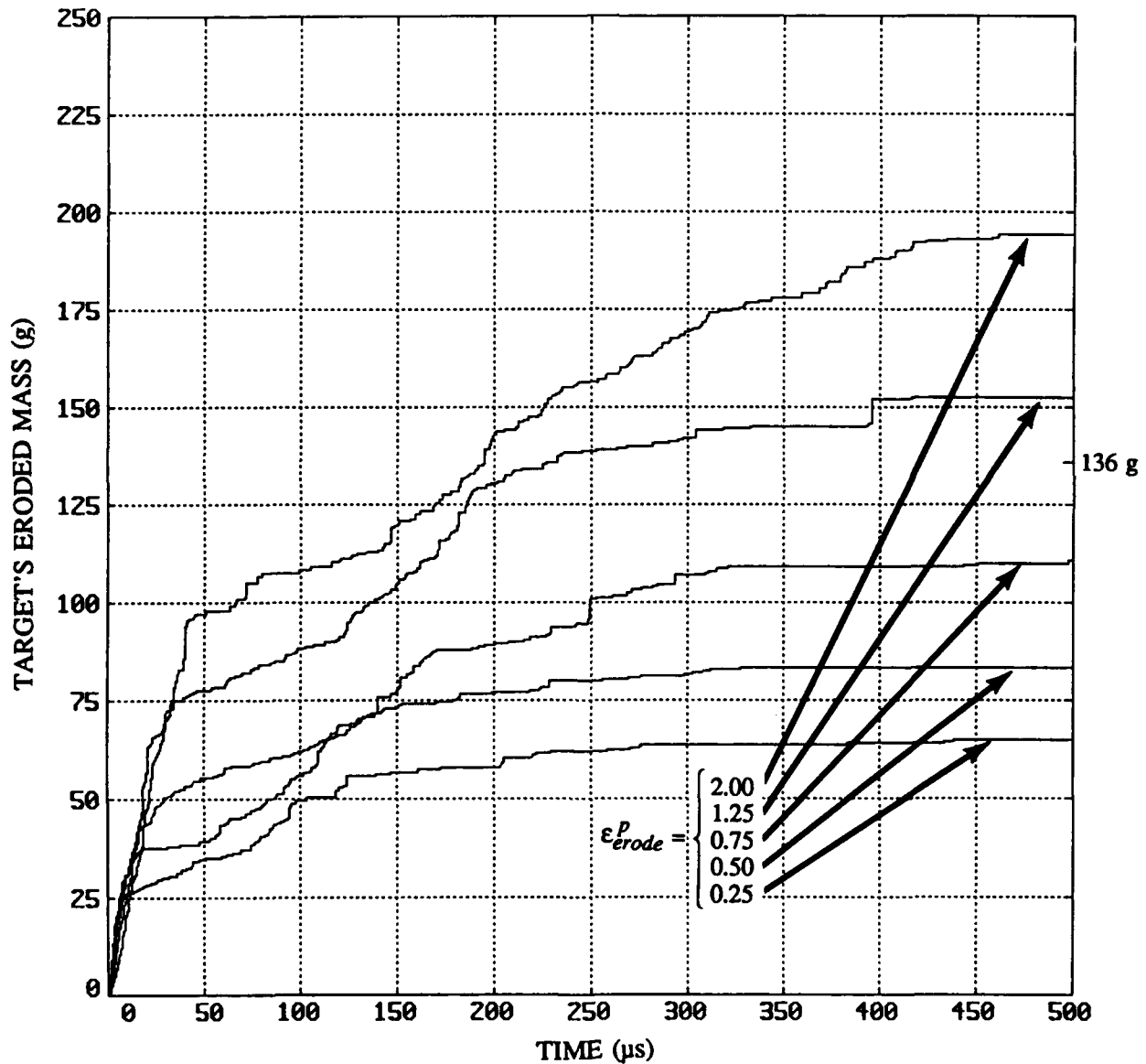


Figure 59. Mass Lost From Target Plate vs. Time for Problem Series IV.

Problem Series V (Tensile Failure in RHA & Cu,  $p_{fail} = -3.00$  GPa;  
 Shear Band Failure in RHA,  $\Delta\epsilon_{fail}^p = 0.25$ )

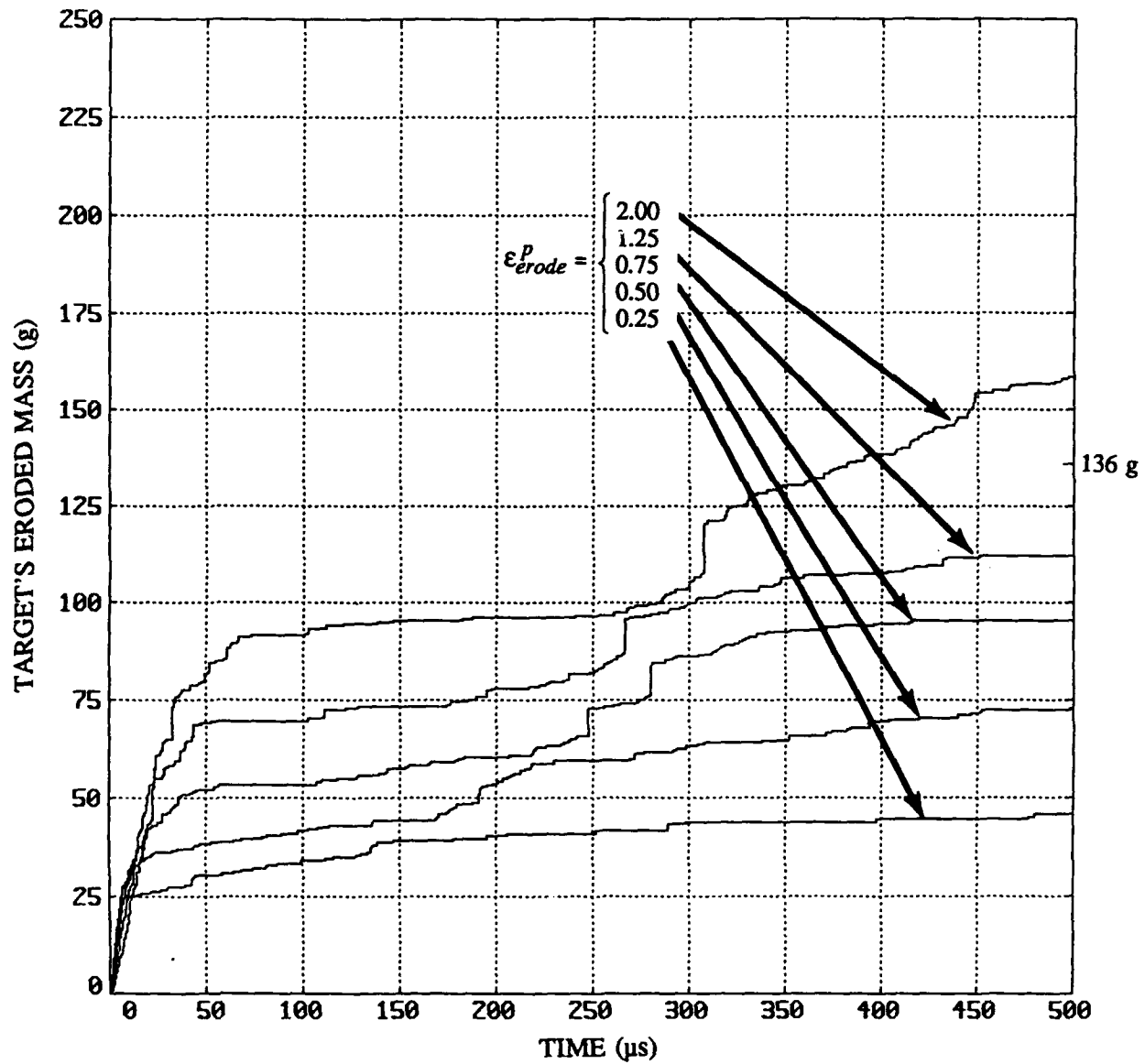


Figure 60. Mass Lost From Target Plate vs. Time for Problem Series V.

Problem Series VI (Tensile Failure in RHA & Cu,  $p_{fail} = -3.00$  GPa;  
Shear Band Failure in RHA,  $\Delta \epsilon_{fail}^p = 0.50$ )

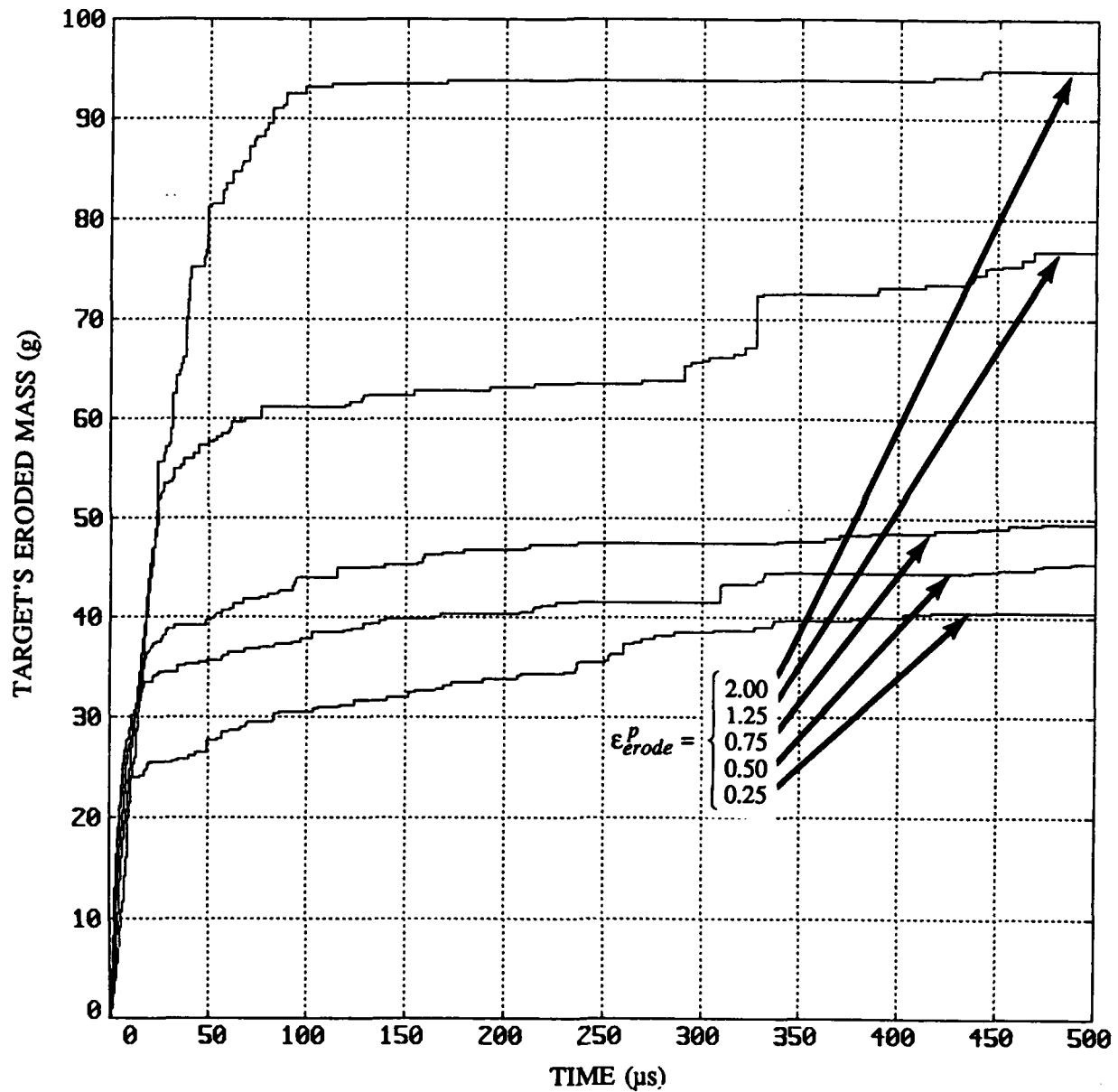


Figure 61. Mass Lost From Target Plate vs. Time for Problem Series VI.

Problem Series VII (Tensile Failure in RHA & Cu,  $p_{fail} = -3.00$  GPa;  
 Shear Band Failure in RHA,  $\Delta \epsilon_{fail}^p = 0.75$ )

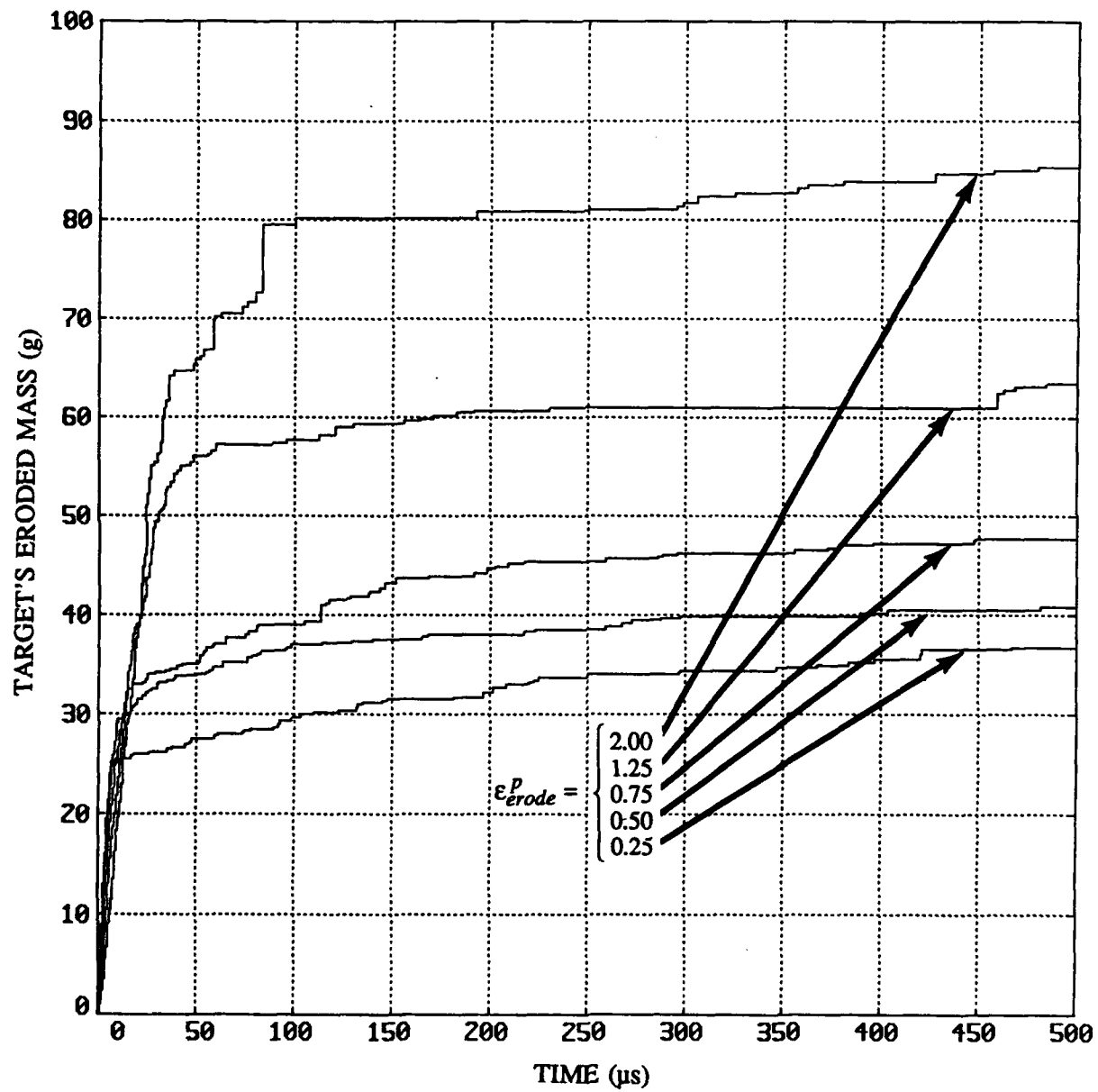


Figure 62. Mass Lost From Target Plate vs. Time for Problem Series VII.

Problem Series VIII (Tensile Failure in RHA & Cu,  $p_{fail} = -3.00$  GPa;  
Shear Band Failure in RHA,  $\Delta \epsilon_{fail}^p = 1.00$ )

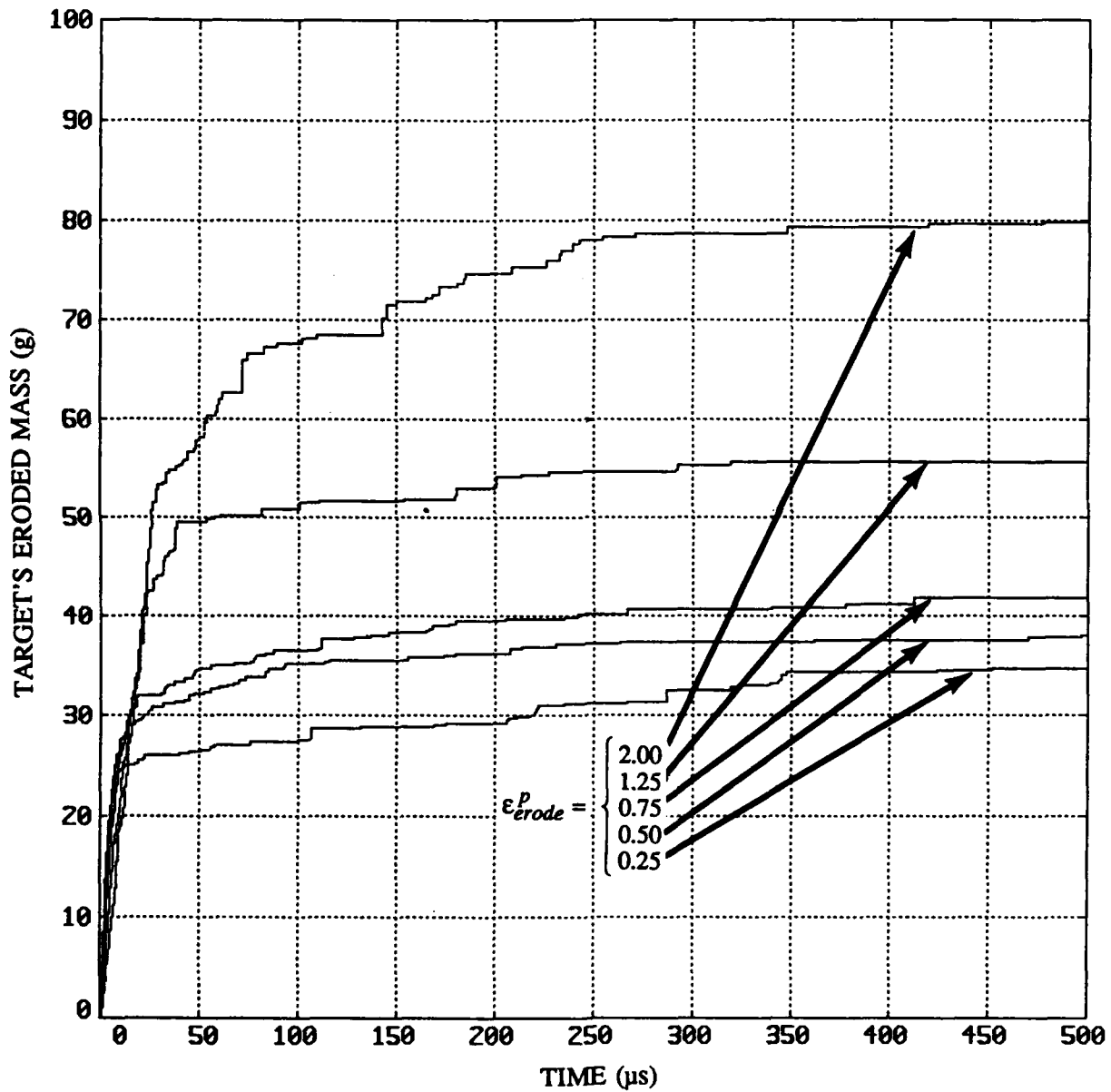


Figure 63. Mass Lost From Target Plate vs. Time for Problem Series VIII.

Problem Series III Through VIII (Tensile Failure in RHA & Cu,  $p_{fail} = -3.00$  GPa;  
Shear Band Failure in RHA,  $\Delta\epsilon_{fail}^p$  Varied)

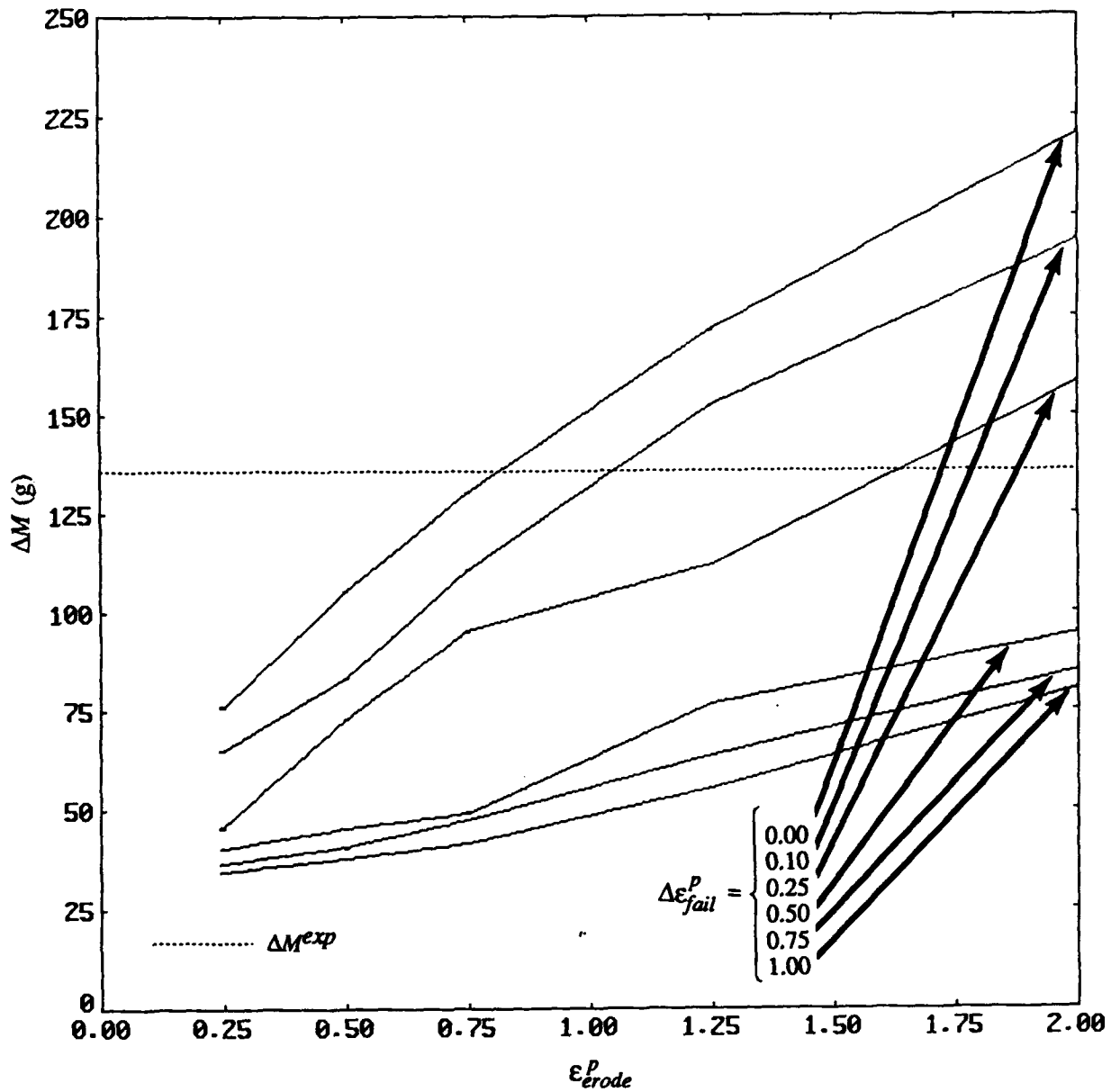


Figure 64. Computed  $\Delta M$  vs.  $\epsilon_{erosion}^p$  With  $\Delta\epsilon_{fail}^p$  a Parameter for Problem Series III Through VIII.

Problem Series III Through VIII (Tensile Failure in RHA & Cu,  $p_{fail} = -3.00$  GPa;  
Shear Band Failure in RHA,  $\Delta\epsilon_{fail}^p$  Varied)

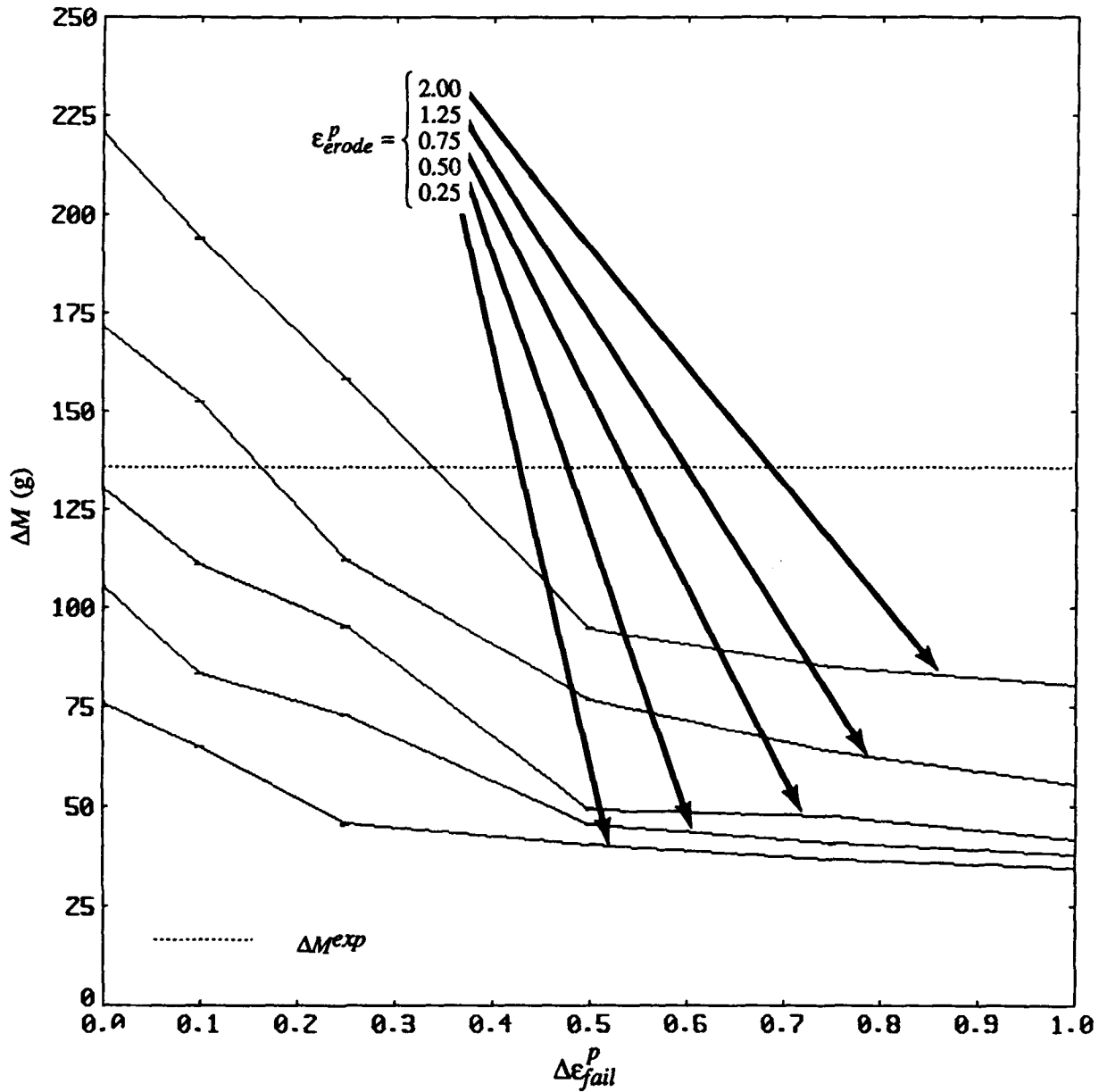


Figure 65. Computed  $\Delta M$  vs.  $\Delta\epsilon_{fail}^p$  With  $\epsilon_{erode}^p$  a Parameter for Problem Series III Through VIII.

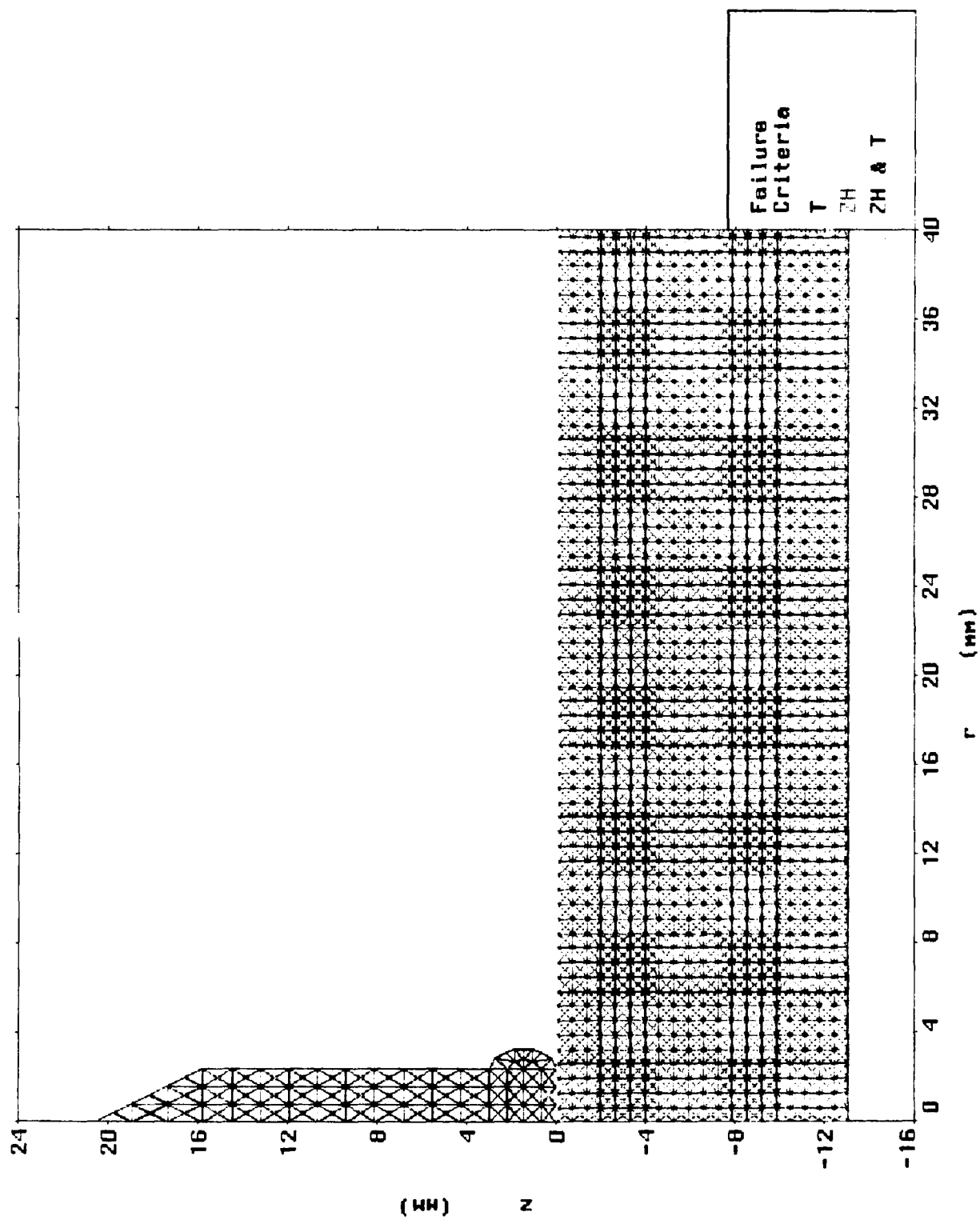


Figure 66. The Initial Mesh Used in Section 9.

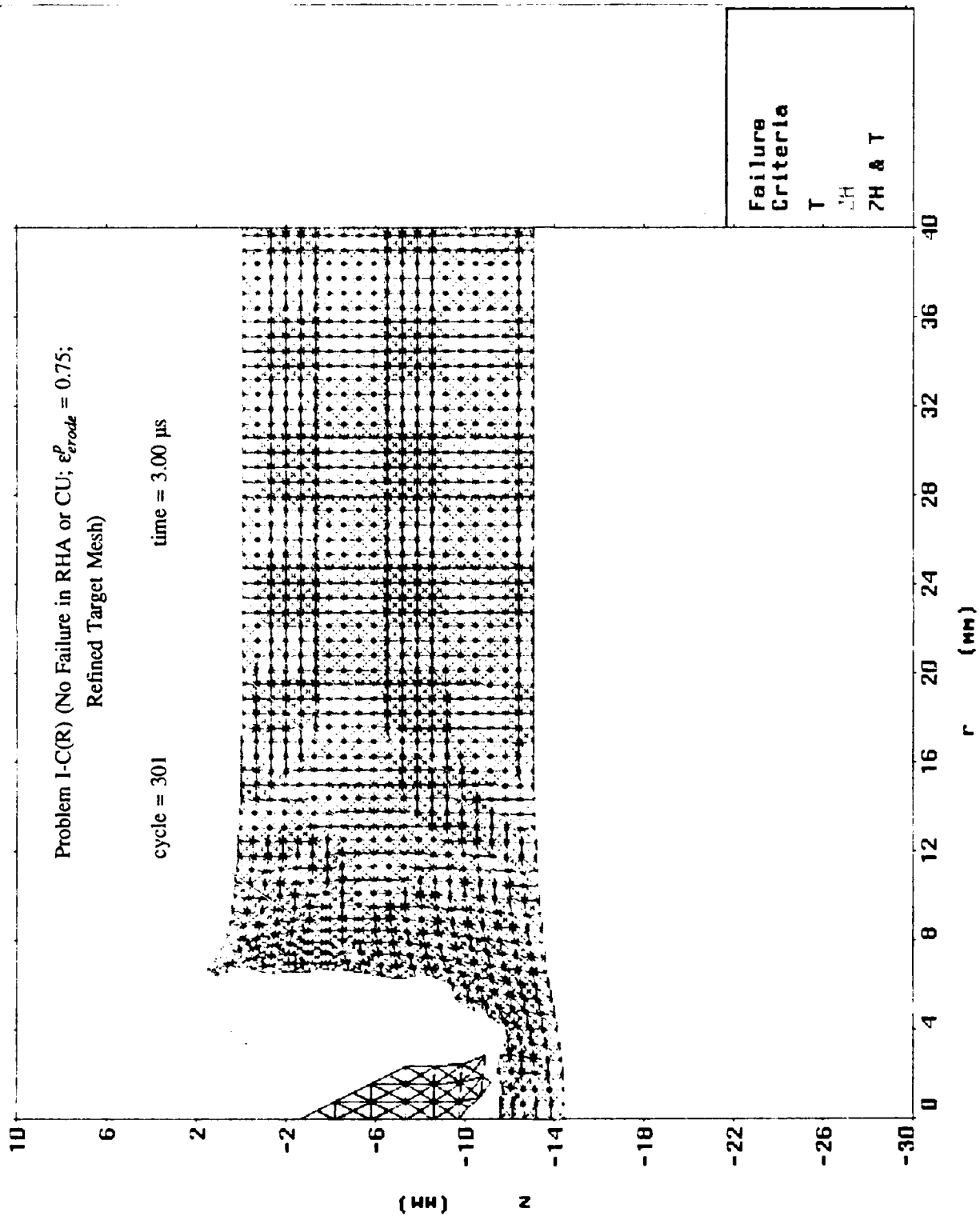


Figure 67. Mesh Plot at 3.00  $\mu\text{s}$  After Impact for Problem I-C(R).

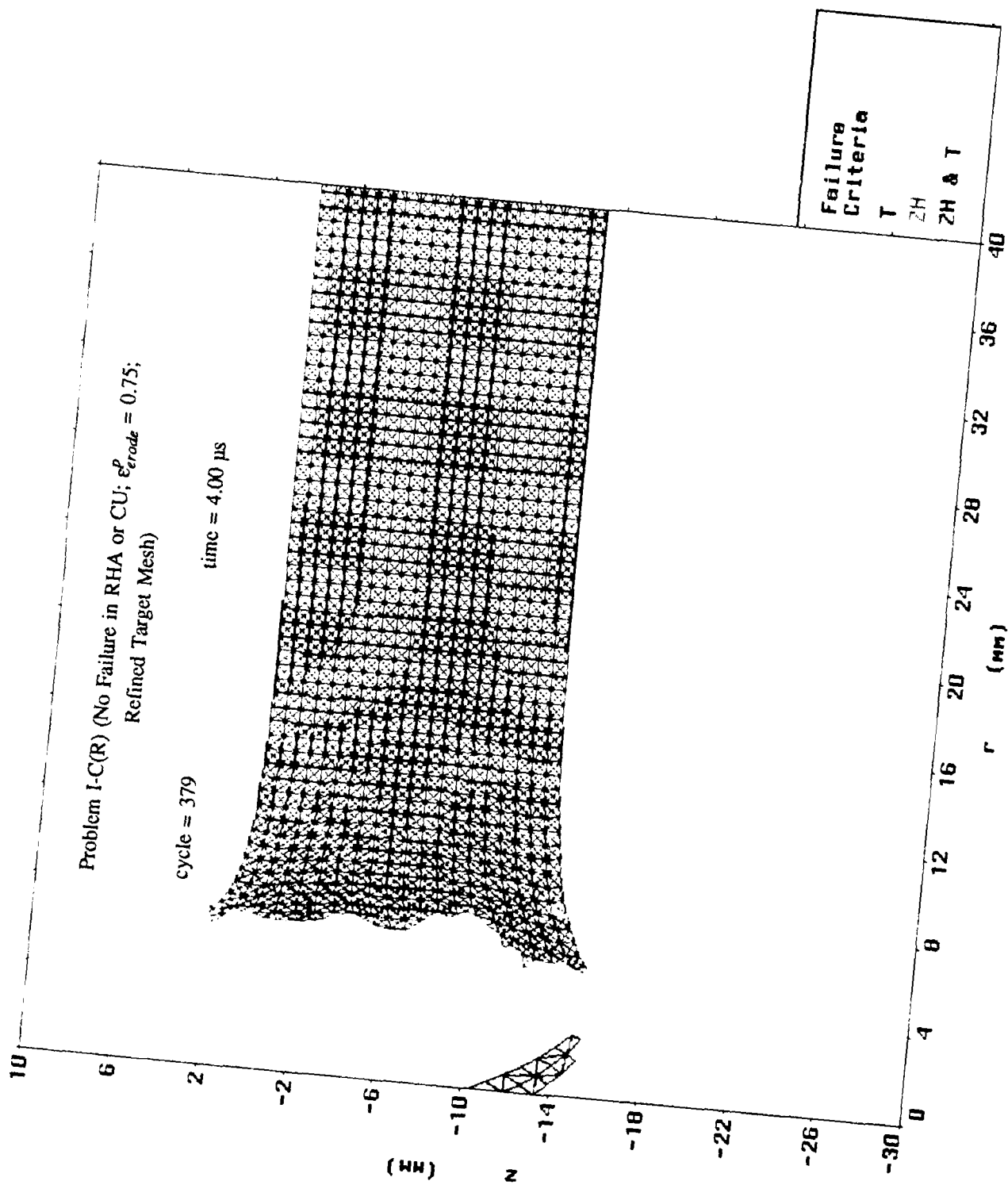


Figure 68. Mesh Plot at 4.00  $\mu$ s After Impact for Problem I-C(R).

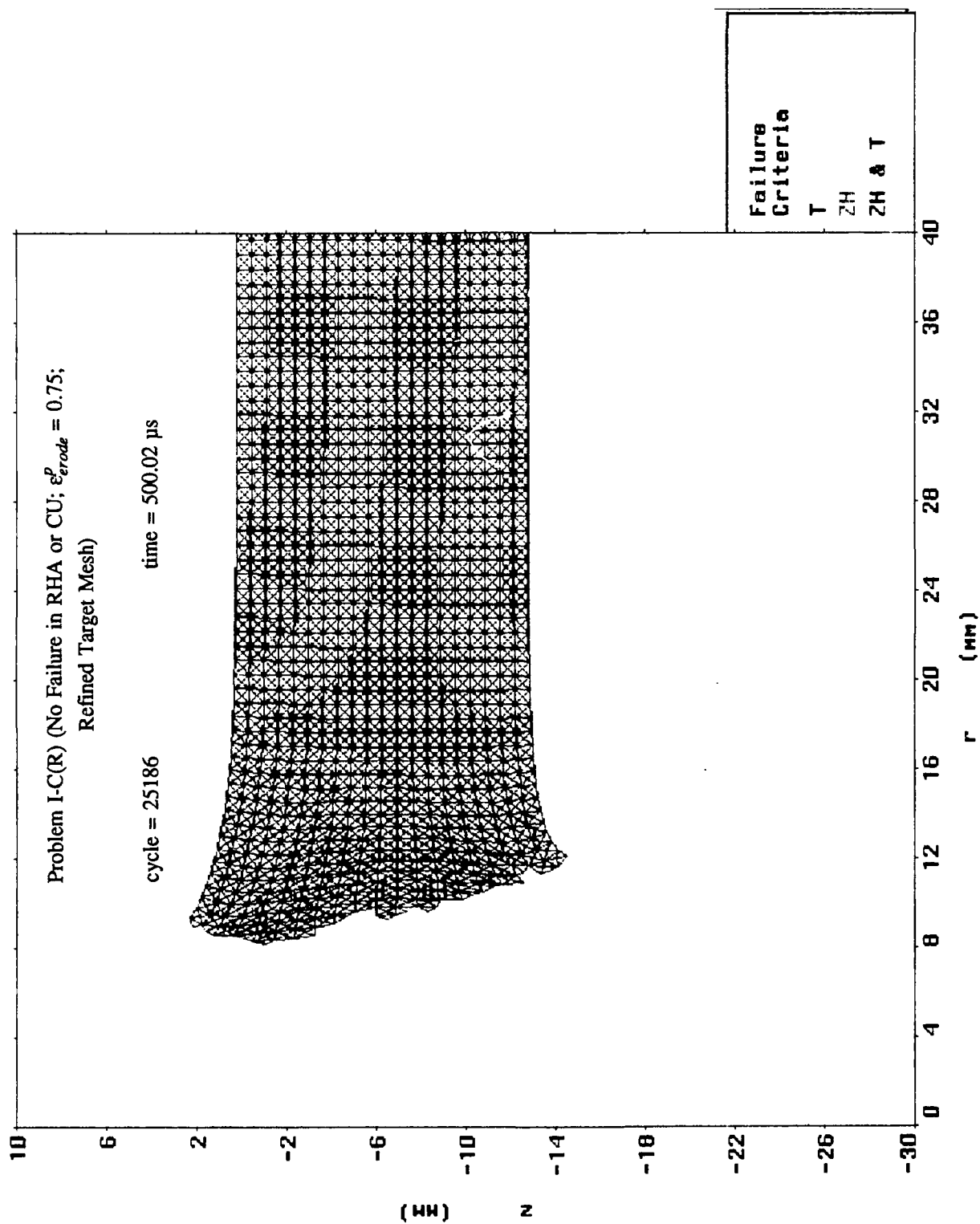


Figure 69. Mesh Plot at 500.02  $\mu$ s After Impact for Problem I-C(R).

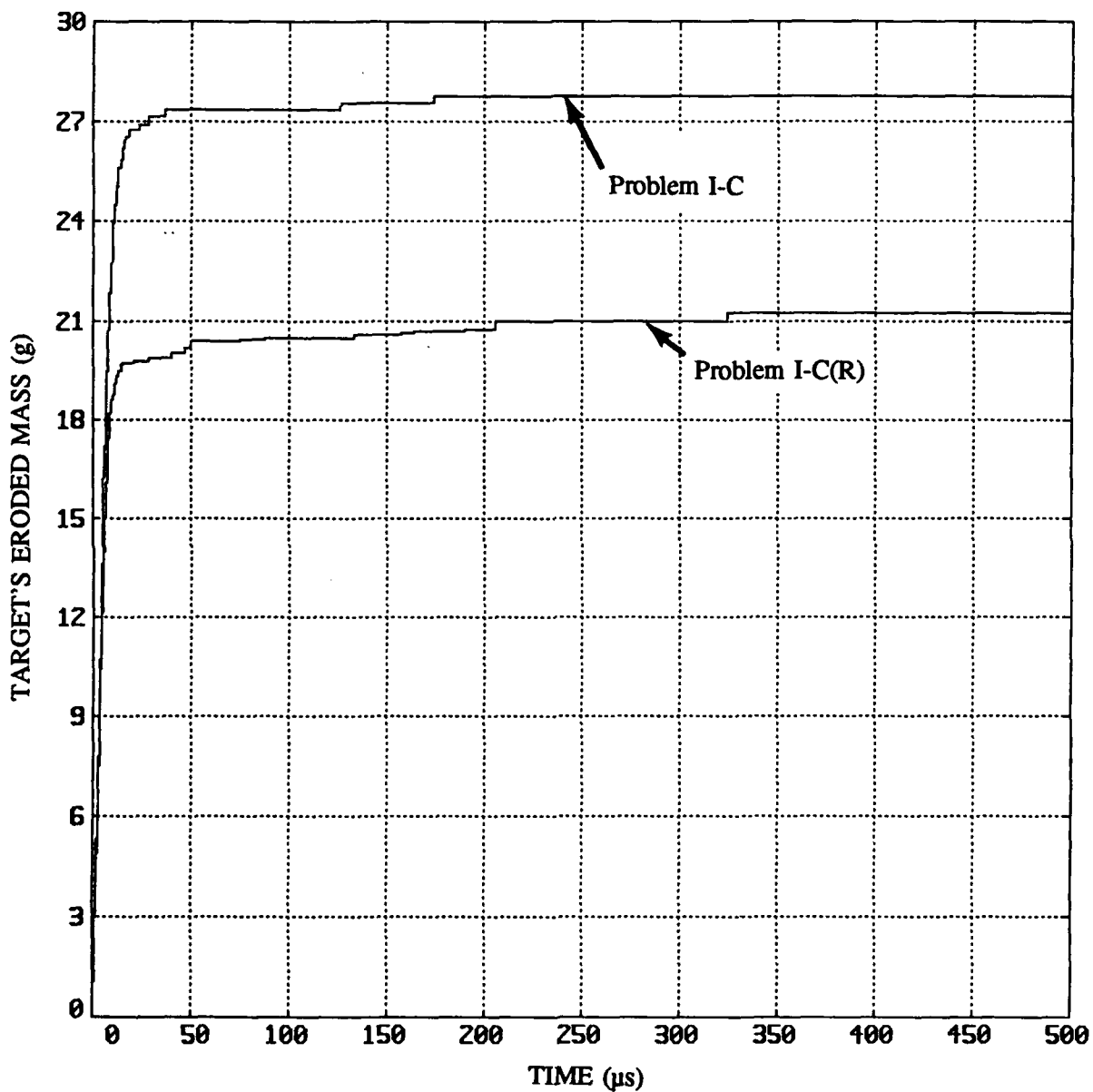


Figure 70. Mass Lost From Target Plate vs. Time for Problems I-C and I-C(R).

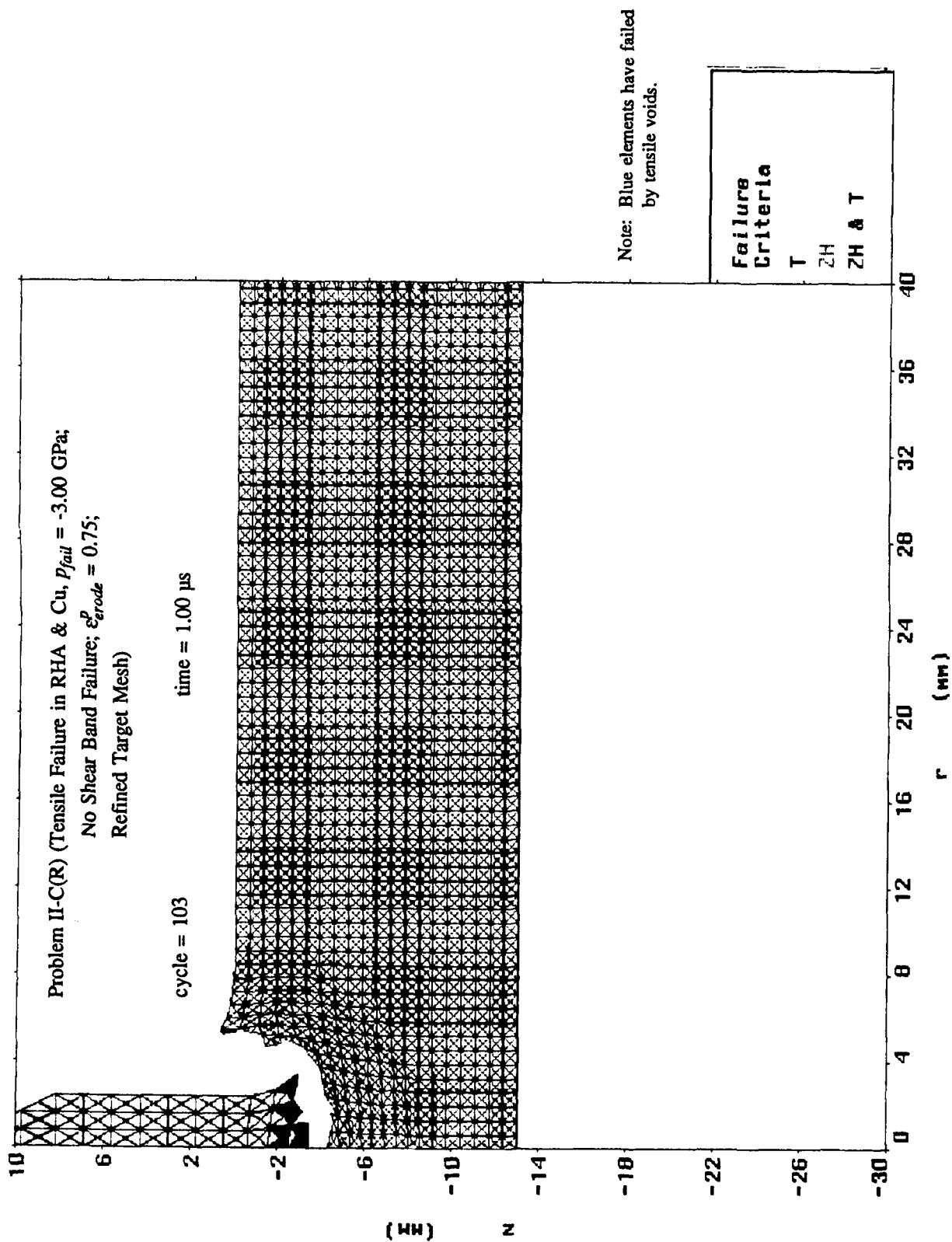


Figure 71. Mesh Plot at 1.00  $\mu$ s After Impact for Problem II-C(R).

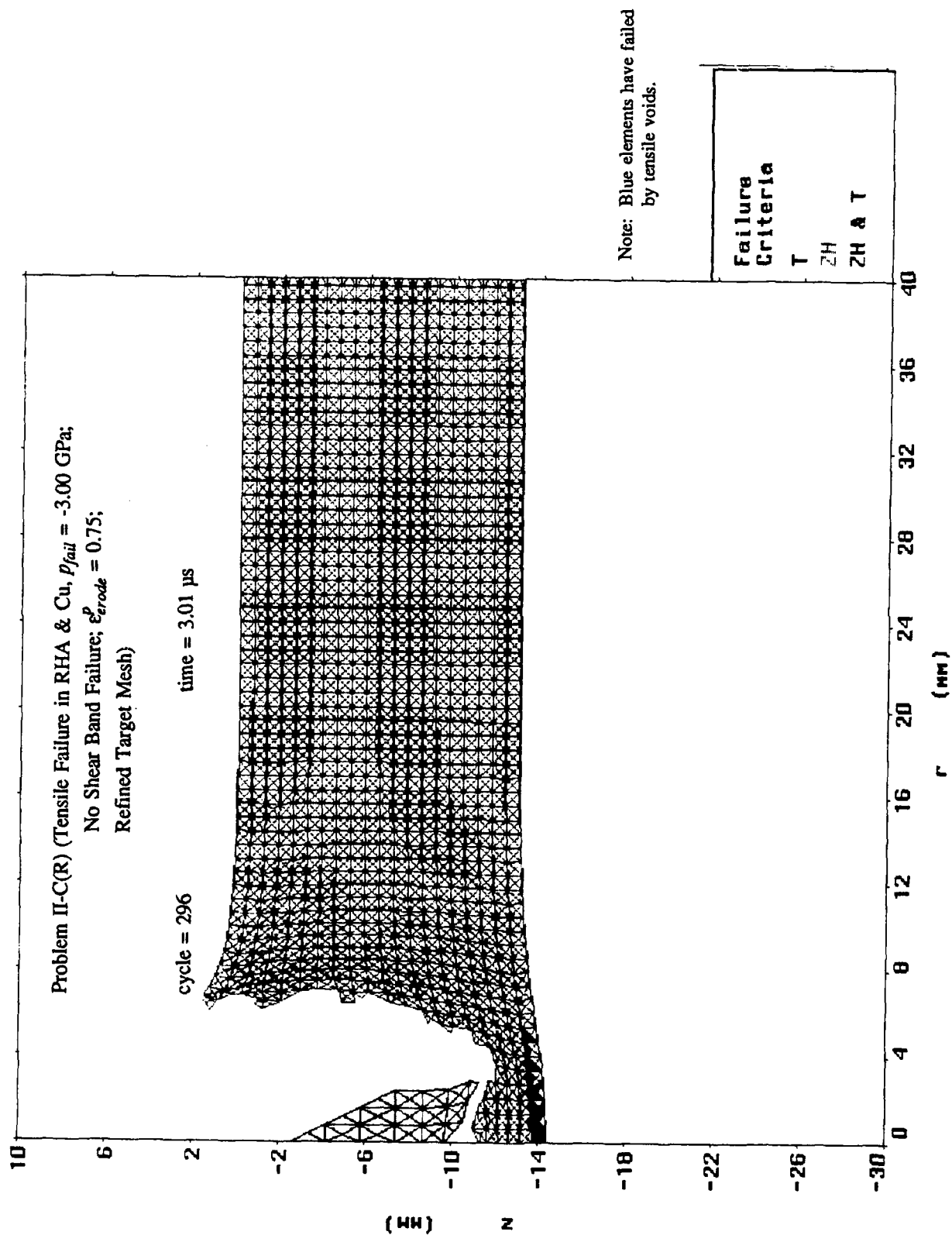


Figure 72. Mesh Plot at 3.01  $\mu$ s After Impact for Problem II-C(R).

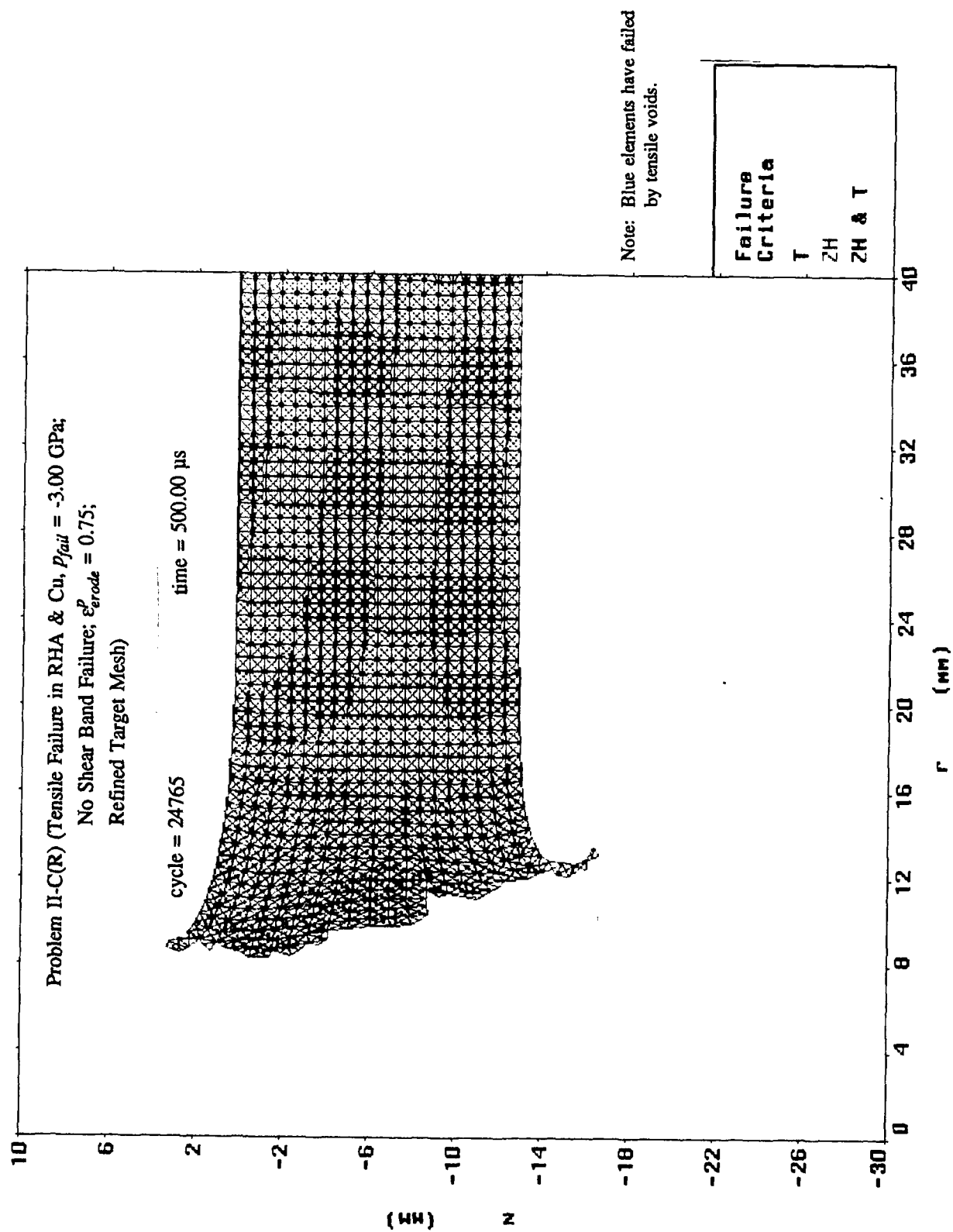


Figure 73. Mesh Plot at 500.00  $\mu$ s After Impact for Problem II-C(R).

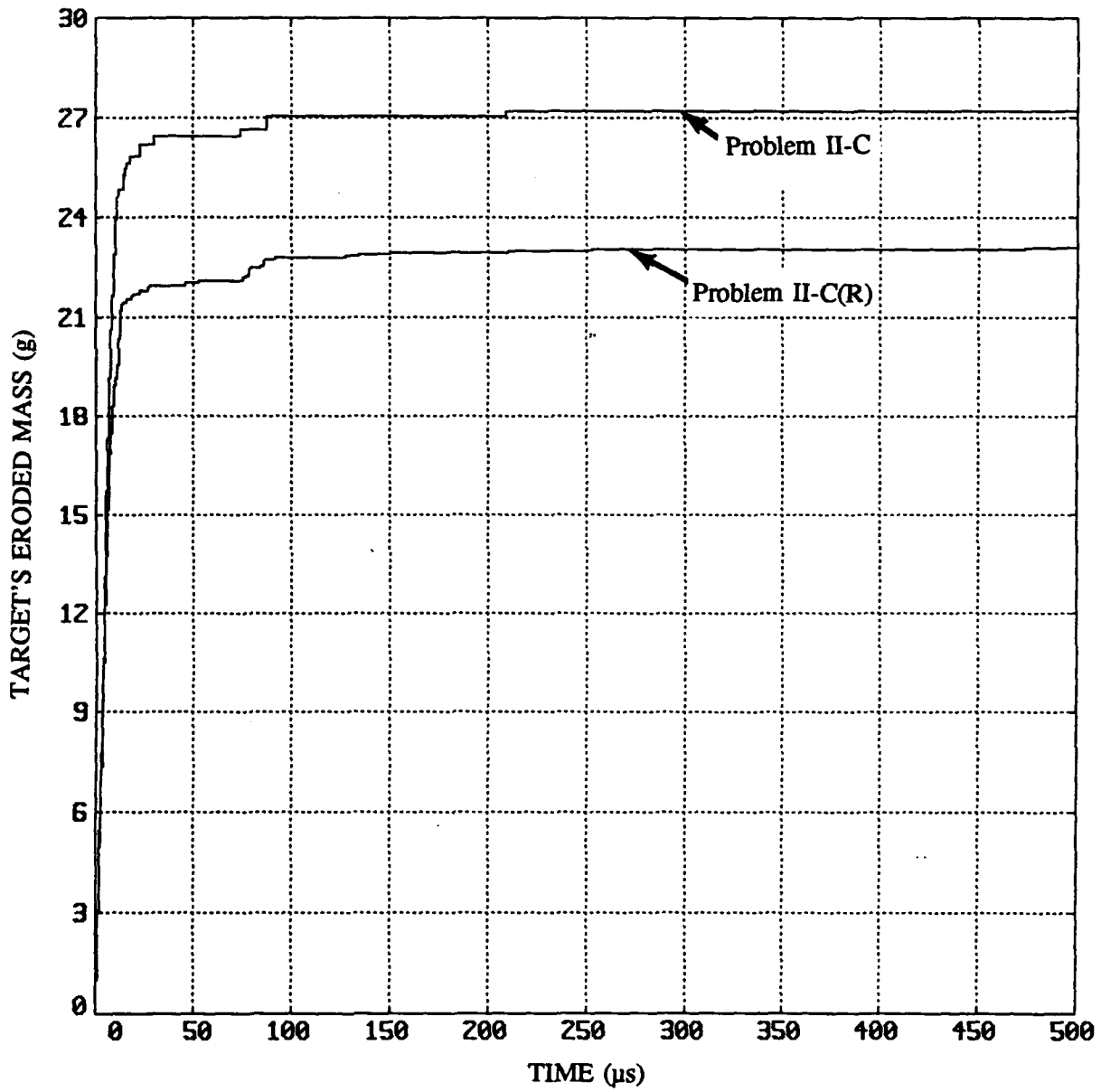


Figure 74. Mass Lost From Target Plate vs. Time for Problems II-C and II-C(R).

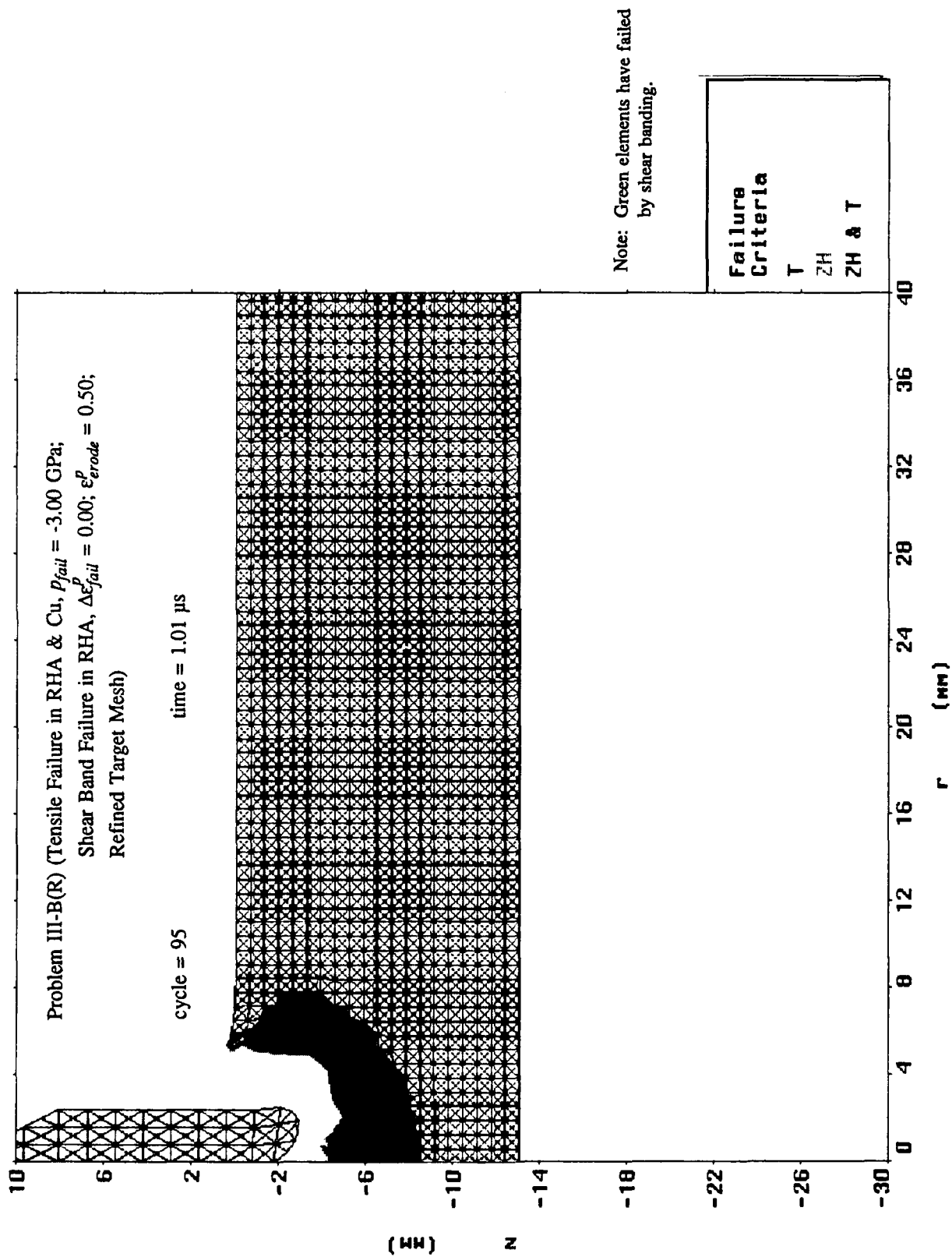


Figure 75. Mesh Plot at 1.01  $\mu$ s After Impact for Problem III-B(R).

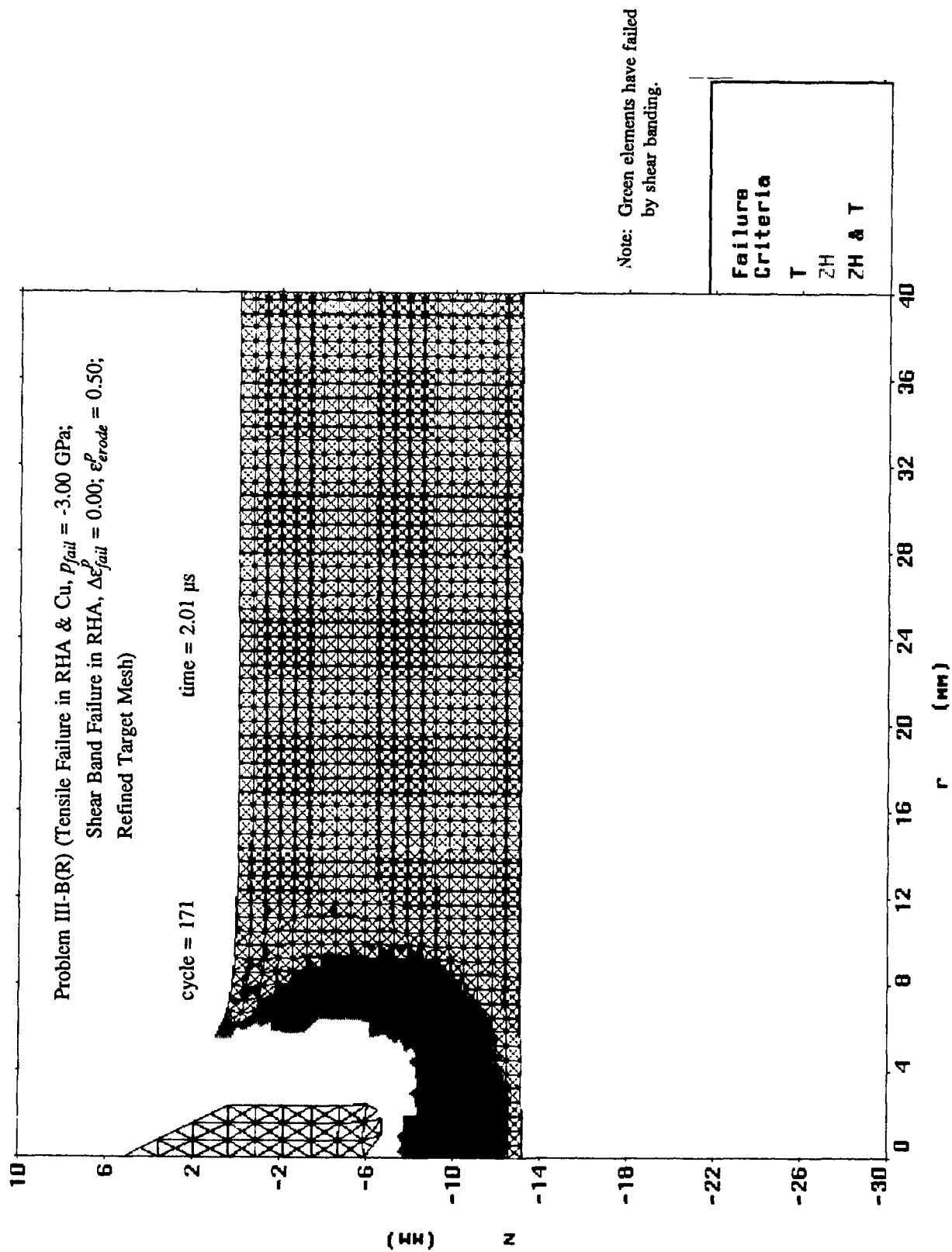


Figure 76. Mesh Plot at 2.01  $\mu$ s After Impact for Problem III-B(R).

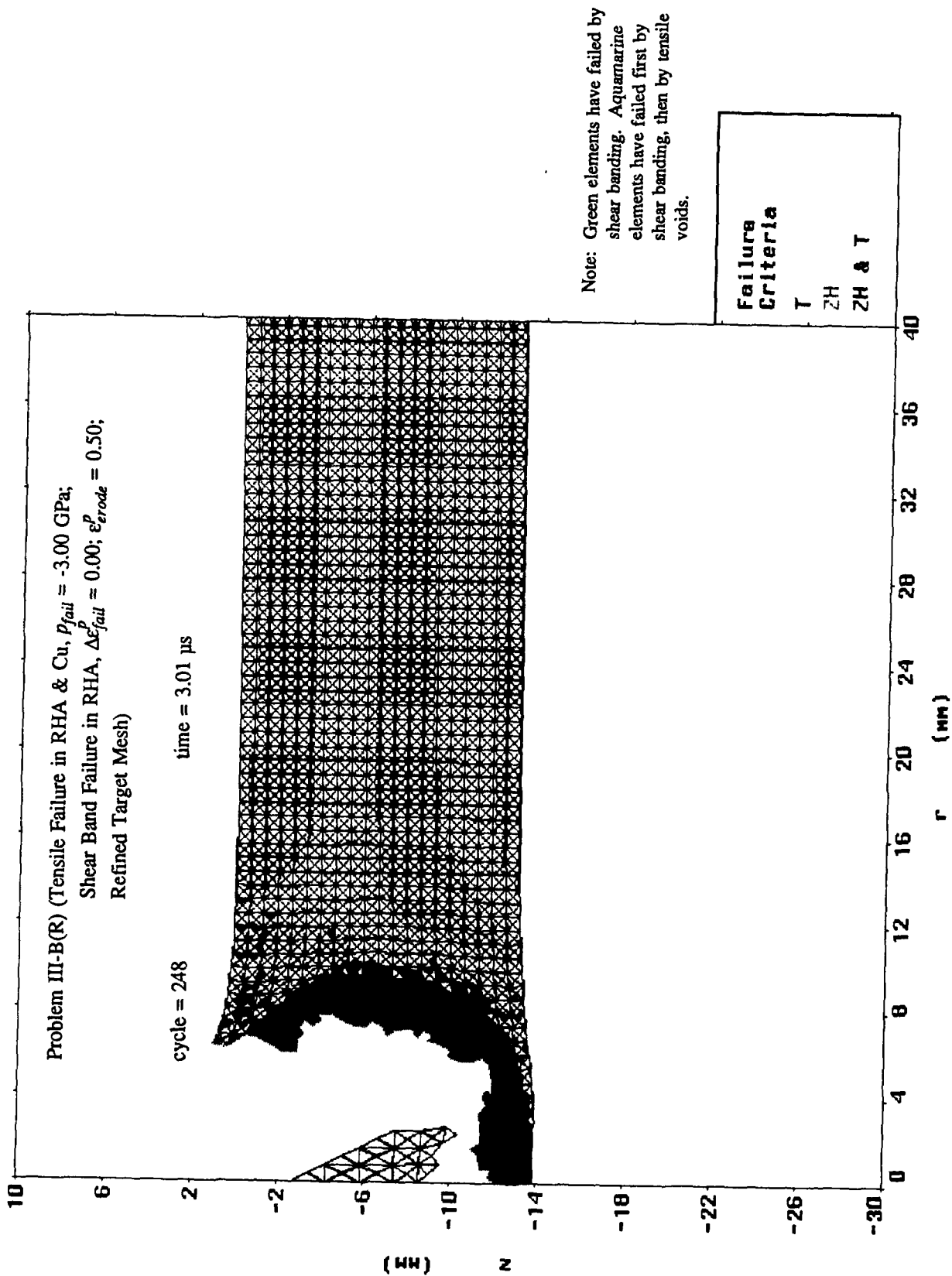


Figure 77. Mesh Plot at 3.01  $\mu$ s After Impact for Problem III-B(R).

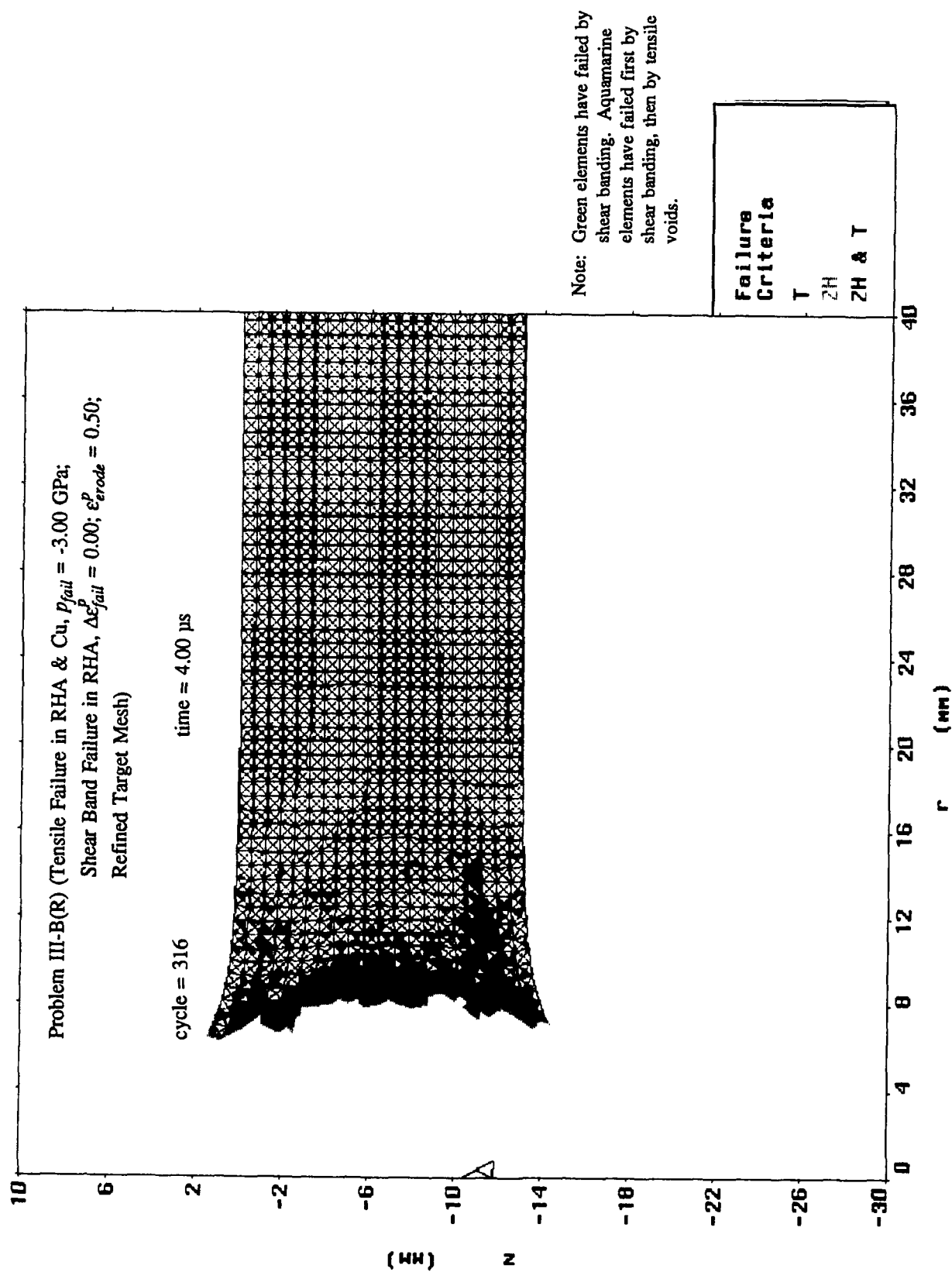


Figure 78. Mesh Plot at 4.00  $\mu s$  After Impact for Problem III-B(R).

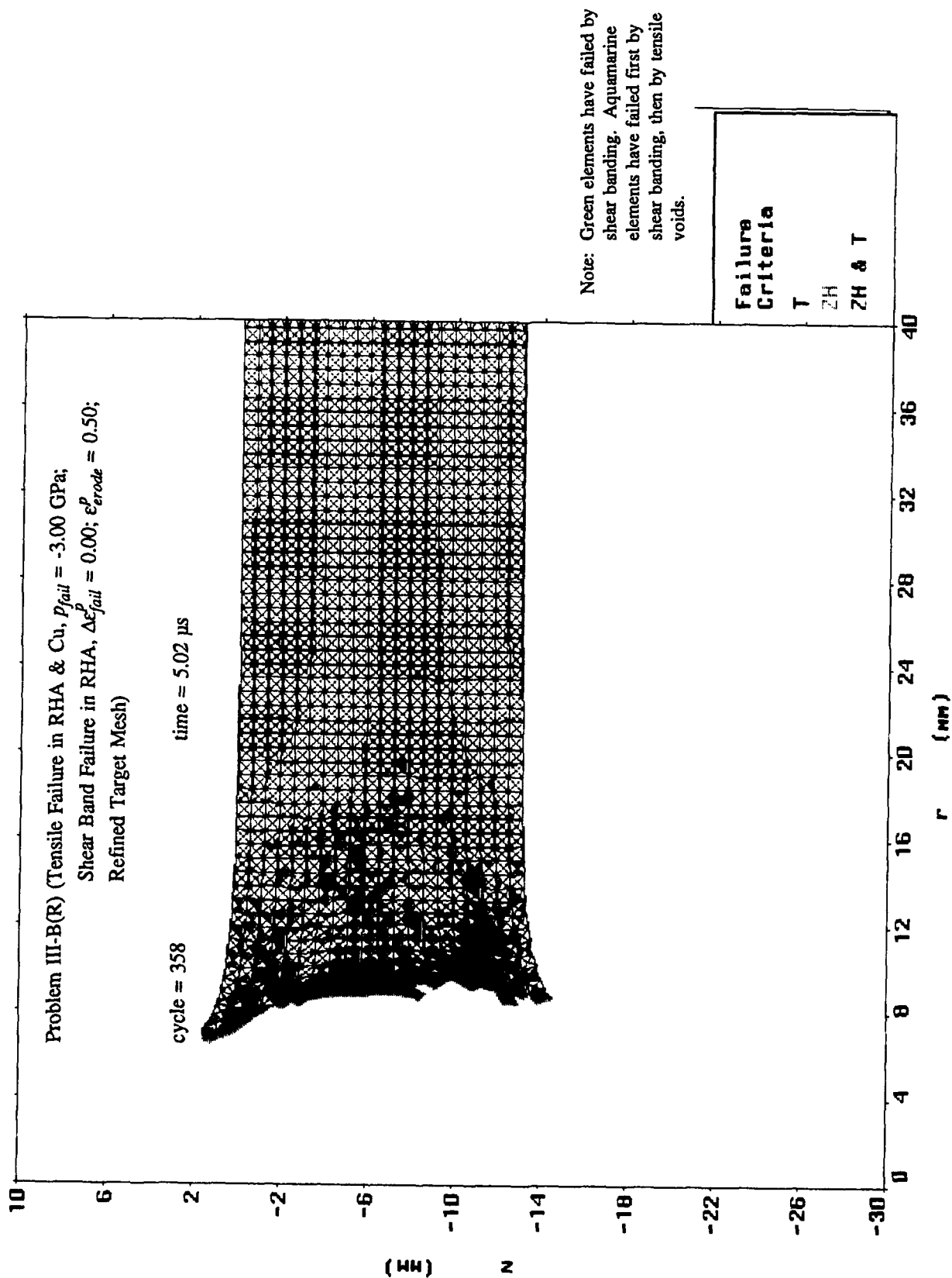


Figure 79. Mesh Plot at 5.02  $\mu$ s After Impact for Problem III-B(R).

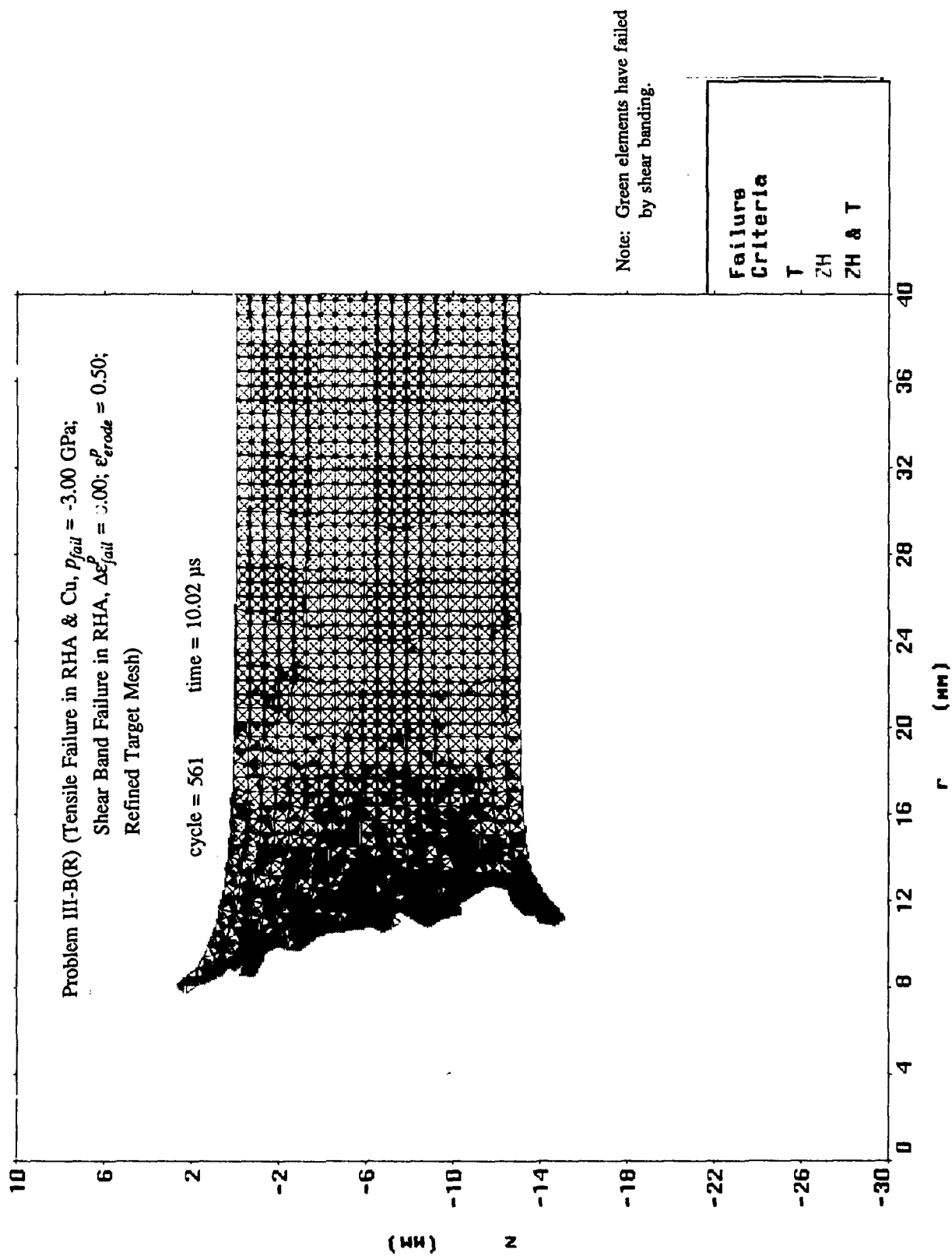


Figure 80. Mesh Plot at 10.02  $\mu$ s After Impact for Problem III-B(R).

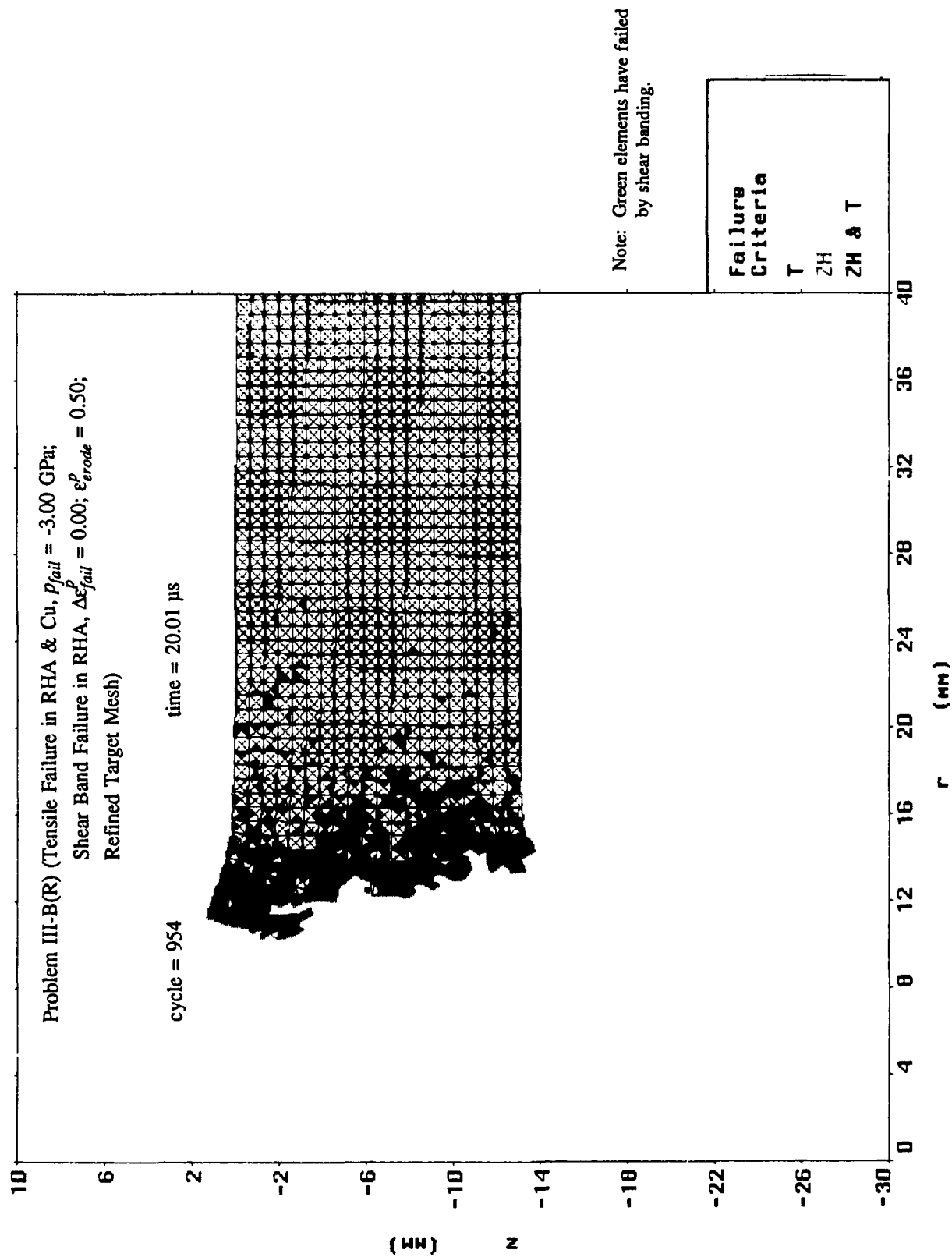


Figure 81. Mesh Plot at 20.02  $\mu$ s After Impact for Problem III-B(R).

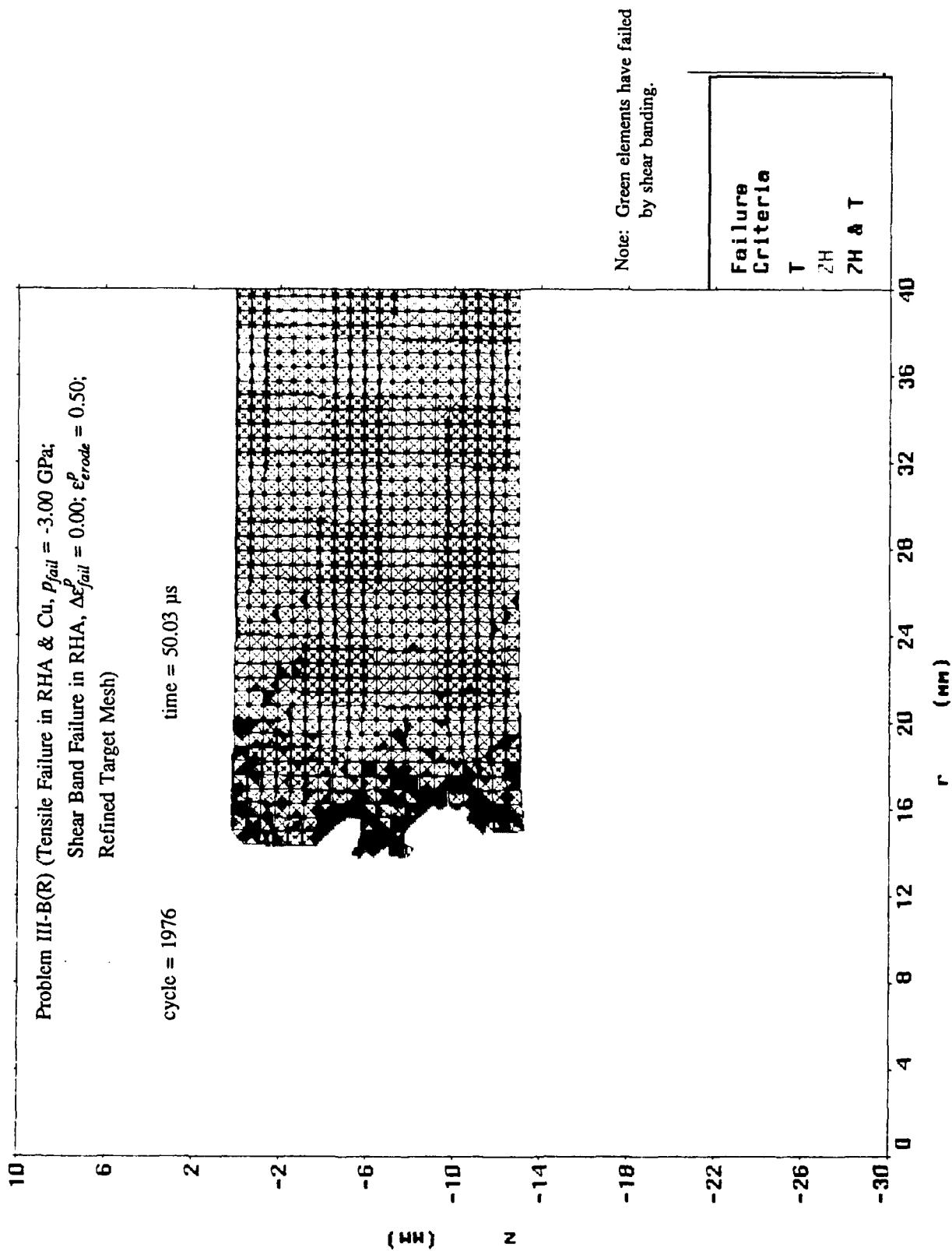


Figure 82. Mesh Plot at 50.03  $\mu$ s After Impact for Problem III-B(R).

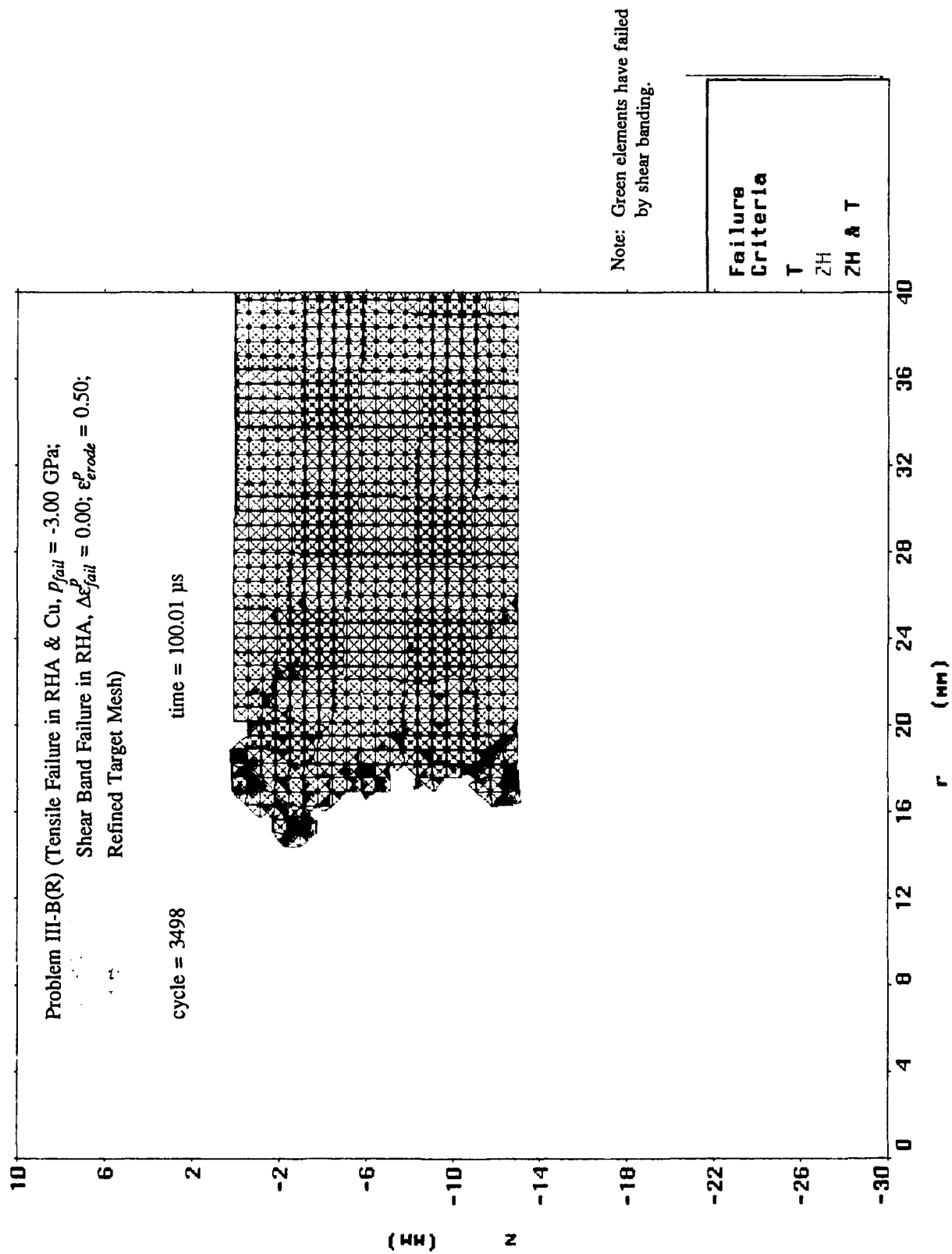


Figure 83. Mesh Plot at 100.01  $\mu$ s After Impact for Problem III-B(R).

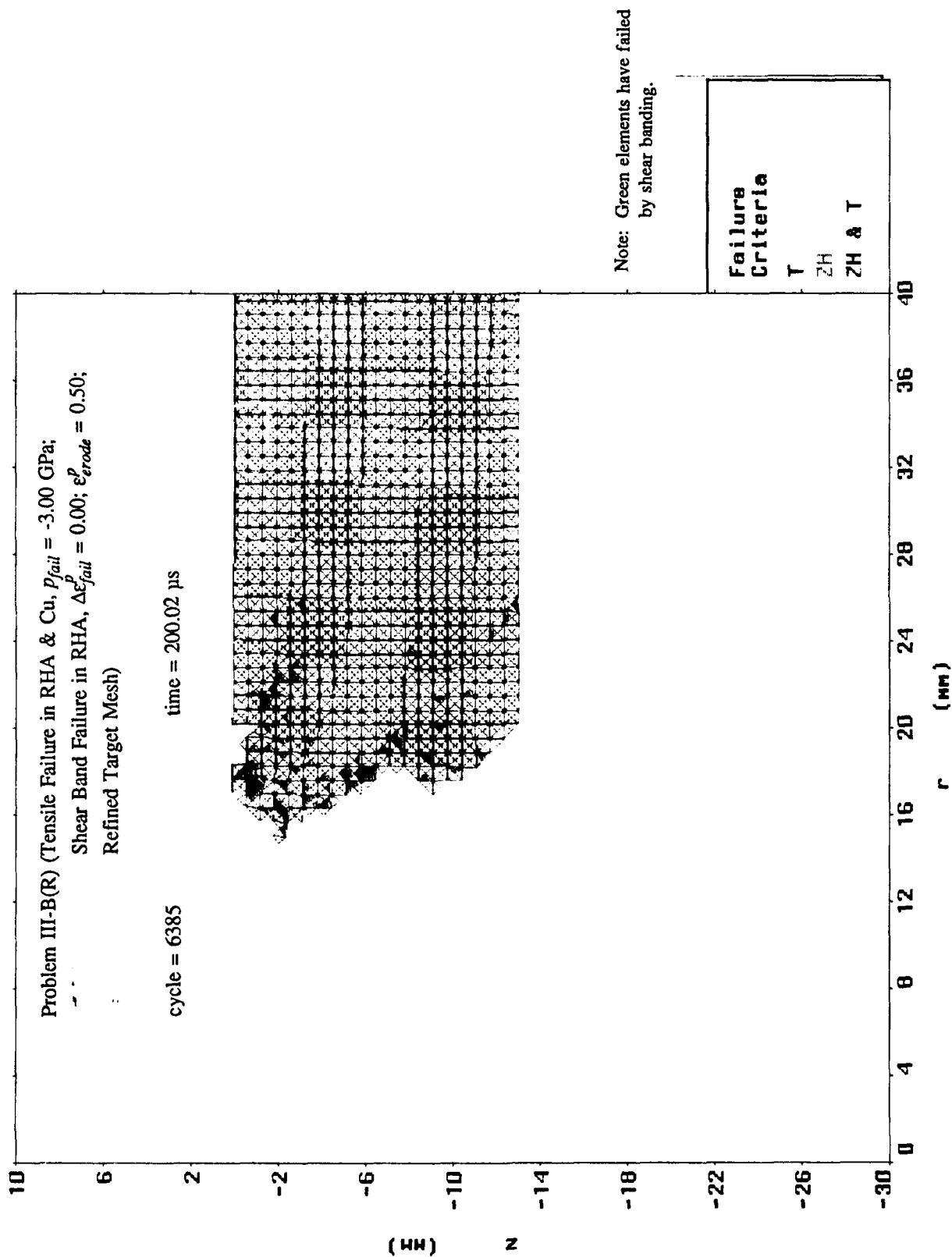


Figure 84. Mesh Plot at 200.02  $\mu$ s After Impact for Problem III-B(R).

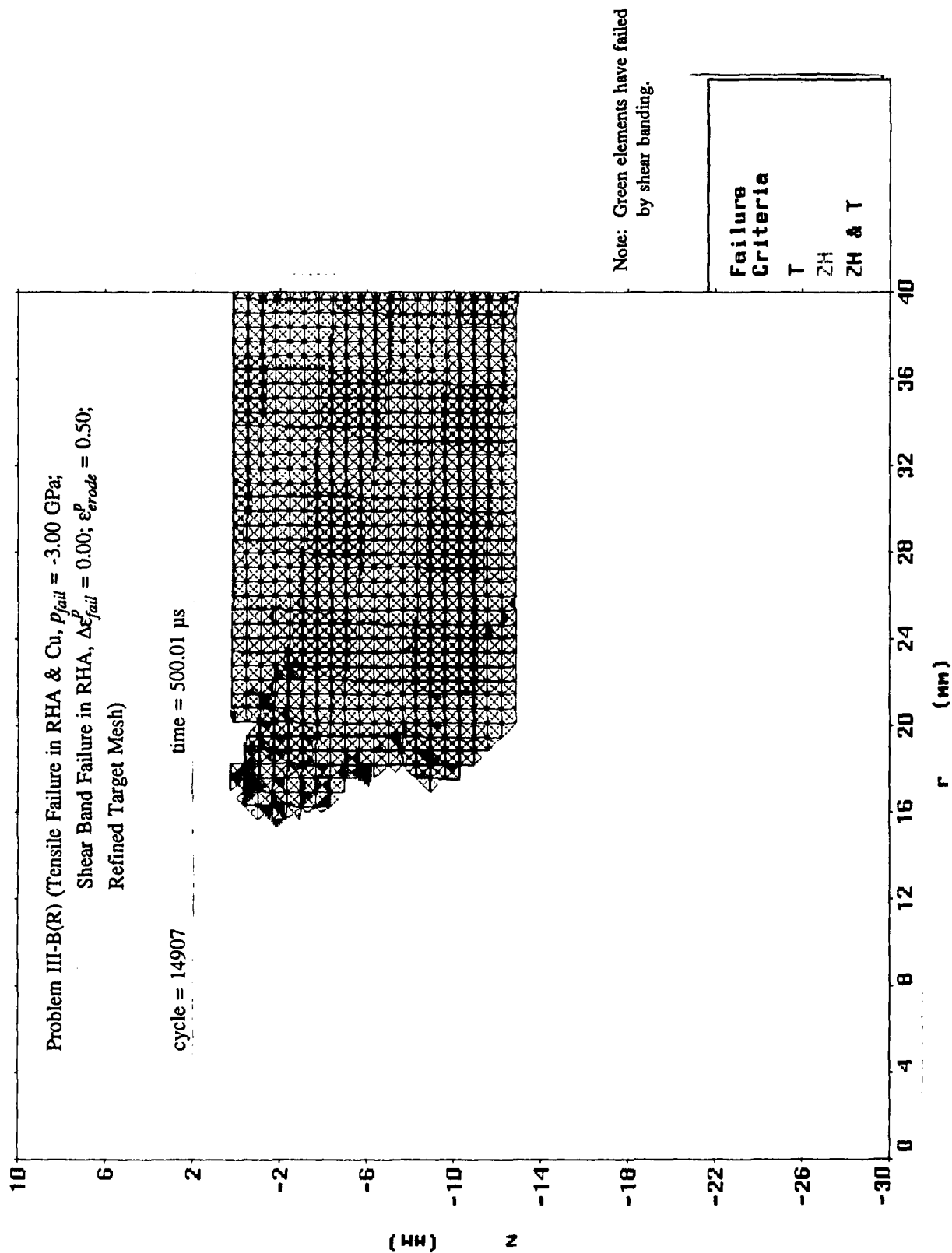
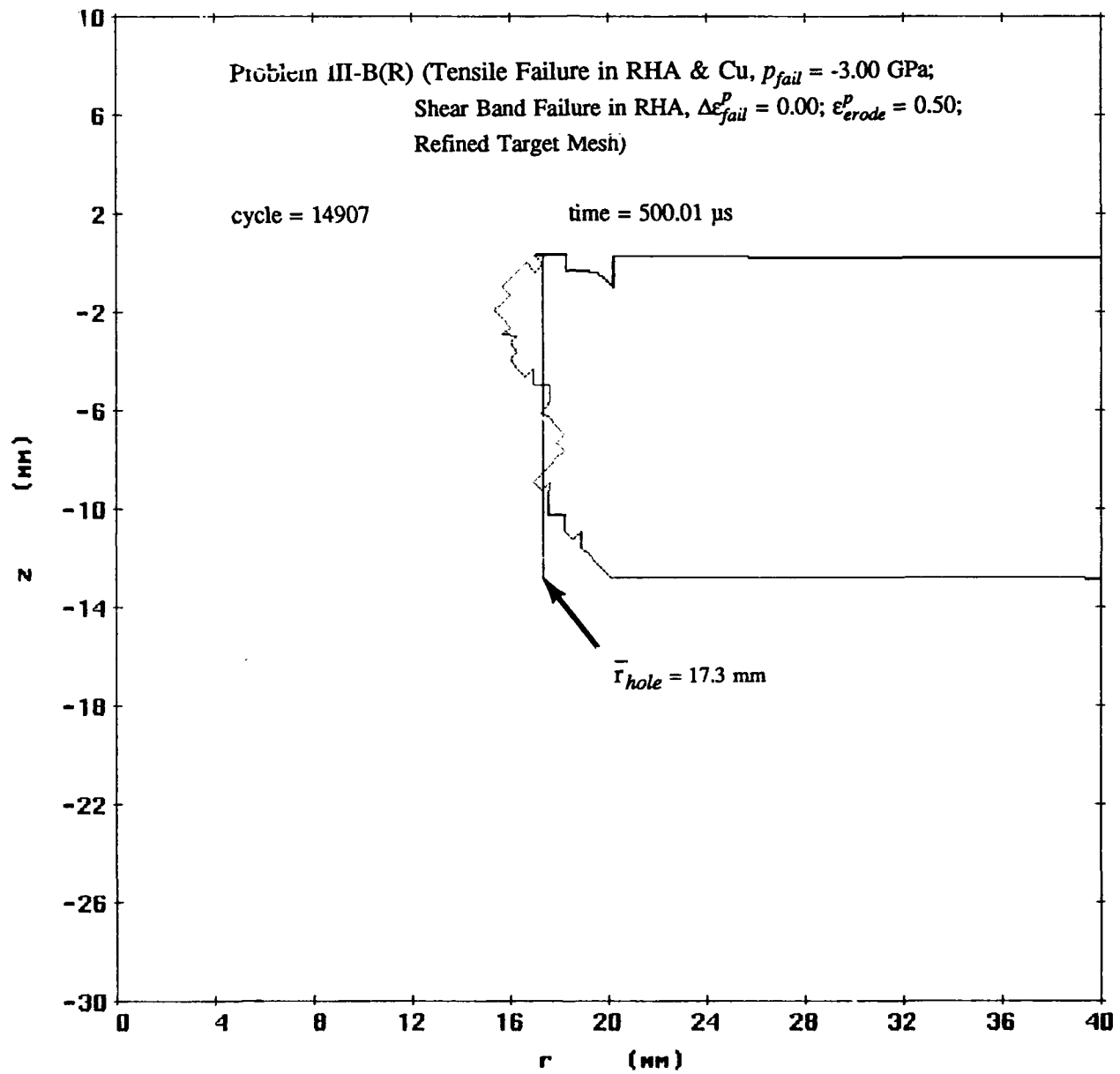


Figure 85. Mesh Plot at 500.01  $\mu$ s After Impact for Problem III-B(R).



NOTE:  $\bar{r}_{hole}$  calculation based on red portion of boundary.

Figure 86. Mesh Boundary at 500.01  $\mu$ s and Calculation of  $\bar{r}_{hole}$  for Problem III-B(R).

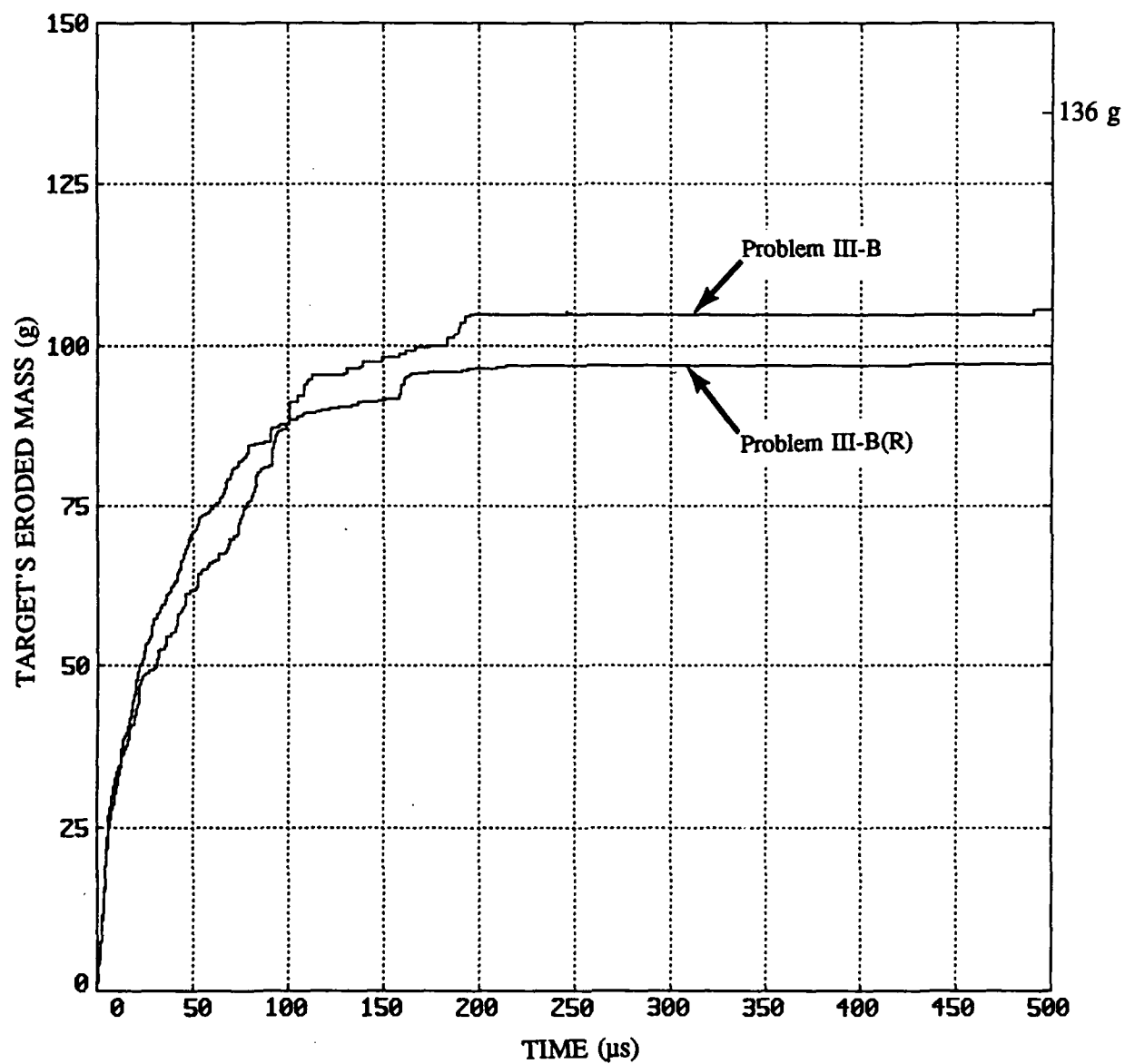


Figure 87. Mass Lost From Target Plate vs. Time for Problems III-B and III-B(R).

## 11. REFERENCES

- Barbee, Jr., T. W., L. Seaman, R. Crewdson and D. Curran. "Dynamic Fracture Criteria for Ductile and Brittle Metals." Journal of Materials, vol. 7, pp. 393-401, 1972.
- Johnson, G. R. "Analysis of Elastic-Plastic Impact Involving Severe Distortions." Journal of Applied Mechanics, vol. 98, pp. 439-444, 1976.
- Johnson, G. R. and W. H. Cook. "A Constitutive Model and Data for Metals Subjected to Large Strains, High Strain Rates and High Temperatures." Seventh International Ballistics Symposium Proceedings, The Hague, 1983, pp. 541-547.
- Johnson, G. R. and W. H. Cook. "Fracture Characteristics of Three Metals Subjected to Various Strains, High Strain Rates, Temperatures and Pressures." Engineering Fracture Mechanics, vol. 21, pp. 31-48, 1985.
- Johnson, G. R. and R. A. Stryk. "User Instructions for the EPIC-2 Code." AFATL-TR-86-51, Air Force Armament Laboratory, Eglin AFB, FL, 1986.
- Kohn, B. J. "Compilation of Hugoniot Equations of State." AFWL-TR-69-38, Air Force Weapons Laboratory, Kirtland AFB, NM, 1965.
- Raftenberg, M. N. "Experimental Study of RHA Plate Perforation by a Shaped-Charge Jet; Hole Size and Mass Loss." Developments in Mechanics, vol. 16, edited by R. C. Batra and B. F. Armaly, University of Missouri, Rolla, MO, p. 34, 1991.
- Raftenberg, M. N. "Experimental Investigation of RHA Plate Perforation by a Shaped-Charge Jet." Proceedings from the Army Symposium on Solid Mechanics, edited by S.-C. Chou, U. S. Army Materials Technology Laboratory, Watertown, MA, 1992, in press.
- Rinehart, J. S. "Some Quantitative Data Bearing on the Scabbing of Metals under Explosive Attack." Journal of Applied Physics, vol. 22, pp. 555-560, 1951.
- Seaman, L., D. R. Curran and D. A. Shockey. "Computational Models for Ductile and Brittle Fracture." Journal of Applied Physics, vol. 47, pp. 4814-4826, 1976.
- Stecher, F. P. and G. R. Johnson. "Lagrangian Computations for Projectile Penetration into Thick Plates." Computers in Engineering 1984, vol. 2, edited by W. A. Gruver, A.S.M.E., New York, NY, pp. 292-299, 1984.
- U. S. Department of Defense. "Military Specification: Armor Plate, Steel, Wrought, Homogeneous (for Use in Combat-Vehicles and for Ammunition Testing." MIL-A-12560G(MR), U. S. Army Materials Technology Laboratory, Watertown, MA, 1984.

Wright, T.W. and J. W. Walter. "On Stress Collapse in Adiabatic Shear Bands." Journal of the Mechanics and Physics of Solids, vol. 35, pp. 701-720, 1987.

Zener, C. and J. H. J. Hollomon. "Effect of Strain Rate Upon Plastic Flow of Steel." Journal of Applied Physics, vol. 15, pp. 22-32, 1944.

Zukas, J. A. "Stress Waves in Solids." in Impact Dynamics, edited by J. A. Zukas, T. Nicholas, H. F. Hallock, L. B. Greszczuk and D. R. Curran, Wiley, New York, NY, pp. 1-27, 1982.

## LIST OF SYMBOLS

$A, B, C, M, N$	parameters in the Johnson-Cook strength model
$D_{ij}^p$	$ij$ component of the plastic part of the rate of deformation tensor
$G$	elastic shear modulus
$K_1, K_2, K_3$	parameters in the Mie-Gruneison equation of state
$L_C, L_S, L_B, R_S, R_B$	parameters in the geometric model for the leading jet particle
$L_P$	length of the leading jet particle
$T$	temperature
$T_m$	melting temperature
$T_r$	room temperature
$T^*$	homologous temperature
$V_P$	volume of the leading jet particle
$e$	internal energy per undeformed volume
$f(\epsilon^P)$	stress reduction function used in the shear banding failure model
$p$	pressure
$p_{fail}$	pressure at which the onset of tensile failure occurs
$r$	radial coordinate
$\bar{r}_{hole}$	computational hole radius at 500 $\mu s$ after initial impact, averaged over the target plate's thickness
$\bar{r}_{hole}^{exp.}$	experimental final hole radius averaged over the target plate's thickness
$s_{ij}$	$ij$ component of the deviatoric Cauchy stress tensor following reduction
$s_{rr}, s_{zz}, s_{\theta\theta}$	radial, axial, circumferential normal components of the deviatoric Cauchy stress tensor following reduction

$s_{rz}$	shear component of the (deviatoric) Cauchy stress tensor following reduction
$s_{ij}^*$	$ij$ component of the deviatoric Cauchy stress tensor prior to reduction
$s_{rr}^*, s_{zz}^*, s_{\theta\theta}^*$	radial, axial, circumferential normal components of the deviatoric Cauchy stress tensor prior to reduction
$s_{rz}^*$	shear component of the (deviatoric) Cauchy stress tensor prior to reduction
$t$	time
$t_{.95}$	computational time, after initial impact, at which the target plate's cumulative mass loss equals $0.95\Delta M$
$t_{.95}^{exp.}$	experimental time, after initial impact, at which the target plate's cumulative mass loss equals $0.95\Delta M^{exp.}$
$z$	axial coordinate
$\bar{z}_p$	axial coordinate of the centroid of the leading jet particle
$\Delta M$	computational accumulated mass lost by the target plate at 500 $\mu s$ after initial impact
$\Delta M^{exp.}$	experimental total mass lost by the target plate
$\Delta \epsilon_{fail}^p$	the minimum increment above $\epsilon_{onset}^p$ of equivalent plastic strain corresponding to which all components of deviatoric Cauchy stress within an element are set to zero
$\Gamma$	Gruneison coefficient
$\chi$	expression involving parameters of the geometric model for the leading jet particle
$\epsilon^p$	equivalent plastic strain
$\epsilon_{erode}^p$	equivalent plastic strain at which a slideline's master surface element is eroded
$\epsilon_{onset}^p$	equivalent plastic strain within an element at the time of the onset of its failure by shear banding

$\dot{\epsilon}^p$	time rate of change of equivalent plastic strain
$\mu$	fractional change in density from the undeformed state
$\rho$	density
$\rho_0$	undeformed density
$\sigma$	equivalent Cauchy stress
$\sigma_y$	flow stress
$\sigma_{rr}, \sigma_{zz}, \sigma_{\theta\theta}$	radial, axial, circumferential normal components of the Cauchy stress tensor

INTENTIONALLY LEFT BLANK.

<u>No. of Copies</u>	<u>Organization</u>	<u>No. of Copies</u>	<u>Organization</u>
2	Administrator Defense Technical Info Center ATTN: DTIC-DDA Cameron Station Alexandria, VA 22304-6145	1	Commander U.S. Army Tank-Automotive Command ATTN: ASQNC-TAC-DIT (Technical Information Center) Warren, MI 48397-5000
1	Commander U.S. Army Materiel Command ATTN: AMCAM 5001 Eisenhower Ave. Alexandria, VA 22333-0001	1	Director U.S. Army TRADOC Analysis Command ATTN: ATRC-WSR White Sands Missile Range, NM 88002-5502
1	Commander U.S. Army Laboratory Command ATTN: AMSLC-DL 2800 Powder Mill Rd. Adelphi, MD 20783-1145	1	Commandant U.S. Army Field Artillery School ATTN: ATSF-CSI Ft. Sill, OK 73503-5000
2	Commander U.S. Army Armament Research, Development, and Engineering Center ATTN: SMCAR-IMI-I Picatinny Arsenal, NJ 07806-5000	(Class. only) 1	Commandant U.S. Army Infantry School ATTN: ATSH-CD (Security Mgr.) Fort Benning, GA 31905-5660
2	Commander U.S. Army Armament Research, Development, and Engineering Center ATTN: SMCAR-TDC Picatinny Arsenal, NJ 07806-5000	(Unclass. only) 1	Commandant U.S. Army Infantry School ATTN: ATSH-CD-CSO-OR Fort Benning, GA 31905-5660
1	Director Benet Weapons Laboratory U.S. Army Armament Research, Development, and Engineering Center ATTN: SMCAR-CCB-TL Watervliet, NY 12189-4050	1	WL/MNOI Eglin AFB, FL 32542-5000
(Unclass. only) 1	Commander U.S. Army Rock Island Arsenal ATTN: SMCRI-TL/Technical Library Rock Island, IL 61299-5000		<u>Aberdeen Proving Ground</u>
1	Director U.S. Army Aviation Research and Technology Activity ATTN: SAVRT-R (Library) M/S 219-3 Ames Research Center Moffett Field, CA 94035-1000	2	Dir, USAMSAA ATTN: AMXSY-D AMXSY-MP, H. Cohen
1	Commander U.S. Army Missile Command ATTN: AMSMI-RD-CS-R (DOC) Redstone Arsenal, AL 35898-5010	1	Cdr, USATECOM ATTN: AMSTE-TC
		3	Cdr, CRDEC, AMCCOM ATTN: SMCCR-RSP-A SMCCR-MU SMCCR-MSI
		1	Dir, VLAMO ATTN: AMSLC-VL-D
		10	Dir, USABRL ATTN: SLCBR-DD-T

<u>No. of Copies</u>	<u>Organization</u>	<u>No. of Copies</u>	<u>Organization</u>
2	Director Defense Advanced Research Projects Agency ATTN: J. Richardson Technical Information 1400 Wilson Blvd. Arlington, VA 22209-2308	1	U.S. Naval Academy Dept. of Mathematics ATTN: R. Malek-Madani Annapolis, MD 21402
3	U.S. Army Research Office ATTN: J. Chandra K. Iyer Technical Library P.O. Box 12211 4300 Miami Blvd. Research Triangle Park, NC 27709	2	Naval Weapons Center ATTN: S. A. Finnegan Technical Library China Lake, CA 93555
1	U.S. Army MICOM ATTN: AMSMI-RD-ST-WF, Michael Schexnayder Redstone Arsenal, AL 35898-5250	3	Air Force Armament Laboratory ATTN: J. Foster W. Cook Technical Library Eglin AFB, FL 32542-5438
5	U.S. Army Materials Technology Laboratory ATTN: SLCMT-MRT, Tony Chou Charles S. White A.M. Rajendran J. Beatty Technical Library Watertown, MA 02172-0001	1	Air Force Wright Aeronautical Laboratories Air Force Systems Command Materials Laboratory ATTN: T. Nicholas Wright-Patterson AFB, OH 45433
1	Commander U.S. Army Armament Research, Development, and Engineering Center ATTN: SMCAR-AA, J. Pearson Picatinny Arsenal, NJ 07806-5000	9	Director Los Alamos National Laboratory ATTN: G. E. Cort, F663 Thomas F. Adams, F663 Robert Karpp, MS J960 John Bolstad, MS G787 K. S. Holian, MS B295 J. Chapyak P. Follansbee G. T. Gray Technical Library P.O. Box 1663 Los Alamos, NM 87545
2	Commander Naval Surface Warfare Center ATTN: W. Holt Technical Library Dahlgren, VA 22448-5000	1	Sandia National Laboratories ATTN: D. Bammann Livermore, CA 94550
4	Commander Naval Surface Warfare Center ATTN: F. J. Zerilli Code U12, H. Chen Code R14, H. Mair Code X211, Library Silver Spring, MD 20902-5000	1	University of Missouri-Rolla Dept. of Mechanical and Aerospace Engineering ATTN: R. Batra Rolla, MO 65401-0249

<u>No. of Copies</u>	<u>Organization</u>
9	<p>Director Lawrence Livermore National Laboratory ATTN: Barry R. Bowman, L-122 John E. Reaugh, L-290 Michael J. Murphy W. H. Gourdin R. Whirley G. Goudreau D. J. Steinberg, L-35 Robert Tipton, L-35 Technical Library P.O. Box 808 Livermore, CA 94550</p>
7	<p>Sandia National Laboratories ATTN: L. Davison W. Herrman M. Forrestal J. M. McGlaun P. Yarrington V. Luk D. Grady P.O. Box 5800 Albuquerque, NM 87185-5800</p>
1	<p>Denver Research Institute University of Denver ATTN: R. Recht P.O. Box 10127 Denver, CO 80210</p>
1	<p>Massachusetts Institute of Technology Dept. of Mechanical Engineering ATTN: L. Anand Cambridge, MA 02139</p>
1	<p>California Research and Technology, Inc. ATTN: Mark Majerus P.O. Box 2229 Princeton, NJ 08543-2229</p>
1	<p>Rensselaer Polytechnic Institute Dept. of Computer Science ATTN: J. Flaherty Troy, NY 12181</p>

<u>No. of Copies</u>	<u>Organization</u>
3	<p>Brown University Division of Engineering ATTN: R. Clifton J. Duffy A. Needleman Providence, RI 02912</p>
1	<p>Cornell University Dept. of Theoretical and Applied Mechanics ATTN: J. Jenkins Ithaca, NY 14850</p>
1	<p>North Carolina State University Dept. of Civil Engineering ATTN: Y. Horie Raleigh, NC 27607</p>
1	<p>North Carolina State University Dept. of Mechanical Engineering ATTN: M. Zikry Raleigh, NC 27607</p>
2	<p>The Johns Hopkins University Dept. of Mechanical Engineering Latrobe Hall ATTN: A. Douglas K. T. Ramesh 34th and Charles Streets Baltimore, MD 21218</p>
3	<p>University of California at San Diego Dept. of Applied Mechanics and Engineering Sciences ATTN: S. Nemat-Nasser M. Meyers D. J. Benson La Jolla, CA 92093</p>
1	<p>Northwestern University Dept. of Applied Mathematics ATTN: T. Belytschko Evanston, IL 60201</p>
1	<p>University of Illinois Dept. of Theoretical and Applied Mechanics ATTN: T. Shawki Urbana, IL 61801</p>

<u>No. of</u> <u>Copies</u>	<u>Organization</u>
1	University of Texas Dept. of Engineering Mechanics ATTN: J. Oden Austin, TX 78712
1	University of Maryland Dept. of Mechanical Engineering ATTN: R. Armstrong College Park, MD 20742
1	Washington State University Dept. of Physics ATTN: Y. Gupta Pullman, WA 99163
1	Washington State University Dept. of Mechanical and Materials Engineering ATTN: H. Zbib Pullman, WA 99164-2920
1	Arizona State University Mechanical and Aerospace Engineering M/S 6106 ATTN: D. Krajcinovic Tempe, AZ 85287-6106
1	Michigan Technological University Dept. of Mechanical Engineering ATTN: William W. Predebon 1400 Townsend Dr. Houghton, MI 49931-1295
1	University of Alabama ATTN: S. Jones 210 Hardaway Hall Box 870278 Tuscaloosa, AL 35487-0278
1	University of Texas at El Paso Dept. of Metallurgical and Materials Engineering ATTN: L. E. Murr El Paso, TX 79968

<u>No. of</u> <u>Copies</u>	<u>Organization</u>
1	State University of New York at Stony Brook Applied Mathematics and Statistics Department ATTN: James Glimm Stony Brook, NY 11794
1	Aerojet Precision Weapons Dept. 5131/T-W ATTN: Joseph Carleone 1100 Hollyvale Azusa, CA 91702
2	Dyna East Corporation ATTN: P. C. Chou W. Flis 3201 Arch St. Philadelphia, PA 19104
2	Southwest Research Institute ATTN: C. Anderson S. Bodner P.O. Drawer 28255 San Antonio, TX 78228-0255
1	Battelle Edgewood Operations ATTN: R. Jameson 2113 Emmorton Park Rd. Edgewood, MD 21040
2	Alliant Techsystems, Inc. ATTN: Gordon R. Johnson Tim Holmquist MN 48-2700 7225 Northland Dr. Brooklyn Park, MN 55428
1	S-Cubed ATTN: R. Sedgwick P.O. Box 1620 La Jolla, CA 92038-1620
1	Orlando Technology, Inc. ATTN: Dan Matuska P.O. Box 855 Shalimar, FL 32579

No. of

Copies   Organization

- 1   Livermore Software Technology Corp.  
ATTN: John O. Hallquist  
2876 Waverly Way  
Livermore, CA 94550
  
- 2   SRI International  
ATTN: D. Curran  
H. Giovanola  
333 Ravenswood Ave.  
Menlo Park, CA 94025

No. of

Copies Organization

- 1 Defense Research Suffield  
ATTN: Chris Weickert  
Ralston, Alberta, JOJ 2NO Ralston  
Canada
- 1 Ernst Mach Institute  
ATTN: A. J. Stilp  
Eckerstrasse 4  
D-7800 Frieburg i. Br.  
Germany
- 1 Royal Armament R&D Establishment  
ATTN: Ian Cullis  
Fort Halstead  
Sevenoaks, Kent TN14 7BJ  
England
- 1 Centre d'Etudes de Gramat  
ATTN: SOLVE Gerard  
46500 Gramat  
France
- 1 Materials Research Laboratories  
ATTN: R. L. Woodward  
P.O. Box 50  
Ascot Vale  
Victoria 3032  
Australia
- 1 Israel Military Industries  
ATTN: E. Hirsch  
Ramat Hasharon 47100  
Israel